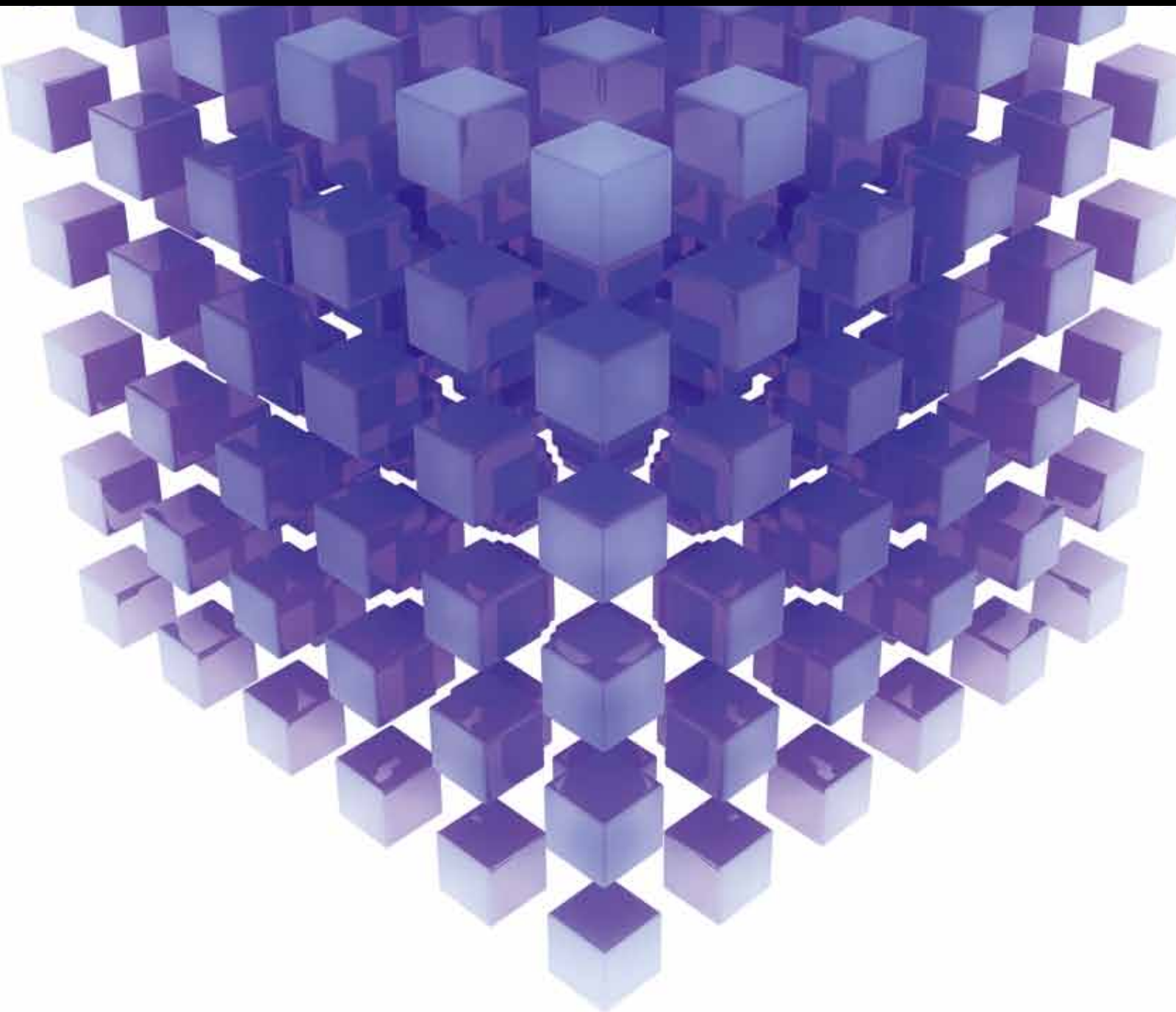


MATHEMATICAL PROBLEMS IN ENGINEERING

SMART CONTROL ALGORITHMS AND TECHNOLOGY IN CIVIL INFRASTRUCTURES

GUEST EDITORS: HONGNAN LI, GANGBING SONG, JEONG-TAE KIM, AND GANG LI





Smart Control Algorithms and Technology in Civil Infrastructures

Mathematical Problems in Engineering

Smart Control Algorithms and Technology in Civil Infrastructures

Guest Editors: Hongnan Li, Gangbing Song, Jeong-Tae Kim,
and Gang Li



Copyright © 2014 Hindawi Publishing Corporation. All rights reserved.

This is a special issue published in “Mathematical Problems in Engineering.” All articles are open access articles distributed under the Creative Commons Attribution License, which permits unrestricted use, distribution, and reproduction in any medium, provided the original work is properly cited.

Editorial Board

- M. Abd El Aziz, Egypt
E. M. Abdel-Rahman, Canada
R. K. Abu Al-Rub, USA
Sarp Adali, South Africa
Salvatore Alfonzetti, Italy
Igor Andrianov, Germany
Sebastian Anita, Romania
W. Assawinchaichote, Thailand
Erwei Bai, USA
Ezzat G. Bakhoum, USA
José M. Balthazar, Brazil
R. K. Bera, India
C. Bérenguer, France
Jonathan N. Blakely, USA
Stefano Boccaletti, Spain
Stephane P.A. Bordas, USA
Daniela Boso, Italy
M. Boutayeb, France
Michael J. Brennan, UK
Salvatore Caddemi, Italy
Piermarco Cannarsa, Italy
Jose E. Capilla, Spain
Carlo Cattani, Italy
Marcelo M. Cavalcanti, Brazil
Diego J. Celentano, Chile
Mohammed Chadli, France
Arindam Chakraborty, USA
Yong-Kui Chang, China
Michael J. Chappell, UK
Kui Fu Chen, China
Xinkai Chen, Japan
Kue-Hong Chen, Taiwan
Jyh-Horng Chou, Taiwan
Slim Choura, Tunisia
Cesar Cruz-Hernandez, Mexico
Swagatam Das, India
Filippo de Monte, Italy
Antonio Desimone, Italy
Yannis Dimakopoulos, Greece
Baocang Ding, China
Joao B. R. Do Val, Brazil
Daoyi Dong, Australia
B. Dubey, India
Horst Ecker, Austria
M. Onder Efe, Turkey
Elmetwally Elabbasy, Egypt
A. Elías-Zúñiga, Mexico
Anders Eriksson, Sweden
Vedat S. Erturk, Turkey
Moez Feki, Tunisia
Ricardo Femat, Mexico
Robertt A. Valente, Portugal
C. Fuerte-Esquivel, Mexico
Zoran Gajic, USA
Ugo Galvanetto, Italy
Furong Gao, Hong Kong
Xin-Lin Gao, USA
Behrouz Gatmiri, Iran
Oleg V. Gendelman, Israel
Didier Georges, France
Paulo B. Gonçalves, Brazil
Oded Gottlieb, Israel
Fabrizio Greco, Italy
Quang Phuc Ha, Australia
M. R. Hajj, USA
Tony S. W. Hann, Taiwan
Thomas Hanne, Switzerland
K. R. (Stevanovic) Hedrih, Serbia
M.I. Herreros, Spain
Wei-Chiang Hong, Taiwan
Jaromir Horacek, Czech Republic
Huabing Huang, China
Chuangxia Huang, China
Gordon Huang, Canada
Yi Feng Hung, Taiwan
Hai-Feng Huo, China
Asier Ibeas, Spain
Anuar Ishak, Malaysia
Reza Jazar, Australia
Zhijian Ji, China
Jun Jiang, China
J. J. Judice, Portugal
Tadeusz Kaczorek, Poland
Tamas Kalmar-Nagy, USA
Tomasz Kapitaniak, Poland
Hamid Reza Karimi, Norway
Metin O. Kaya, Turkey
Nikolaos Kazantzis, USA
Farzad Khani, Iran
K. Krabbenhoft, Australia
Ren-Jieh Kuo, Taiwan
Jurgen Kurths, Germany
Claude Lamarque, France
Usik Lee, Korea
Marek Lefik, Poland
Stefano Lenci, Italy
Roman Lewandowski, Poland
Shanling Li, Canada
Ming Li, China
Jian Li, China
Shihua Li, China
Teh-Lu Liao, Taiwan
Panos Liatsis, UK
Shueei M. Lin, Taiwan
Yi-Kuei Lin, Taiwan
Jui-Sheng Lin, Taiwan
Yuji Liu, China
Wanquan Liu, Australia
Bin Liu, Australia
Paolo Lonetti, Italy
V. C. Loukopoulos, Greece
Junguo Lu, China
Chien-Yu Lu, Taiwan
Alexei Mailybaev, Brazil
Manoranjan K. Maiti, India
O. D. Makinde, South Africa
R. Martinez-Guerra, Mexico
Driss Mehdi, France
Roderick Melnik, Canada
Xinzhu Meng, China
Yuri V. Mikhlin, Ukraine
G. Milovanovic, Serbia
Ebrahim Momoniat, South Africa
Trung Nguyen Thoi, Vietnam
Hung Nguyen-Xuan, Vietnam
Ben T. Nohara, Japan
Sotiris K. Ntouyas, Greece
Gerard Olivar, Colombia
Claudio Padra, Argentina
Bijaya Ketan Panigrahi, India
Francesco Pellicano, Italy
Matjaz Perc, Slovenia
Vu Ngoc Phat, Vietnam
M. do Rosário Pinho, Portugal
A. Pogromsky, The Netherlands

Seppo Pohjolainen, Finland
Stanislav Potapenko, Canada
Sergio Preidikman, USA
Carsten Proppe, Germany
Hector Puebla, Mexico
Justo Puerto, Spain
Dane Quinn, USA
K. R. Rajagopal, USA
Gianluca Ranzi, Australia
Sivaguru Ravindran, USA
G. Rega, Italy
Pedro Ribeiro, Portugal
J. Rodellar, Spain
R. Rodriguez-Lopez, Spain
A. J. Rodriguez-Luis, Spain
Ignacio Romero, Spain
Hamid Ronagh, Australia
Carla Roque, Portugal
Rubén R. García, Spain
Manouchehr Salehi, Iran
Miguel A. Sanjuán, Spain
Ilmar F. Santos, Denmark
Nickolas S. Sapidis, Greece
E. J. Sapountzakis, Greece
Bozidar Sarler, Slovenia
Andrey V. Savkin, Australia
Massimo Scalia, Italy
Mohamed A. Seddeek, Egypt
A. P. Seyranian, Russia
Leonid Shaikhet, Ukraine

Cheng Shao, China
Bo Shen, Germany
Jian-Jun Shu, Singapore
Zhan Shu, UK
Dan Simon, USA
Luciano Simoni, Italy
Grigori M. Sisoiev, UK
Christos H. Skiadas, Greece
Davide Spinello, Canada
Sri Sridharan, USA
Rolf Stenberg, Finland
Changyin Sun, China
Jitao Sun, China
Xi-Ming Sun, China
Andrzej Swierniak, Poland
Yang Tang, Germany
Allen Tannenbaum, USA
Cristian Toma, Romania
Irina N. Trendafilova, UK
Alberto Trevisani, Italy
Jung-Fa Tsai, Taiwan
K. Vajravelu, USA
Victoria Vampa, Argentina
Josep Vehi, Spain
Stefano Vidoli, Italy
Xiaojun Wang, China
Dan Wang, China
Youqing Wang, China
Yongqi Wang, Germany
Cheng C. Wang, Taiwan

Moran Wang, China
Yijing Wang, China
Gerhard-Wilhelm Weber, Turkey
J. A. S. Witteveen, The Netherlands
Kwok-Wo Wong, Hong Kong
Ligang Wu, China
Zhengguang Wu, China
Gongnan Xie, China
Wang Xing-yuan, China
Xi Frank Xu, USA
Xuping Xu, USA
Jun-Juh Yan, Taiwan
Xing-Gang Yan, UK
Suh-Yuh Yang, Taiwan
Mahmoud T. Yassen, Egypt
Mohammad I. Younis, USA
Bo Yu, China
Huang Yuan, Germany
S.P. Yung, Hong Kong
Ion Zaballa, Spain
Ashraf M. Zenkour, Saudi Arabia
Jianming Zhan, China
Xu Zhang, China
Yingwei Zhang, China
Lu Zhen, China
Liancun Zheng, China
Jian Guo Zhou, UK
Zexuan Zhu, China
Mustapha Zidi, France

Contents

Smart Control Algorithms and Technology in Civil Infrastructures, Hongnan Li, Gangbing Song, Jeong-Tae Kim, and Gang Li
Volume 2014, Article ID 842802, 2 pages

Study on Optimal Placement and Reasonable Number of Viscoelastic Dampers by Improved Weight Coefficient Method, Ji-ting Qu and Hong-nan Li
Volume 2013, Article ID 358709, 10 pages

Recentering Shape Memory Alloy Passive Damper for Structural Vibration Control, Hui Qian, Hongnan Li, Gangbing Song, and Wei Guo
Volume 2013, Article ID 963530, 13 pages

A Static Control Algorithm for Adaptive Beam String Structures Based on Minimal Displacement, Yanbin Shen, Huaqiang Cheng, Pengcheng Yang, and Yaozhi Luo
Volume 2013, Article ID 713768, 10 pages

Optimal Design of Liquid Dampers for Structural Vibration Control Based on GA and H_∞ Norm, Linsheng Huo, Wenhe Shen, Hongnan Li, and Yaowen Zhang
Volume 2013, Article ID 191279, 10 pages

A Constitutive Model for Superelastic Shape Memory Alloys Considering the Influence of Strain Rate, Hui Qian, Hongnan Li, Gangbing Song, and Wei Guo
Volume 2013, Article ID 248671, 8 pages

Study on Seismic Control of Power Transmission Tower-Line Coupled System under Multicomponent Excitations, Li Tian, Qiqi Yu, and Ruisheng Ma
Volume 2013, Article ID 829415, 12 pages

Application of Fuzzy Control with Market-Based Control Strategy to Structures, Gang Li, Hong-Nan Li, and Qi-Feng Liu
Volume 2013, Article ID 132010, 8 pages

Numerical Study on Nonlinear Semiactive Control of Steel-Concrete Hybrid Structures Using MR Dampers, Long-He Xu, Zhong-Xian Li, and Yang Lv
Volume 2013, Article ID 401410, 9 pages

Editorial

Smart Control Algorithms and Technology in Civil Infrastructures

Hongnan Li,¹ Gangbing Song,² Jeong-Tae Kim,³ and Gang Li¹

¹ Faculty of Infrastructure Engineering, Dalian University of Technology, Dalian 116023, China

² Department of Mechanical Engineering Director, Smart Materials and Structures Laboratory, University of Houston, Houston, TX 77004, USA

³ Department of Ocean Engineering, Pukyong National University, Busan 608-737, Republic of Korea

Correspondence should be addressed to Gang Li; gli@dlut.edu.cn

Received 18 December 2013; Accepted 18 December 2013; Published 20 January 2014

Copyright © 2014 Hongnan Li et al. This is an open access article distributed under the Creative Commons Attribution License, which permits unrestricted use, distribution, and reproduction in any medium, provided the original work is properly cited.

Structural control technology has made considerable progress by developing theoretical and experimental researches. Following the emerging of complex structures such as the ultrahigh and long-span infrastructure, the conventional control strategy for structures in civil engineering gradually exposes limitation in the computation time, robustness, stability, and so forth, while smart control algorithms and technologies being introduced or incorporated in the structural control technology solve the above problems. In addition, new smart materials, for example, shape memory alloy, replacing traditional general materials, such as steel and rubber, improve controllers' performance.

This special issue accepted and published 9 papers, the content of which falls into two broad categories: smart control algorithms and smart materials (or controllers). These novelty research works were applied widely to infrastructure engineering, for instance, steel framed structures, reinforced concrete buildings, and power transmission tower-line system.

The market-based control as a control strategy is developed based on an analogy between the control force-energy source in the structural area and the supply-demand in the free market. Since the supply-demand relation model and iteration procedure for the optimal price solution are necessary and relatively hard to understand and perform for civil engineers, therefore, G. Li et al. established an equivalent fuzzy logical rule to replace the existing market-based control method.

L. Huo et al. conducted the optimal design of liquid dampers for the seismic response control of structures and selected the H_∞ norm of the transfer function from the ground motion to the structural response as the optimal objective. The optimization procedure is carried out by using genetic algorithms in order to reach an optimal solution. The proposed method has the unnecessary advantage to solve the equation of motion for the control system, and the obtained optimal parameters of dampers are not dependent on the ground motion records. The results show that the structural responses can be effectively reduced and subjected to earthquake excitation at different sites.

A semiactive control platform based on magnetorheological dampers comprising the Bouc-Wen model, the semiactive control law, the shear wall damage criteria, and steel damage material model is developed in LS-DYNA program, based on the data transferring between the main program and the control platform by L. Xu et al. The nonlinear seismic control effectiveness is verified by the numerical example of a 15-story steel-concrete hybrid structure, and results indicate that the control platform and the numerical method are stable and fast; the relative displacement, shear force, and damage of the steel-concrete structure are largely reduced using optimal designed MR dampers; and the deformations and shear forces of the concrete tube and frame are better consorted by the control devices.

Y. Shen et al. presented a static control algorithm for adaptive beam string structures based on the nonlinear finite element method and simulated annealing algorithm. An

optimization model of adaptive beam string structures with multiple active struts is established, which uses a sensitivity analysis method. A nonlinear iteration procedure is used afterwards to calibrate the results of linear calculation.

H. Qian et al. investigated the properties of superelastic NiTi shape memory alloys and emphasized on the influence of strain rate on superelastic behavior under various strain amplitudes by cyclic tensile tests. A novel constitutive equation is proposed to describe the strain-rate dependent hysteretic behavior of superelastic shape memory alloys at different strain levels. Numerical simulation results based on the proposed constitutive equation and experimental results are in good agreement. The findings in this paper will assist the future design of superelastic SMA-based energy dissipation devices for the seismic protection of structures. Moreover, H. Qian et al. presented a preliminary study on the evaluation of an innovative energy dissipation system with the shape memory alloys for structural seismic protection. A recentering shape memory alloy damper was utilized as energy dissipation components, and improved constitutive equations based on the existing model were proposed for superelastic Nitinol wires and used in the damper. Cyclic tensile-compressive tests on the damper with various pre-strain under different loading frequency and displacement amplitude were conducted.

L. Tian et al. carried out the seismic control of power transmission tower-line coupled system subjected to multi-component excitations. The schematic of tuned mass damper is introduced, and equations of motion of a system with the tuned mass damper under multicomponent excitations are proposed. The time domain analysis takes into account the geometric nonlinearity due to the finite deformation. The optimal design of the transmission tower-line system with the tuned mass damper is obtained according to the different mass ratio.

In summary, the topics of smart control algorithms, materials, and technologies in infrastructure engineering are discussed in this special issue. Most problems, which are relatively difficult to answer using the traditional methods, such as actuators optimization, robustness improvement, and control law rule simplifications, were solved with various degrees. We hope that smart control algorithms and technologies are thought to have tendency and the effective approach to handling current issues existing in the structural control area, and the involved papers contribute to further advance in the area of smart control in civil engineering.

Acknowledgments

All guest editors would like to thank the investigators for their contributions and the referees for their efforts on reviewing the papers.

*Hongnan Li
Gang Li
Gangbing Song
Jeong-Tae Kim*

Research Article

Study on Optimal Placement and Reasonable Number of Viscoelastic Dampers by Improved Weight Coefficient Method

Ji-ting Qu^{1,2} and Hong-nan Li¹

¹ Faculty of Infrastructure Engineering School of Civil Engineering, Dalian University of Technology, Dalian 116024, China

² State Key Laboratory of Structural Analysis for Industrial Equipment, Dalian University of Technology, Dalian 116024, China

Correspondence should be addressed to Ji-ting Qu; qjt@dlut.edu.cn

Received 19 July 2013; Revised 18 November 2013; Accepted 18 November 2013

Academic Editor: Gangbing Song

Copyright © 2013 J.-t. Qu and H.-n. Li. This is an open access article distributed under the Creative Commons Attribution License, which permits unrestricted use, distribution, and reproduction in any medium, provided the original work is properly cited.

A new optimal method is presented by combining the weight coefficient with the theory of force analogy method. Firstly, a new mathematical model of location index is proposed, which deals with the determination of a reasonable number of dampers according to values of the location index. Secondly, the optimal locations of dampers are given. It can be specific from stories to spans. Numerical examples are illustrated to verify the effectiveness and feasibility of the proposed mathematical model and optimal method. At last, several significant conclusions are given based on numerical results.

1. Introduction

Structural control protects structures and resists earthquakes by placing many types of energy dissipaters. Several passive as well as active methods and techniques have been developed [1–7]. Viscoelastic dampers (VED) have shown to be effective energy dissipation devices for structures under wind and seismic actions. To design a structure with energy dissipation devices, the placement of dampers has moderate influence on structural responses and the achievement of design objectives. Up to now, various methods in placing dampers have been studied, such as topological optimization [8], simulated annealing optimization [9], gradient-based method [10, 11], and genetic algorithm [12, 13]. These approaches usually do the step-by-step time history analysis many times by the circulation approximation when they are applied to the optimal placement of dampers for high-rise structures.

As an effective method among them, Zhang et al. [14] suggested a weight coefficient method for choosing parameters and locations of VEDs. On the premise that the amount of dampers is fixed, the number of dampers located on each story can be determined according to the ratio of the control indices of each story to the sum of them. This method is advantageous to calculate the number of dampers placed on each story all at once and bring great applicability in high-rise structures with energy dissipation devices. However, this

method is introduced for placing dampers on stories on the assumption of a certain amount of dampers and hardly can provide basis and recommendation on the placement in spans.

The force analogy method (FAM) was first proposed by Lin [15] for the inelastic analysis in continuum mechanics. Hart and Wong [16] extended this method into the dynamic analysis of nonlinear structures, while Wong and Yang [17] proposed a new algorithm based on this method formulated in the force-deformation space for inelastic dynamic analysis. The state space approach is mainly used in the FAM, which is a kind of time domain method based on state variables in modern control theories and is quite convenient for the time history analysis. Except the structural response history, the rotation history and hysteretic loops of plastic hinges are also available according to the FAM, thus providing possibilities of analysis for strain-softening and elastic-plastic properties, in which traditional methods cannot be completed. Besides, the plastic energy dissipation can be determined on each component. Combined with the hysteretic loops of dissipation devices, plastic hinges' transformations and order of appearance could be monitored for structures under earthquake excitations [18].

The main objective of this research is to study the optimization of VEDs. The weight coefficient method is improved based on the FAM theory and a new mathematical model of

location optimization will be established, which is suitable for determining the amount of dampers and the specific location of VEDs in spans. Numerical analyses are illustrated to verify effectiveness and feasibility of the improved method and the new location index for the optimization of dampers and structural control, which supplies beneficial reference to further optimizations.

2. Energy Equation in Force Analogy Method

2.1. Principle of Force Analogy Method. The fundamental principle of the FAM is that each inelastic deformation is formulated as a degree of freedom and the force is calculated through varying displacement instead of varying stiffness, which means that the initial stiffness matrix can be used throughout the inelastic analysis. The FAM uses inelastic displacement as the variable rather than stiffness, with high efficiency and accuracy in analyzing inelastic responses. It is the premise of the theory that the whole deformation can be considered as the accumulation of local deformation. Plastic hinges are used to simulate structural plasticity in this method.

The basic concept of the FAM was presented in detail by Wong and Yang [17] in the analysis of braced frames, so only a brief summary is provided as background. Studying from a single degree of freedom system (SDOF), the inelastic responses are expressed by varying a displacement field as shown in Figure 1. In this figure, the total displacement $x(t)$ because of external force $F(t)$ is divided into two parts: the elastic displacement $x'(t)$ and the inelastic displacement $x''(t)$. The inelastic deformation of the structure is considered to be concentrated on the ends of the beams and columns, which is presented by the inelastic rotation of the plastic hinge $\theta''(t)$. The restoring force in the system $F_s(t)$ is written as

$$\begin{aligned} F_s &= k_e x_y + k_t (x - x_y), \\ x' &= \frac{F_s}{k_e}, \\ x'' &= \begin{cases} 0, & x < x_y, \\ (x - x_y) \left(1 - \frac{k_t}{k_e}\right), & x > x_y, \end{cases} \end{aligned} \quad (1)$$

where k_e and k_t denote the initial and postyield stiffness, respectively and x_y and F_y , respectively, represent the yield displacement and yield force.

Then, the total moment $M(t)$ at the locations where plastic hinges may form can be expressed as

$$M(t) = M'(t) + M''(t) = \frac{3EI}{l^2} x(t) - \frac{3EI}{l} \theta''(t), \quad (2)$$

where $M'(t)$ denotes the elastic moment caused by elastic displacement and $M''(t)$ represents the residual moment because of inelastic displacement.

2.2. Energy Equations of Structures. The equation of motion for an n -degree-freedom structure subjected to an earthquake can be written as

$$M\ddot{X}(t) + C\dot{X}(t) + KX'(t) = -M\ddot{X}_g(t), \quad (3)$$

where M and C mean the $n \times n$ mass and inherent damping matrices of the structure, $X'(t)$ is the n -dimensional elastic displacement vector, $\dot{X}(t)$ and $\ddot{X}(t)$ are the relative velocity and acceleration vector of the n -dimension, and $\ddot{X}_g(t)$ implies the seismic excitation.

Define the absolute acceleration $\ddot{Y}(t)$ to be the sum of $\ddot{X}(t)$ and $\ddot{X}_g(t)$. Based on the structural dynamic equation under earthquakes and the fundamental principle of FAM, the energy equation can be gained as follows:

$$\begin{aligned} \int_{t=0}^{t=t_k} \ddot{Y}^T M dY + \int_{t=0}^{t=t_k} \dot{X}^T C dX + \int_{t=0}^{t=t_k} X'^T K dX' \\ + \int_{t=0}^{t=t_k} M'^T d\theta'' = \int_{t=0}^{t=t_k} \ddot{Y}^T M dX_g. \end{aligned} \quad (4)$$

The above equation shows the different forms of energy in the structure. They are the kinetic energy, damping energy, strain energy, plastic energy (PE), and input energy from left to right. Studies show that the input energy will be dissipated by the plastic energy and strain energy, and plastic energy is dissipated due to the development of plastic hinges, which can be viewed as

$$\begin{aligned} PE &= \int_{t=0}^{t=t_k} M'^T d\theta'' \\ &= \int_{t=0}^{t=t_k} \sum_{i=1}^m M_i'^T d\theta_i'' = \sum_{i=1}^m PE_i, \end{aligned} \quad (5)$$

where PE_i represents the plastic dissipation of the i th plastic hinge. For structures with dissipation devices, hysteretic loops of these devices and plastic dissipation of each plastic hinge can be gained using the force analogy method, which makes the energy specified. Plastic hinges may be overdeformed, leading to structural failure when subjected to a large earthquake. Thus, passive energy dissipation devices like the VEDs are used in structures to absorb energy from earthquakes.

3. Improved Weight Coefficient Method

3.1. Objective Function. To bring forward an objective function is a core concept in optimal design. To design a structure with energy dissipation devices, the optimal location of dampers can make the performance indices be restricted within desired objectives as the amount of dampers is fixed. The performance index of the weight coefficient method is the story-drift angle. On the premise that the number of dampers is fixed, the number of dampers placed on the i th story can be determined by

$$N_i = N \frac{\theta_i}{\sum_{i=1}^n \theta_i}, \quad (6)$$

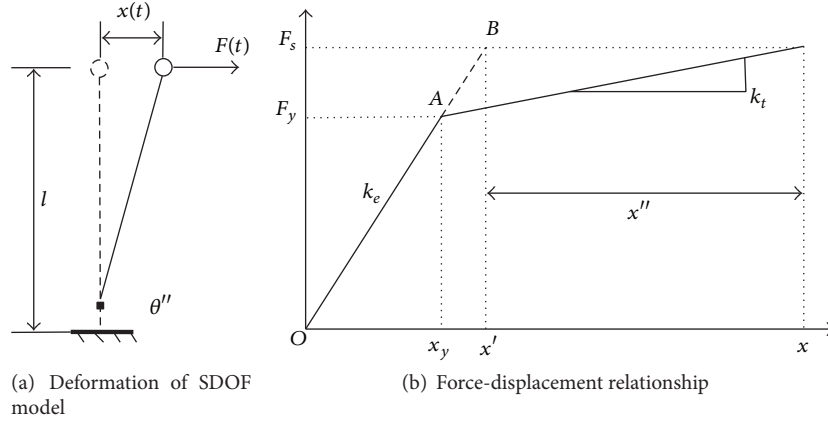


FIGURE 1: The principle of FAM.

where N is the amount of VEDs needed to be located on the whole structure, n is the number of stories, and θ_i represents the drift angle of the i th story. The number of dampers placed on the story can be calculated by using the above formulation of the weight coefficient method on the assumption of N , but the specific locations of them in spans are not determined.

Combining the weight coefficient method with the force analogy method, in this paper, a new objective function of optimal location for the VEDs is proposed. The aim is to place dampers on the locations where the hysteretic energy dissipation is large. Because the hysteretic energy dissipation is considered as the sum of the plastic energy of each member in the FAM, the plastic energy due to the inelastic deformation of each span is taken as the performance index which can be evaluated using the FAM. The optimal index can be written in the following form:

$$\rho_l = \frac{w_l}{\max(w_i)} \quad (i = 1, 2, \dots, r), \quad (7)$$

where w_l denotes the sum of plastic energy of two beam ends on the l th span, $\max(w_i)$ represents the maximum value of plastic energy of all the spans, r is the number of spans of a structure, and ρ_l denotes the objective function of the l th span. The values of the optimal index can be calculated for the structure subjected to earthquakes according to Section 2.

For the case that the location index ρ_l is greater than or equal to different values, the amount of dampers N needed to be placed on the structure can be determined. The number of dampers on each story can be calculated all at once based on the principle of the weight coefficient method in the following form:

$$N_k = N \frac{W_k}{\sum_{i=1}^n W_i}, \quad (8)$$

$$W_k = \sum_{i=1}^m w_i,$$

where m means the number of spans of each story and W_k represents the total plastic energy of the k th story.

At last, the specific location of dampers in each span can be determined according to the number of dampers on each story and the value of the location index. In other words, the dampers should be arranged in the span where the index values are larger.

3.2. Optimal Design Process Based on Improved Weight Coefficient. Based on the improved weight coefficient method and the process of dynamic analysis of the structures, the steps of the optimal design process are as follows.

- (1) Do step-by-step time history analysis of system without dampers by inputting records of earthquakes.
- (2) Calculate the values of optimal indices of all spans according to formula (7).
- (3) Set a target value of the location index according to the target of damping rate and determine the amount of dampers for the structure.
- (4) Confirm the number of dampers on each story by using formulae (8).
- (5) Make certain of the specific location of dampers according to the values of the position index and the number of each story.
- (6) Do step-by-step time history analysis of the controlled structure with dampers subjected to earthquakes and analyze whether or not the effective reduction of structural responses is satisfied.

The system analysis and optimal design procedures of dampers are programmed by adopting the MATLAB programming language.

4. Numerical Analysis

4.1. Structural Model. A 15-story, 3-span moment resisting frame [19] is considered. The serial number of plastic hinges and spans of the structure is shown in Figure 2. The mechanical properties are provided in Table 1. The mass is 56,430 kg of each floor, the span is 6.6 m, and the height of each story is 3.3 m. The stress-strain relation of steel is considered to

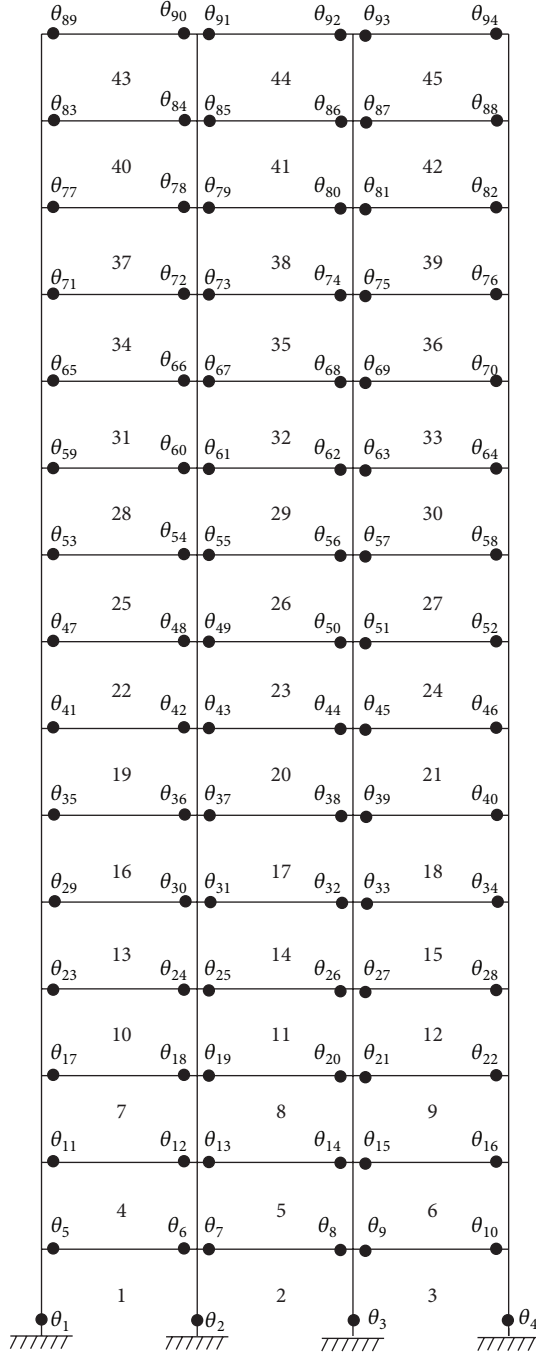


FIGURE 2: The serial number of plastic hinges and spans of the structure.

be ideal elastic-plastic with the modulus of elasticity $E = 2.06 \times 10^7$ N/mm. The yield stress of the steel members is 345 MPa. The increase of strength caused by strain-hardening and axial deformations is ignored.

4.2. Earthquake Records. Four seismic records are chosen as the input earthquake ground accelerations to the structure in this paper as shown in Table 2. The values of peak ground accelerations are scaled to 400 gal, 1200 gal, 600 gal, and

TABLE 1: Mechanical properties of the structure.

Member	Type of section	Material
Columns of 1~3 story	H400 × 400 × 30 × 50	Q345
Columns of 4~5 story	H400 × 400 × 25 × 40	
Columns of 6~8 story	H400 × 400 × 20 × 35	
Columns of 9~10 story	H400 × 400 × 20 × 32	
Columns of 11~15 story	H400 × 400 × 18 × 28	
Beams of 1~15 story	H500 × 300 × 12 × 25	

200 gal to make structures perform inelastically so as to calculate dampers' location indices.

4.3. Optimal Results. Compared with traditional energy analysis, the computational method based on the FAM is highly efficient and accurate. It utilizes the change in displacement to represent the inelastic behavior of the structure instead of changing stiffness. The plastic energy of each member is calculated according to Section 2.2 and the optimization process is programmed by adopting the MATLAB programming language.

Structural plastic energy is equal to the sum of individual plastic dissipations at each plastic hinge, which are computed by the MATLAB program. According to the index formula (7), location indices are calculated. For the case that the location index ρ_l is greater than or equal to 0.8, 0.6 and 0.4, the amount of dampers needed to be placed on the structure are 12, 20, and 24, respectively, termed as cases 1, 2, and 3. Take case 1 as an example, the calculation of optimal location is shown in Table 3. Compared with the original weight coefficient method, which can be applied on the premise that the number of dampers is fixed, the improved method can determine the reasonable number of dampers needed according to the location index and the engineering requirement.

The number of dampers placed on each story for three cases subjected to different earthquakes can be obtained as shown in Table 4. The results indicate that dampers are mainly located on the bottom and middle part of the structure for three cases. The number of dampers placed on the bottom and middle part increases with the addition of the amount from case 1 to 3. But the effect on the placement of dampers on the top part of the structure is not obvious.

The results of location indices indicate that values of side spans are generally greater than middle spans on the bottom and middle part of the structure, which is the basis of position selection for each story. The zero value of the location index denotes that there is no plastic energy for the member end. In other words, the corresponding part yields no plastic hinges under the action of earthquakes. The optimal placement of dampers for three cases can be obtained according to the above results, as shown in Figures 3, 4, and 5.

The original weight coefficient method can only determine the number of dampers on each floor. For example, if two dampers are needed for the building on the first floor, the dampers are usually each placed on the side span according to experience. However, the improved method can determine

TABLE 2: Earthquake records.

Records	Component	Interval(s)	Time(s)	Peak value (cm/s ²)
1940, El Centro, CALIF	NS	0.02	30	431.7
1994, Northridge, Tarzana-Cedar Hill Nursery A	NS	0.02	60	847.5
1979, Imperial Valley, Superstition Mountain, CA	S45E	0.02	28.34	146.4
1976, Tianjin Hospital, Ninghe	NS	0.01	19.19	145.8

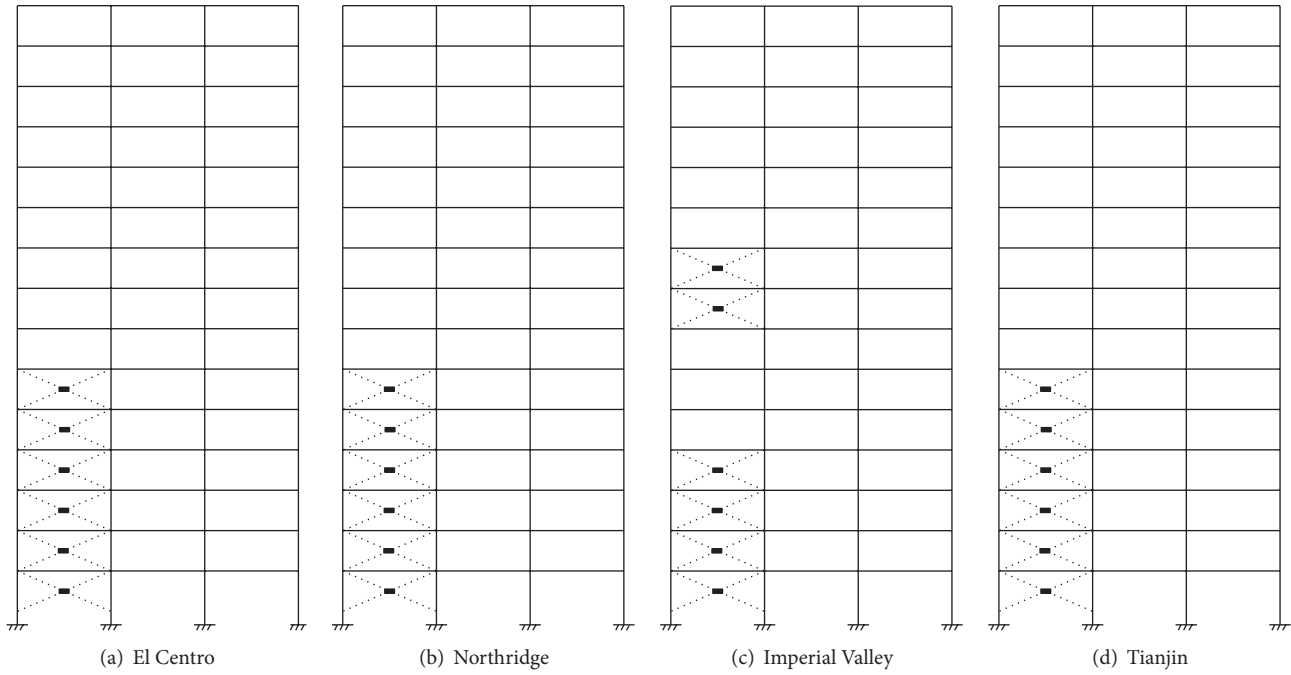


FIGURE 3: Optimal location of dampers for case 1.

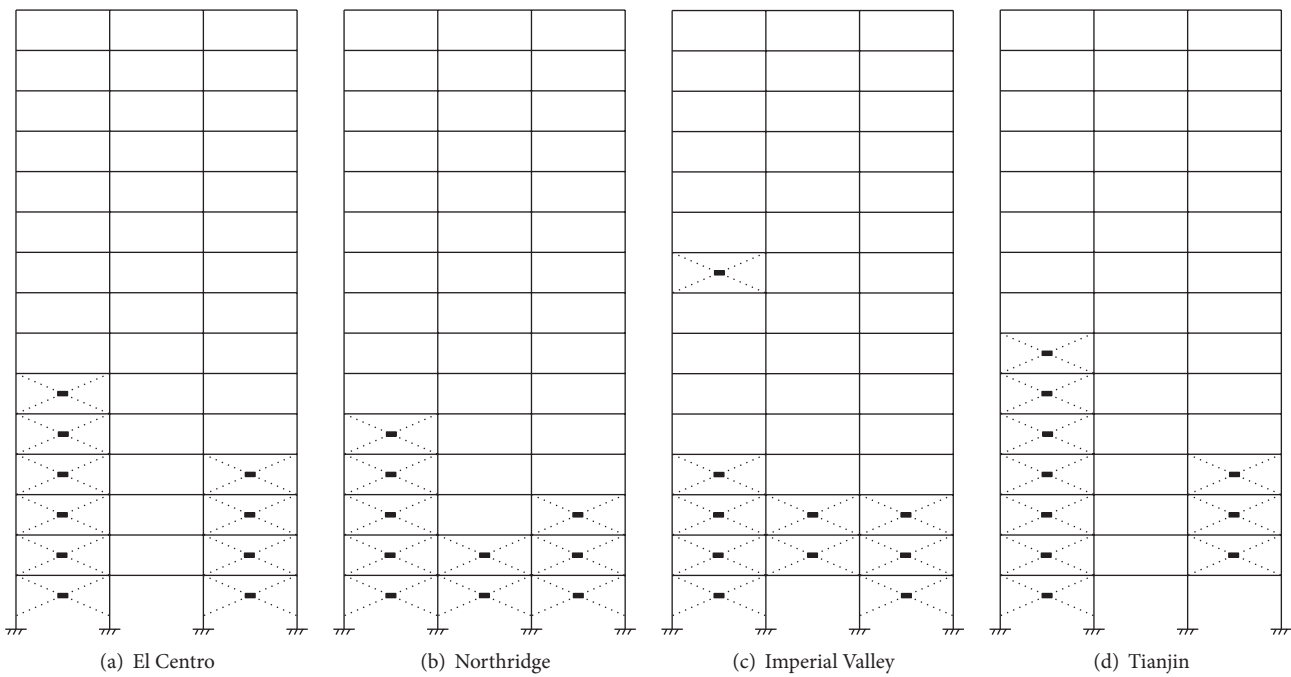


FIGURE 4: Optimal location of dampers for case 2.

TABLE 3: Optimal calculation for case 1.

Story	Earthquake	W_k	$\sum_{i=1}^n W_i$	$W_k / \sum_{i=1}^n W_i$	$N(W_k / \sum_{i=1}^n W_i)$	N_k
1	El Centro	130780	857718.6	0.15	1.83	2
	Northridge	81339.5	308790.3	0.26	3.16	3
	Imperial Valley	35064.82	145344.4	0.24	2.90	3
	Tianjin	122828.9	889286.3	0.14	1.66	2
2	El Centro	179236.4	857718.6	0.21	2.51	3
	Northridge	104232.8	308790.3	0.34	4.05	3
	Imperial Valley	46811.38	145344.4	0.32	3.86	3
	Tianjin	177512.9	889286.3	0.20	2.40	2
3	El Centro	170634.2	857718.6	0.20	2.39	2
	Northridge	73045.34	308790.3	0.24	2.84	3
	Imperial Valley	36157.5	145344.4	0.25	2.99	3
	Tianjin	170438.9	889286.3	0.19	2.30	2
4	El Centro	142590.5	857718.6	0.17	1.99	2
	Northridge	33427.78	308790.3	0.11	1.30	2
	Imperial Valley	17779.92	145344.4	0.12	1.47	2
	Tianjin	143765.5	889286.3	0.16	1.94	2
5	El Centro	96344.12	857718.6	0.11	1.35	1
	Northridge	13383.64	308790.3	0.04	0.52	1
	Imperial Valley	622.46	145344.4	0.00	0.00	0
	Tianjin	114449.4	889286.3	0.13	1.54	2
6	El Centro	64871.4	857718.6	0.08	0.91	1
	Northridge	3361.22	308790.3	0.01	0.13	0
	Imperial Valley	0	145344.4	0.00	0.00	0
	Tianjin	77249.5	889286.3	0.09	1.04	1
7	El Centro	42150.96	857718.6	0.05	0.59	1
	Northridge	0	308790.3	0.00	0.00	0
	Imperial Valley	555.78	145344.4	0.00	0.00	0
	Tianjin	48947.2	889286.3	0.06	0.66	1
8	El Centro	18588.14	857718.6	0.02	0.26	0
	Northridge	0	308790.3	0.00	0.00	0
	Imperial Valley	2315.88	145344.4	0.02	0.19	0
	Tianjin	22726.54	889286.3	0.03	0.31	0
9	El Centro	6705.2	857718.6	0.01	0.09	0
	Northridge	0	308790.3	0.00	0.00	0
	Imperial Valley	2974.04	145344.4	0.02	0.25	1
	Tianjin	9685.74	889286.3	0.01	0.13	0
10	El Centro	4511.84	857718.6	0.01	0.06	0
	Northridge	0	308790.3	0.00	0.00	0
	Imperial Valley	2424.72	145344.4	0.02	0.20	0
	Tianjin	1681.68	889286.3	0.00	0.00	0
11	El Centro	1305.86	857718.6	0.00	0.00	0
	Northridge	0	308790.3	0.00	0.00	0
	Imperial Valley	637.92	145344.4	0.00	0.05	0
	Tianjin	0	889286.3	0.00	0.00	0
12	El Centro	0	857718.6	0.00	0.00	0
	Northridge	0	308790.3	0.00	0.00	0
	Imperial Valley	0	145344.4	0.00	0.00	0
	Tianjin	0	889286.3	0.00	0.00	0

TABLE 3: Continued.

Story	Earthquake	W_k	$\sum_{i=1}^n W_i$	$W_k / \sum_{i=1}^n W_i$	$N(W_k / \sum_{i=1}^n W_i)$	N_k
13	El Centro	0	857718.6	0.00	0.00	0
	Northridge	0	308790.3	0.00	0.00	0
	Imperial Valley	0	145344.4	0.00	0.00	0
	Tianjin	0	889286.3	0.00	0.00	0
14	El Centro	0	857718.6	0.00	0.00	0
	Northridge	0	308790.3	0.00	0.00	0
	Imperial Valley	0	145344.4	0.00	0.00	0
	Tianjin	0	889286.3	0.00	0.00	0
15	El Centro	0	857718.6	0.00	0.00	0
	Northridge	0	308790.3	0.00	0.00	0
	Imperial Valley	0	145344.4	0.00	0.00	0
	Tianjin	0	889286.3	0.00	0.00	0

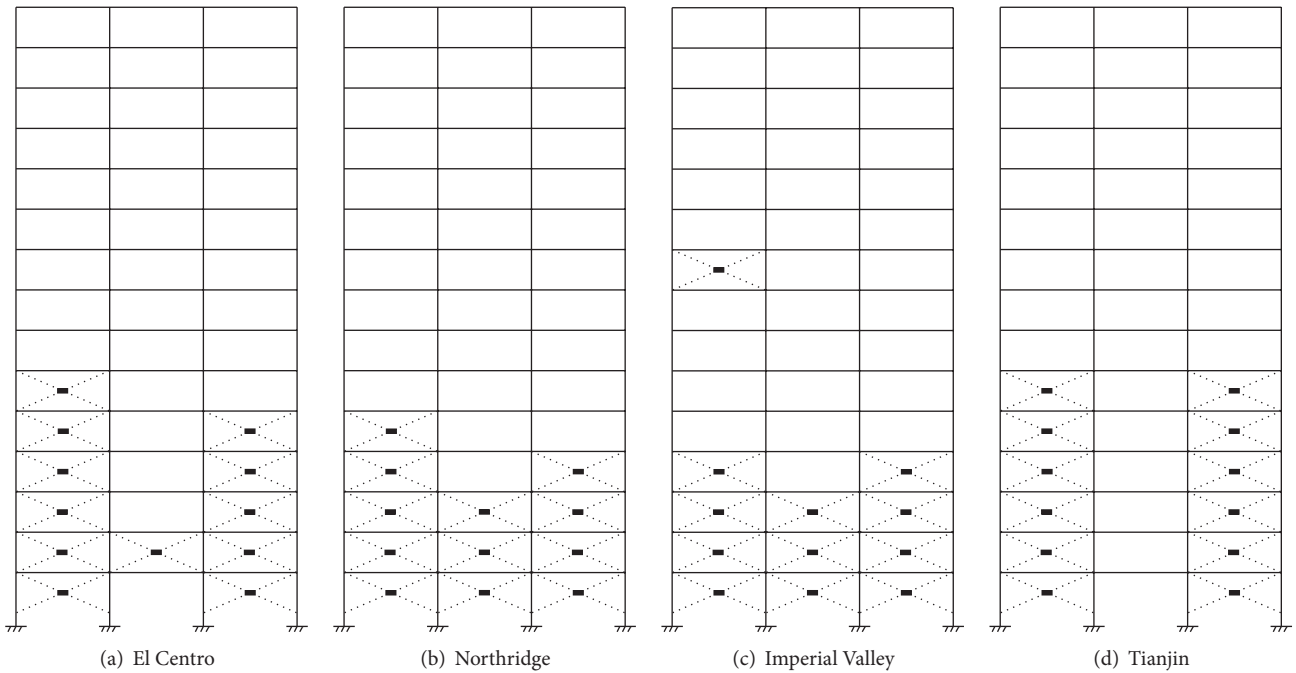


FIGURE 5: Optimal location of dampers for case 3.

the specific location of dampers in spans according to the value of the location index.

4.4. Time History Analysis of the Structures with VEDs. A number of force-deformation relationship models of VEDs have been brought forward and they are applicable to different conditions. The Maxwell model is adopted. When the dampers are located in structures according to the optimal results, the step-by-step time history analysis is utilized by using the SAP 2000 to obtain the responses of structures for each of the three cases. The maximum displacements of the structure with and without dampers are compared as shown in Figure 6. The story drifts of the structure with optimally located dampers are calculated as shown in Tables 5, 6, and

7. The story drifts of the structure with and without dampers are compared as shown in Figure 7.

From the view of the above tables and figures, structural displacements are controlled well and decrease obviously when dampers are placed optimally. Also, the displacement distributions are more even. For case 1, the story drifts of the controlled structure decrease by 20%~35%, while for case 2 they decrease by 25%~60% and for case 3 they decrease by 25%~65%. On the other hand, the more dampers used, the better the effect on energy dissipation of structures. Considering space limits and economy, the reasonable quantity of dampers can be determined by setting the feasible value of the location index to meet actual requirements. The value of the location index should be taken as 0.6 for the example for

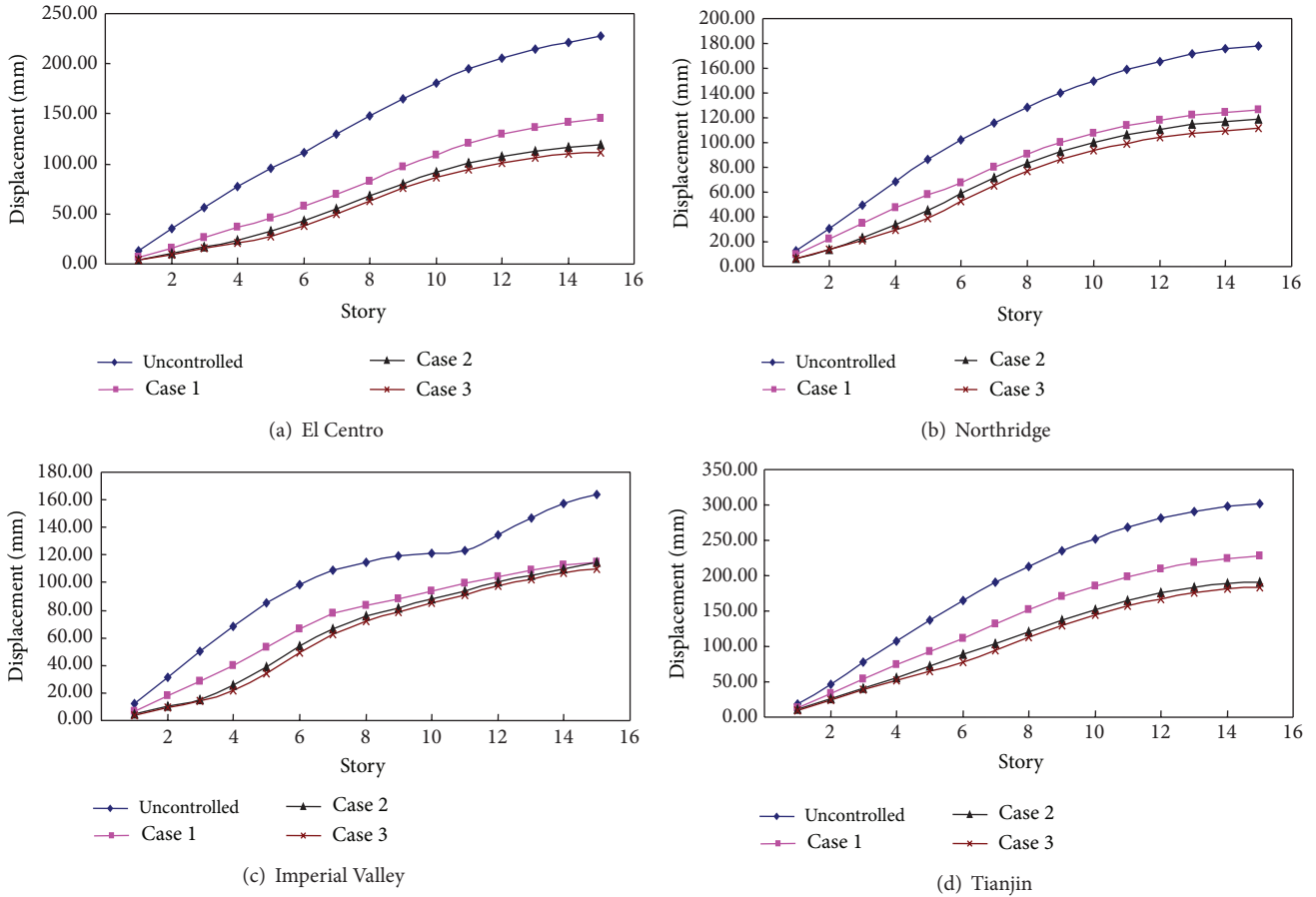


FIGURE 6: Comparison of maximum displacements of structure with and without dampers.

TABLE 4: Number of dampers on each story for three cases.

Case	Earthquake	Story									
		1	2	3	4	5	6	7	8	9	10-15
1	El Centro	2	2	2	2	2	2	0	0	0	0
	Northridge	2	2	2	2	2	2	0	0	0	0
	Imperial Valley	2	2	2	2	0	0	0	2	2	0
	Tianjin	2	2	2	2	2	2	0	0	0	0
	Uncontrolled	0	0	0	0	0	0	0	0	0	0
2	El Centro	4	4	4	4	2	2	0	0	0	0
	Northridge	6	6	4	2	2	0	0	0	0	0
	Imperial Valley	4	6	6	2	0	0	0	0	2	0
	Tianjin	2	4	4	4	2	2	2	0	0	0
	Uncontrolled	0	0	0	0	0	0	0	0	0	0
3	El Centro	4	6	4	4	4	2	0	0	0	0
	Northridge	6	6	6	4	2	0	0	0	0	0
	Imperial Valley	6	6	6	4	0	0	0	0	2	0
	Tianjin	4	4	4	4	4	4	0	0	0	0
	Uncontrolled	0	0	0	0	0	0	0	0	0	0

TABLE 5: Story drift of the structure with dampers for case 1 (mm).

Story	El Centro	Northridge	Imperial Valley	Tianjin
1	6.38	9.19	7.09	13.06
2	9.59	13.15	10.75	20.25
3	10.02	12.76	10.86	20.44
4	10.18	11.79	11.50	20.05
5	10.08	10.66	13.19	18.77
6	11.05	10.17	13.31	18.88
7	12.37	12.04	10.82	20.44
8	13.02	10.74	6.24	19.63
9	13.77	8.99	4.63	17.95
10	12.61	7.44	5.58	15.69
11	11.16	6.34	5.25	13.74
12	9.16	4.87	5.14	11.12
13	7.02	3.66	4.63	8.40
14	5.48	2.65	3.87	5.65
15	3.32	1.87	2.22	3.02

both good response reduction and economy. From the aspect of placement of dampers, it can be seen that dampers are mostly placed at the bottom, middle part, and side spans of the structure for the three cases.

5. Conclusions

In this paper, an improved weight coefficient method is proposed and a new location index is given to optimize

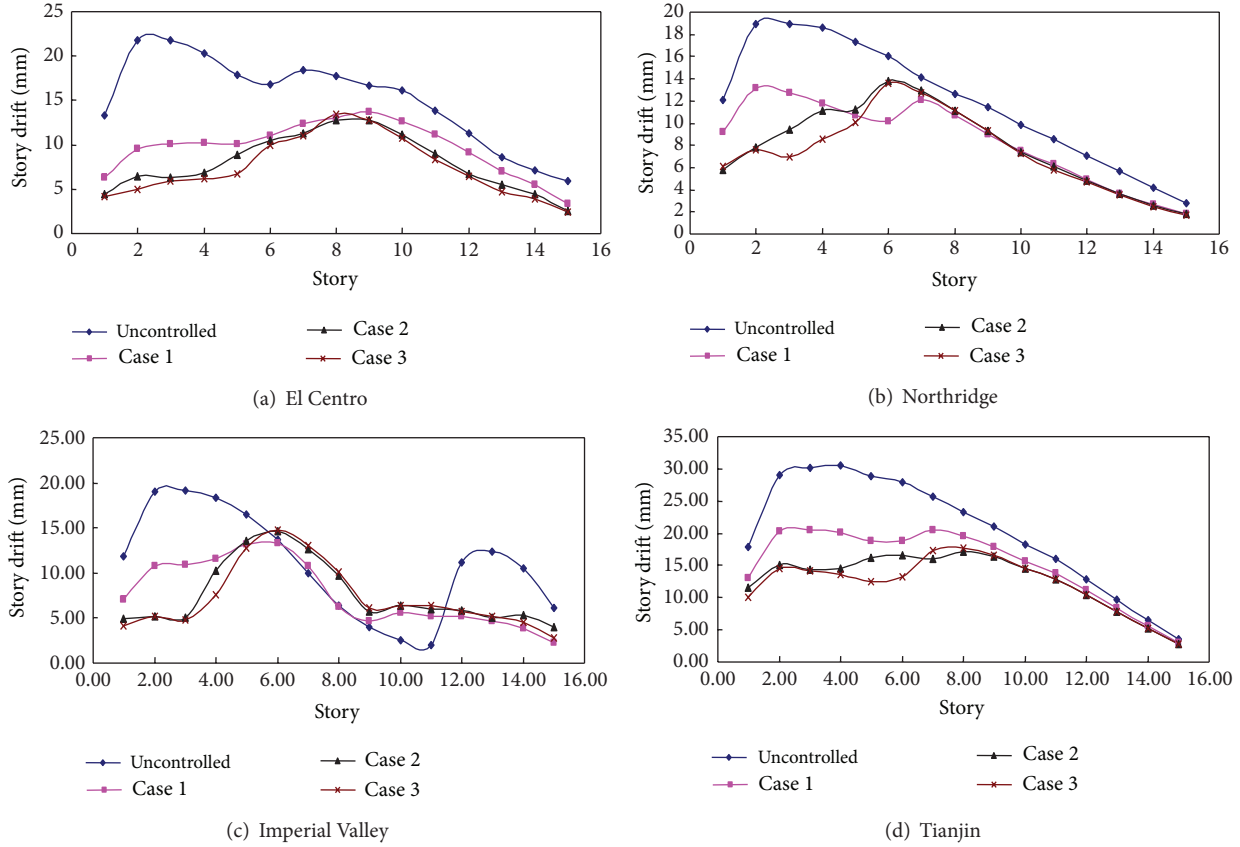


FIGURE 7: Comparison of story drift of the structure with and without dampers.

TABLE 6: Story drift of the structure with dampers for case 2 (mm).

Story	El Centro	Northridge	Imperial Valley	Tianjin
1	4.50	5.82	4.93	11.47
2	6.45	7.81	5.15	15.07
3	6.29	9.42	5.11	14.33
4	6.80	11.07	10.28	14.50
5	8.92	11.25	13.53	16.23
6	10.53	13.75	14.60	16.53
7	11.28	12.90	12.65	16.01
8	12.71	11.14	9.73	17.06
9	12.81	9.26	5.74	16.37
10	11.11	7.35	6.45	14.61
11	8.97	6.07	6.04	12.81
12	6.65	4.86	5.82	10.36
13	5.48	3.59	4.99	7.84
14	4.39	2.57	5.28	5.27
15	2.54	1.78	4.00	2.82

TABLE 7: Story drift of the structure with dampers for case 3 (mm).

Story	El Centro	Northridge	Imperial Valley	Tianjin
1	4.23	6.12	4.14	10.00
2	5.01	7.58	5.13	14.59
3	5.91	7.00	4.82	14.16
4	6.21	8.51	7.64	13.51
5	6.72	10.11	12.71	12.51
6	9.94	13.58	14.80	13.27
7	11.07	12.70	13.08	17.22
8	13.48	11.13	10.09	17.69
9	12.72	9.25	6.09	16.59
10	10.74	7.30	6.44	14.59
11	8.37	5.75	6.42	12.87
12	6.43	4.71	5.77	10.40
13	4.72	3.48	5.25	7.86
14	3.91	2.47	4.50	5.29
15	2.43	1.71	2.81	2.83

the reasonable number and locations of VEDs in structures based on the force analogy method. According to numerical simulations, a few conclusions can be drawn as follows.

(1) The structural displacement and story drift decrease a lot by using the raised optimal method, and the

effects are optimal in lower layers. Furthermore, the distribution of displacements is more reasonable, which leads to a full use of materials.

(2) It can be concluded that a greater number of dampers is preferable, while, in practical applications, the

amount of dampers should be confirmed wisely by setting the value of the location index with structural characteristics, dissipation effects, and economy all taken into consideration.

- (3) The method presented here can not only specify the placement of dampers from layers to spans but also carry on the advantages of high efficiency and accuracy from the force analogy method, which is of great applicability.
- (4) The improved weight coefficient method and new location index can be applied to the optimal design of the structure with other types of passive energy dissipation dampers.

Acknowledgments

This research work was jointly supported by the Science Fund for Creative Research Groups of the NSFC (Grant no. 51121005), the National Natural Science Foundation of China (Grant no. 51108064), and the Fundamental Research Funds for the Central Universities (Grant no. DUT13LK26). The authors would like to thank the reviewers for their careful reading of the paper and their constructive criticism.

References

- [1] H. N. Li and S. Yan, "State-of-the-art review: researches and applications of structural control in China," *Earthquake Engineering and Engineering Vibration*, vol. 19, no. 1, pp. 107–112, 1999.
- [2] G. Song, P. Qiao, V. Sethi, and A. Prasad, "Active vibration control of a smart pultruded fiber-reinforced polymer I-beam," *Smart Materials and Structures*, vol. 13, no. 4, pp. 819–827, 2004.
- [3] G. Song and H. Gu, "Active vibration suppression of a composite I-beam using fuzzy positive position control," *Smart Materials and Structures*, vol. 14, no. 4, pp. 540–547, 2005.
- [4] V. Sethi and G. Song, "Multimodal vibration control of a flexible structure using piezoceramic sensor and actuator," *Journal of Intelligent Material Systems and Structures*, vol. 19, no. 5, pp. 573–582, 2008.
- [5] H. Gu, G. Song, and H. Malki, "Chattering-free fuzzy adaptive robust sliding-mode vibration control of a smart flexible beam," *Smart Materials and Structures*, vol. 17, no. 3, Article ID 35007, 2008.
- [6] V. Sethi, M. A. Franchek, and G. Song, "Active multimodal vibration suppression of a flexible structure with piezoceramic sensor and actuator by using loop shaping," *Journal of Vibration and Control*, vol. 17, no. 13, pp. 1994–2006, 2011.
- [7] L. Y. Li, G. Song, and J. P. Ou, "Adaptive fuzzy sliding mode based active vibration control of a smart beam with mass uncertainty," *Structural Control and Health Monitoring*, vol. 18, no. 1, pp. 40–52, 2011.
- [8] H. G. Natke and T. T. Soong, "Topological structural optimization under dynamic loads," in *Optimization of Structural Systems and Applications*, S. Hernandez and C. A. Brebbia, Eds., Computational Mechanics Publications, Southampton, UK, 1993.
- [9] M. H. Milman and C. C. Chu, "Optimization methods for passive damper replacement and tuning," *Journal of Guidance, Control, and Dynamics*, vol. 17, no. 4, pp. 848–856, 1994.
- [10] I. Takewaki, "Optimal damper placement for minimum transfer functions," *Earthquake Engineering and Structural Dynamics*, vol. 26, no. 11, pp. 1113–1124, 1997.
- [11] I. Takewaki, S. Yoshitomi, K. Uetani, and M. Tsuji, "Non-monotonic optimal damper placement via steepest direction search," *Earthquake Engineering and Structural Dynamics*, vol. 28, pp. 655–670, 1999.
- [12] M. P. Singh and L. M. Moreschi, "Optimal placement of dampers for passive response control," *Earthquake Engineering and Structural Dynamics*, vol. 31, no. 4, pp. 955–976, 2002.
- [13] J. T. Qu and H. N. Li, "Optimal placement of passive energy dissipation devices by genetic algorithms," *Mathematical Problems in Engineering*, vol. 2012, Article ID 474282, 21 pages, 2012.
- [14] Q. Zhang, W. J. Lou, and Y. Chen, "Parameter design and location optimum practical method of viscoelastic dampers," *Structural Engineers*, vol. 3, pp. 39–44, 2003.
- [15] T. H. Lin, *Theory of Inelastic Structures*, John Wiley & Sons, New York, NY, USA, 1968.
- [16] G. C. Hart and K. K. F. Wong, *Structural Dynamics for Structural Engineers*, John Wiley & Sons, New York, NY, USA, 2000.
- [17] K. K. F. Wong and R. Yang, "Inelastic dynamic response of structures using force analogy method," *Journal of Engineering Mechanics*, vol. 125, no. 10, pp. 1190–1200, 1999.
- [18] K. K. F. Wong and R. Yang, "Earthquake response and energy evaluation of inelastic structures," *Journal of Engineering Mechanics*, vol. 128, no. 3, pp. 308–317, 2002.
- [19] A. F. Sun and J. P. Ou, "Lateral action patterns and their effects on pushover seismic analysis of steel tall buildings," *Earthquake Engineering and Engineering Vibration*, vol. 28, no. 4, pp. 88–93, 2008.

Research Article

Recentering Shape Memory Alloy Passive Damper for Structural Vibration Control

Hui Qian,¹ Hongnan Li,² Gangbing Song,^{2,3} and Wei Guo⁴

¹ School of Civil Engineering, Zhengzhou University, Zhengzhou 45000, China

² Faculty of Infrastructure Engineering, Dalian University of Technology, Dalian 116024, China

³ Department of Mechanical Engineering, University of Houston, Houston, TX 77204, USA

⁴ School of Civil Engineering, Central South University, Changsha 410075, China

Correspondence should be addressed to Hui Qian; qianhui@zzu.edu.cn

Received 12 July 2013; Accepted 9 September 2013

Academic Editor: Gang Li

Copyright © 2013 Hui Qian et al. This is an open access article distributed under the Creative Commons Attribution License, which permits unrestricted use, distribution, and reproduction in any medium, provided the original work is properly cited.

This paper presents a preliminary study on the evaluation of an innovative energy dissipation system with shape memory alloys (SMAs) for structural seismic protection. A recentering shape memory alloy damper (RSMAD), in which superelastic nitinol wires are utilized as energy dissipation components, is proposed. Improved constitutive equations based on Graesser and Cozzarelli model are proposed for superelastic nitinol wires used in the damper. Cyclic tensile-compressive tests on the damper with various prestrain under different loading frequencies and displacement amplitudes were conducted. The results show that the hysteretic behaviors of the damper can be modified to best fit the needs for passive structural control applications by adjusting the pretension of the nitinol wires, and the damper performance is not sensitive to frequencies greater than 0.5 Hz. To assess the effectiveness of the dampers for structural seismic protection, nonlinear time history analysis on a ten-story steel frame with and without the dampers subjected to representative earthquake ground motions was performed. The simulation results indicate that superelastic SMA dampers are effective in mitigating the structural response of building structures subjected to strong earthquakes.

1. Introduction

Conventional structures rely on their adequate stiffness, strength, and ductility to survive earthquakes. Such a design strategy may not be economical, and may be ineffective for unexpected seismic events [1, 2]. In recent years, the design strategy based on the performance of civil structures has attracted increasing attentions of both practicing engineers and structure owners [3–5]. To enhance the seismic performance of structural systems, many possible strategies have been proposed [6, 7], and one promising family of solutions is the passive control techniques [8, 9].

By and large, current passive control applications are based on the following two techniques: seismic base isolation and energy dissipation [10]. Seismic isolation system relies on special ductile alternate layers which are installed between substructure and superstructure to reduce the transfer of seismic energy to the superstructure, thus protecting the superstructure's integrity [11]. Usually, in order to limit

the extent of the displacement, energy dissipation devices are incorporated into the alternate layers. Energy dissipation system incorporates special energy dissipation devices into the structures to absorb or consume a portion of the seismic energy, thereby reducing energy dissipation demand on primary structural members and minimizing possible structural damage [8]. Nowadays, several types of seismic energy dissipation devices, such as metallic dampers, friction dampers, viscoelastic dampers, and viscous fluid damper, are available. However, current technologies present some limitations, such as problems related to aging and durability, maintenance, reliability in the long run, substitution after strong events, and variable temperature-dependent performances, among others [12]. Recently, the increasing research and development of smart materials and controlling devices open up a new area for seismic vibration control of structural engineering, providing a basic platform for the design and exploration of new generation high-performance damping devices.

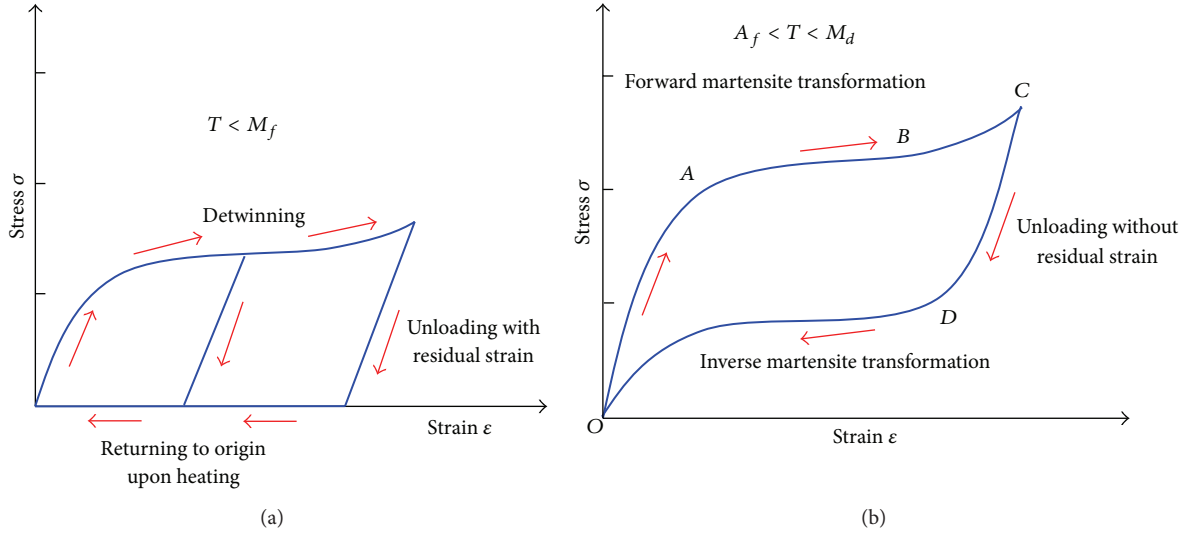


FIGURE 1: Stress-strain diagrams of NiTi shape memory alloy: (a) SME, $T < M_f$; (b) superelasticity, $A_f < T < M_d$.

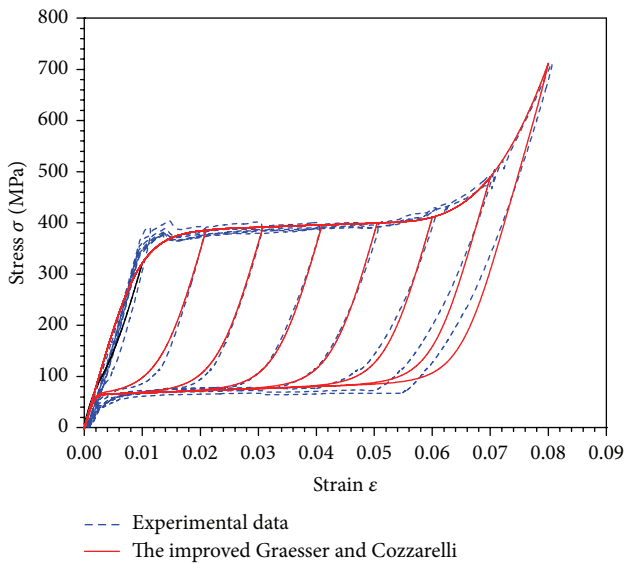


FIGURE 2: Stress-strain curves of superelastic nitinol wires.

Shape memory alloys [13] are a class of novel functional materials that possess unique properties, including shape memory effect (SME), superelasticity effect (SE), extraordinary fatigue resistance, high corrosion resistance, high damping characteristics, and temperature-dependent Young's modulus. At a low temperature, SMAs exhibit the SME—residual deformations can be recovered by heating the material above the austenite finish temperature, as shown in Figure 1(a). At a higher temperature, SMAs exhibit the SE, as shown in Figure 1(b). In the superelastic phase, SMAs are initially austenitic. However, upon loading, stress-induced martensite is formed. Upon unloading, the martensite reverts to austenite at a lower stress level, resulting in the hysteretic behavior. These properties make them ideal candidates for seismic energy dissipation devices in structural engineering.

A significant number of research studies have been conducted in an effort to use SMAs for applications in seismic resistant design and structural retrofit in the past decade (e.g., [14–24]). Wilde et al. [14] proposed a smart isolation system combining a laminated rubber bearing with a device made of SMA for highway bridges. Their analytical results show that the isolation system can limit displacement and dissipate energy for earthquake mitigation. Dolce et al. [15] developed two families of SMA-based energy dissipating and recentering braces for seismic vibration control of buildings and bridges, as outcomes of the MANSIDE project (Memory Alloys for New Seismic Isolation and Energy Dissipation Devices). To assess the effectiveness of SMA braces to reduce the seismic response of reinforced concrete (RC) framed structures, shaking table tests of a 1/3.3-scale, three-story, two-bay RC plane frame, which was designed for low seismicity and low ductility according to the European seismic code, were carried out by Dolce et al. [16]. Their experimental results show that the SMA braces can enhance seismic performances at least comparable to those provided by steel braces, while having an additional self-centering feature. Indirli et al. [17] retrofitted historic buildings using superelastic SMA tie bars to enhance its seismic resistance capacities. DesRoches and Delemont [18] and Andrawes and Desroches [19] evaluated the efficacy of superelastic nitinol bars as restrainers to reduce the risk of collapse from unseating of bridge superstructures at the hinges. They found that the SMA bars are effective in limiting relative hinge displacements in typical multiple frame bridges. Li et al. [20] investigated the vibration mitigation of a stay cable provided with one superelastic SMA damper. The analytical results show that the SMA damper can reduce cable vibration significantly and the control effectiveness is influenced by SMA damper parameters and locations. Zhang and Zhu [21] developed reusable hysteretic damper (RHD) based on superelastic nitinol stranded wires, and their numerical analysis indicated the effectiveness of RHD

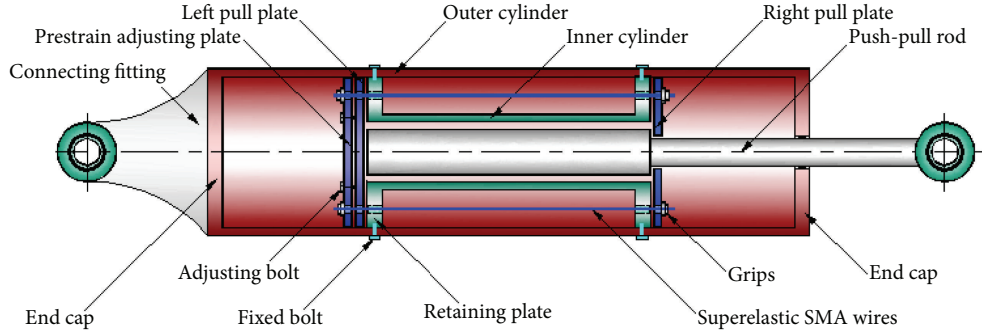


FIGURE 3: Diagram of RSMAD.



FIGURE 4: Photograph of experimental setup.

in passive seismic response control of structures. Ocel et al. [22] and McCormick et al. [23] investigated beam-column connections using SMA bars. Their studies show that SMA can enhance the seismic performance of the connections. Parulekar et al. [24] proposed a damper device using austenite NiTi wires. The device is tested and validated using a thermo-mechanical model of SMA taking into account the residual martensite accumulation. Performance of the structure with SMA dampers is compared with that of the same structure with yielding dampers.

Previous works show that SMAs are of promise in structural engineering, particularly as energy dissipation components for seismic protection. However, significant research is still needed. In Particular, designing new types of SMA-based passive seismic devices, which possess not only energy dissipation and recentering capabilities but also simple configuration for easy installation in the practical engineering, is still a challenge.

This paper presents an innovative recentering shape memory alloy damper (RSMAD) for seismic structural protection. The damper is simple in design and easy to implement. Superelastic nitinol wires were utilized in the damper as kernel energy dissipating components. Cyclic tensile-compressive tests on the damper model with various prestrain under different loading frequencies and displacements were conducted. To assess the effectiveness of the damper for

structural seismic protection, nonlinear time history analyses on a ten-story steel frame subjected to representative earthquake ground motions, with and without the dampers, were performed.

2. Constitutive Equation of Superelastic SMA Wire

With the wide applications of SMAs in different fields, modeling of the peculiar mechanical behavior of SMAs, such as SME and superelasticity, has been an active area of research over the past decades. So far, many constitutive models for SMA have been developed [25–33]. These models describe the thermomechanical, thermoelectrical, and thermochemical behaviors of SMAs; however, most of them are too complex to be convenient for practical application in earthquake engineering. In this paper, a relatively simple model developed by Graesser and Cozzarelli [34] is adopted. This model is an extension of a one-dimensional strain rate independent model for hysteretic behavior proposed by Özdemir [35]. The equation is given as

$$\dot{\sigma} = E \left[\dot{\varepsilon} - |\dot{\varepsilon}| \left(\frac{\sigma - \beta}{Y} \right)^n \right], \quad (1)$$

where σ and ε are the one-dimensional stress and the one-dimensional strain, respectively; E is the initial elastic modulus; Y is the yield stress; n is a constant assumed any positive odd real value controlling the sharpness of transition from the elastic state to the phase transformation; $\dot{\sigma}$ and $\dot{\varepsilon}$ denote the time derivative of the stress and strain, respectively; and β is the one-dimensional back stress, given by

$$\beta = E\alpha \{ \varepsilon_{in} + f_T |\varepsilon|^c \operatorname{erf}(a\varepsilon) [u(-\varepsilon\dot{\varepsilon})] \}, \quad (2)$$

where f_T , a , and c are material constants controlling the type and size of the hysteresis, the amount of elastic recovery during unloading, and the slope of the unloading stress plateau, respectively. When $f_T = 0$, the model is purely martensitic. When $f_T > 0$, the model predicts the superelastic behavior. α is a constant controlling the slope of the $\sigma - \varepsilon$ curve in the inelastic range, given by

$$\alpha = \frac{E_y}{E - E_y}, \quad (3)$$

where E_y is the slope of the $\sigma - \varepsilon$ curve in the inelastic range.

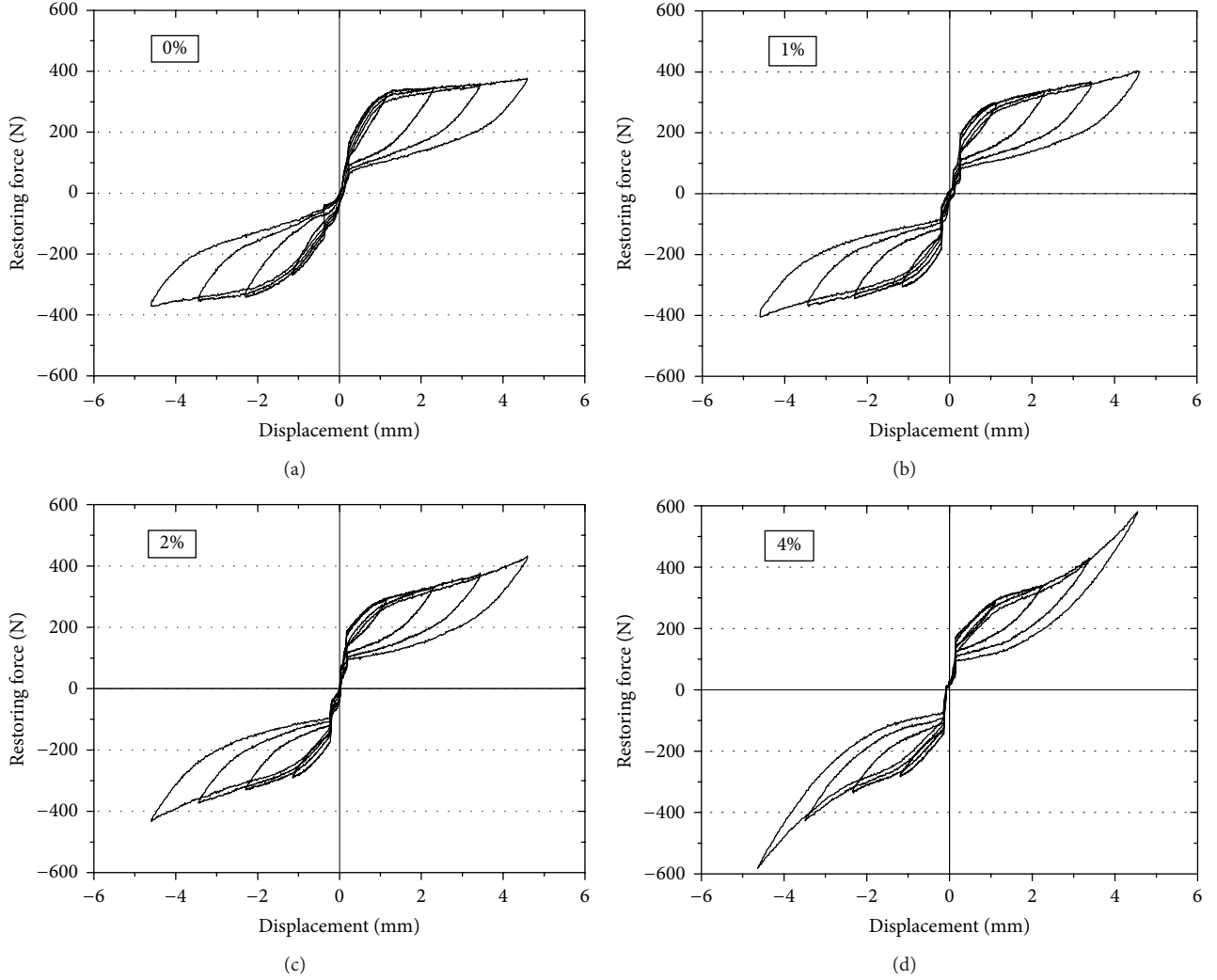


FIGURE 5: Hysteresis loops of the RSMAD at different prestrains and displacement amplitudes (0.05 Hz frequency of loading, 20°C temperature).

ε_{in} is the inelastic strain, given by

$$\varepsilon_{in} = \varepsilon - \frac{\sigma}{E}. \quad (4)$$

$u()$ is the unit step function, defined as

$$u(x) = \begin{cases} +1 & x \geq 0 \\ 0 & x < 0. \end{cases} \quad (5)$$

$\text{erf}()$ is the error function, defined by

$$\text{erf}(x) = \frac{2}{\sqrt{\pi}} \int_0^x e^{-t^2} dt. \quad (6)$$

The original Graesser and Cozzarelli model has a relatively simple expression with the parameters that can be easily acquired; however, this model excludes the martensitic hardening characteristics of SMAs under large amplitudes, which are critical for structural safety protection under extreme events.

To overcome the limitation of the original model, Wilde et al. [14] extended the Graesser and Cozzarelli model by dividing the full loop into four parts, adding two terms with six parameters into (1). The Wilde model was utilized to simulate the cyclic behaviors of SMA devices in other researches [21].

In the following, in order to accurately predict the cyclic behavior of a superelastic SMA device, especially capture the martensitic hardening characteristics of SMAs under large amplitudes, an improved Graesser and Cozzarelli model is presented. In the present model, the backstress expression is modified by adding a special term to capture the martensitic hardening characteristic of SMA under large amplitudes. The modified model is of the form

$$\dot{\sigma} = E \left[\dot{\varepsilon} - |\dot{\varepsilon}| \left(\frac{\sigma - \beta}{Y} \right)^{n-1} \left(\frac{\sigma - \beta}{Y} \right) \right], \quad (7)$$

$$\beta = E\alpha \{ \varepsilon_{in} + f_T |\varepsilon|^c \text{erf}(a\varepsilon) [u(-\varepsilon)] \}$$

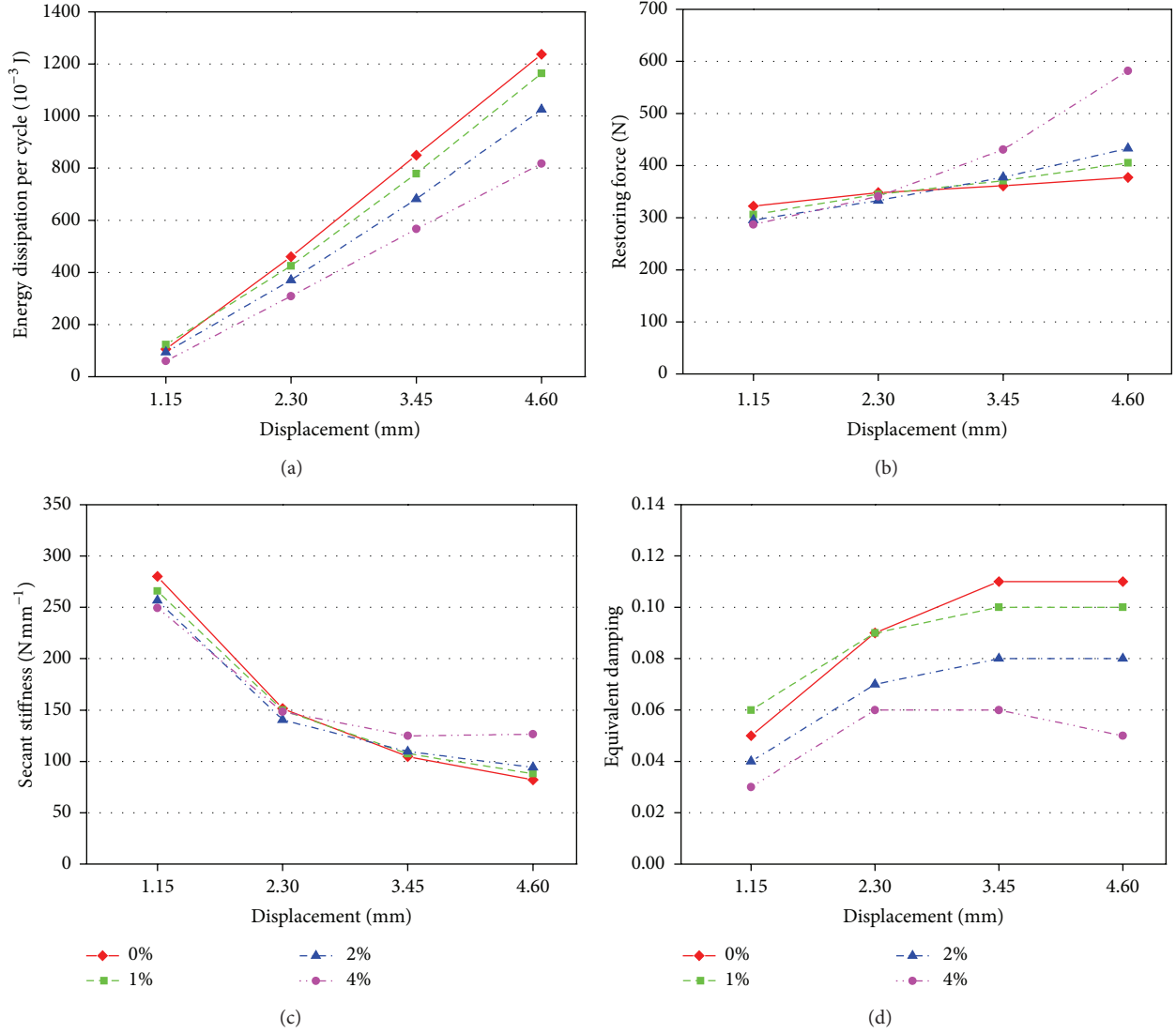


FIGURE 6: Mechanical properties of RSMAD as a function of prestrain and displacement amplitude (0.05 Hz frequency of loading, 20°C temperature).

$$\begin{aligned}
 &+ f_M [\varepsilon - \varepsilon_{Mf} \operatorname{sgn}(\varepsilon)]^m [u(\varepsilon \dot{\varepsilon})] \\
 &\times [u(|\varepsilon| - \varepsilon_{Mf})] \}.
 \end{aligned} \quad (8)$$

The third term in (2) is used to contribute to the back-stress on the ascending branch of the hysteresis in a way that allows for the martensitic hardening. ε_{Mf} is the martensite finish strain, f_M and m are material constants controlling the martensitic hardening curve. $\operatorname{sgn}(x)$ is the signum function, given by

$$\operatorname{sgn}(x) = \begin{cases} +1 & x > 0 \\ 0 & x = 0 \\ -1 & x < 0. \end{cases} \quad (9)$$

Figure 2 shows the stress-strain curves of superelastic nitinol wires predicted by the improved Graesser and Cozzarelli model versus experimental data at different strain

levels. The characteristic parameters used in the models are $E = 39500$ MPa, $Y = 385$ MPa, $\alpha = 0.01$, $f_T = 1.14$, $c = 0.001$, $a = 550$, $n = 3$, $\varepsilon_{Mf} = 0.05$, $f_M = 42500$, and $m = 3$. The superelastic nitinol wires are 0.5 mm in diameter, with a composition of approximately 50.9% Ni and 49.1% Ti. Under zero external stress, the martensite start and finish temperatures (M_s, M_f) and the austenite start and finish temperatures (A_s, A_f), measured by differential scanning calorimeter (DSC), are -73°C , -55°C , -23°C , and 5°C , respectively. The uniaxial tension test of the superelastic nitinol wires was carried out using an electromechanical universal testing machine at room temperature of 20°C . The nitinol wire samples, with a 100 mm test length between the two custom-made grips, were subjected to triangular cyclic loading under different strain amplitudes. The strains were calculated from the elongation measured by a 50 mm gage length extensometer with the stress calculated from the axial force, which was measured by a 10 kN load cell. Prior to

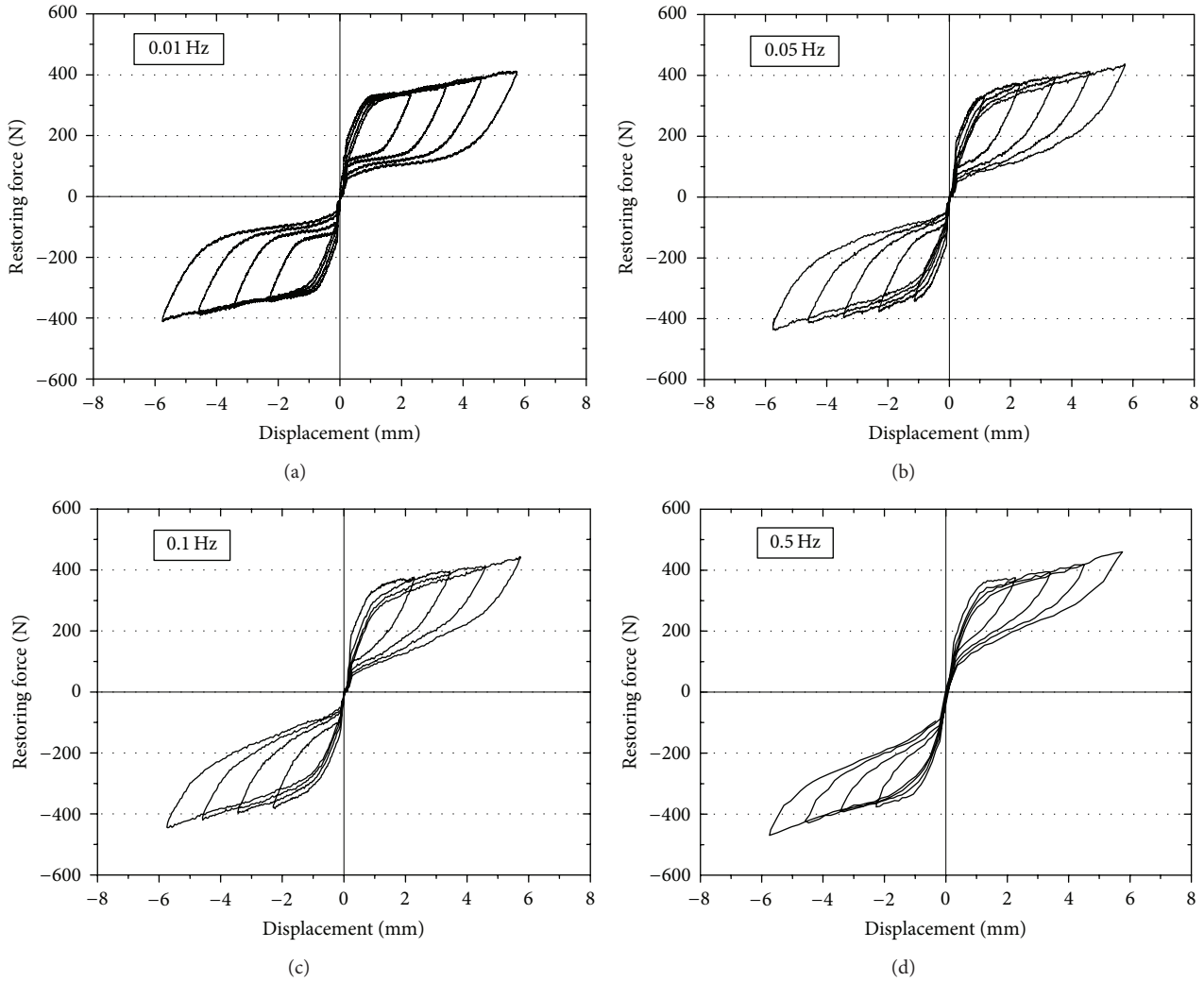


FIGURE 7: Hysteresis loops of the RSMAD at different loading frequencies and displacement amplitudes (0.6 mm predisplacement, 20°C temperature).

testing, the nitinol SMA specimens were cycled 20 times at 6% strain amplitude and $1.2 \times 10^{-3} \text{ s}^{-1}$ strain rate by a “training” process to reach a steady-state condition. The experimental data in Figure 2 are the results of cyclic tests on the superelastic nitinol wire at $1.2 \times 10^{-3} \text{ s}^{-1}$ strain rate with 1% to 8% strain levels. As shown in Figure 2, the hysteresis loops based on the improved Graesser and Cozzarelli model and experimental data match with close accuracy. Moreover, the improved model can accurately reflect the martensitic hardening characteristic of SMAs under large amplitudes.

3. An Innovative SMA Damper: Design, Experiment, and Numerical Simulation

3.1. Recentering SMA Damper Design. By utilizing the energy dissipating and recentering features of superelastic nitinol SMA, an innovative damper is designed. As shown in Figure 3, the damper consists of outer and inner cylinders, left and right pull plates, superelastic SMA wires, retaining plate,

prestrain adjusting plate, adjusting bolt, fixed bolt, push-pull rod, grip, end caps, and connecting fitting. In this damper, superelastic nitinol wires are the key components that provide both damping and self-centering abilities.

The damper will be connected to a structure via its push-pull rod and the connecting fitting. The prestrain of the superelastic wires can be adjusted by the prestrain adjusting plate and the adjusting bolt. The configuration of the damper shown in Figure 3 is in its equilibrium position. The specific design of the damper allows the push-pull rod to move in both left and right directions and return to its equilibrium position when the load is removed (self-centering). During this cyclic process, the damper provides damping, attributed to the hysteretic property of the superelastic wires.

3.2. Experimental Tests

3.2.1. Setup and Program. An SMA damper based on the design presented in Section 3.1 is fabricated. To assess the performance of the SMA damper, cyclic tests were carried

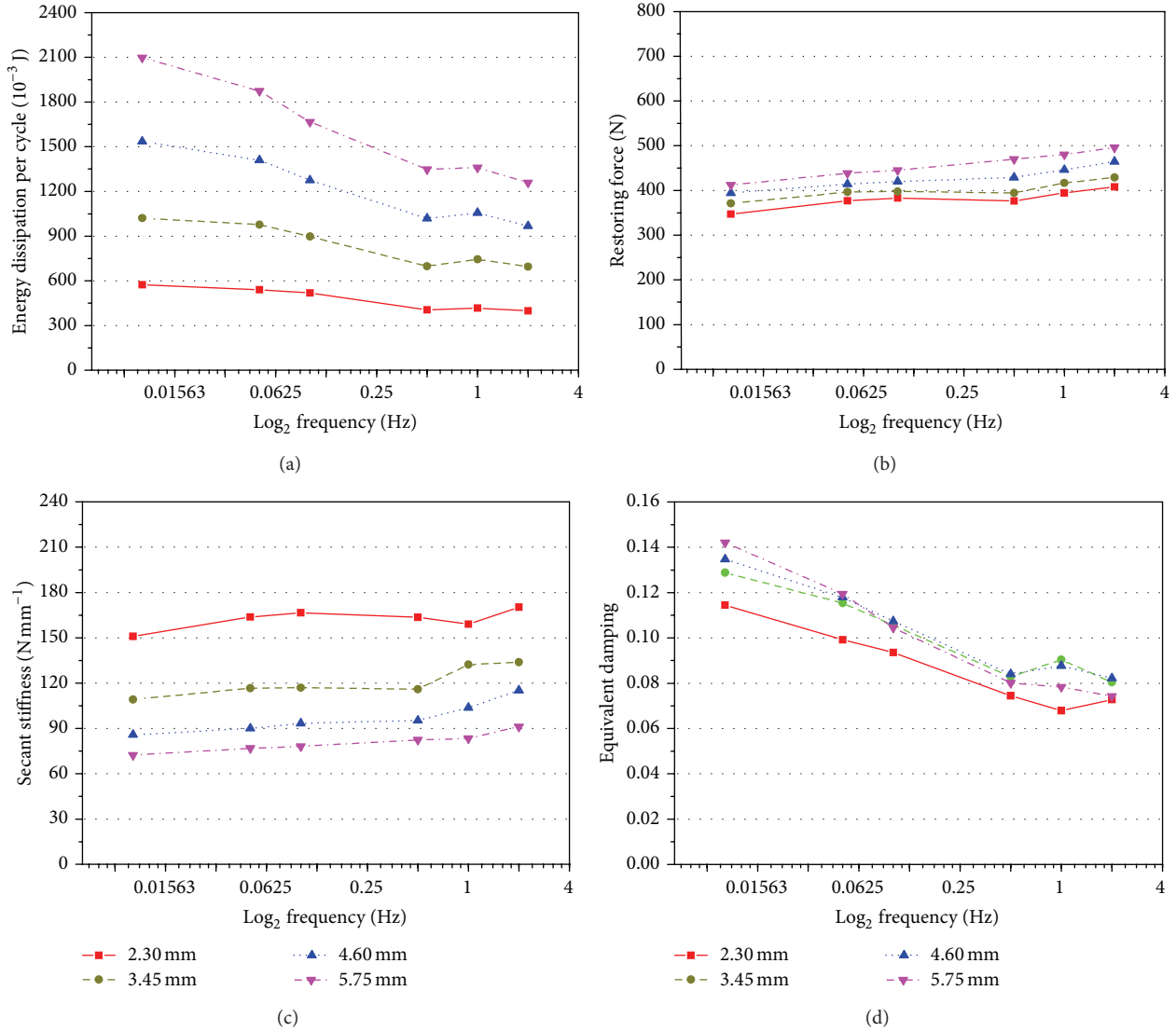


FIGURE 8: Mechanical properties of RSMAD as a function of loading frequencies and displacement amplitudes (0.6 mm predisplacement, 20°C temperature).

out. The SMA damper is 210 mm in length with a diameter of 100 mm and a stroke of ± 9.2 mm (the maximum allowable strain for superelastic nitinol wires is 8%). Four superelastic nitinol wires of a length of 115 mm and a diameter of 0.5 mm are used.

Tests were conducted using an MTS 810 machine with a 100 KN load cell at room temperature of 20°C. The layout of the test system is shown in Figure 4. The damper was tested with different prestrains, at different loading frequencies and at various amplitudes. During the tests, both force and displacement are recorded.

Prior to the installation, each nitinol wire was cycled 20 times at 6% strain with $1.2 \times 10^{-3} \text{ s}^{-1}$ strain rate to minimize the accumulation of residual strain and reach a steady-state condition. The scheme of the tests is described as follows.

- (1) Without prestrain, the damper was subjected to cyclic loading at 0.05 Hz frequency with displacement

amplitudes of 2.3 mm (2% of total length), 3.45 mm (3% of total length), and 4.6 mm (4% of total length), respectively.

- (2) Step (1) was repeated with prestrains of 1% (1.15 mm predisplacement), 2% (2.3 mm predisplacement), and 4% (4.6 mm predisplacement), respectively.
- (3) With 0.5% prestrain (about 0.6 mm predisplacement), the damper was subjected to cyclic loading at 0.01 Hz loading frequency with displacement amplitudes of 2.3 mm, 3.45 mm, 4.6 mm, and 5.75 mm, respectively.
- (4) Step (3) was repeated with loading frequencies of 0.05 Hz, 0.1 Hz, 0.5 Hz, 1 Hz, and 2 Hz, respectively.

To describe the performance of RSMAD as a function of prestrains, loading frequencies, and displacement amplitudes, some important mechanical properties were calculated, including the secant stiffness, K_s , the energy dissipation

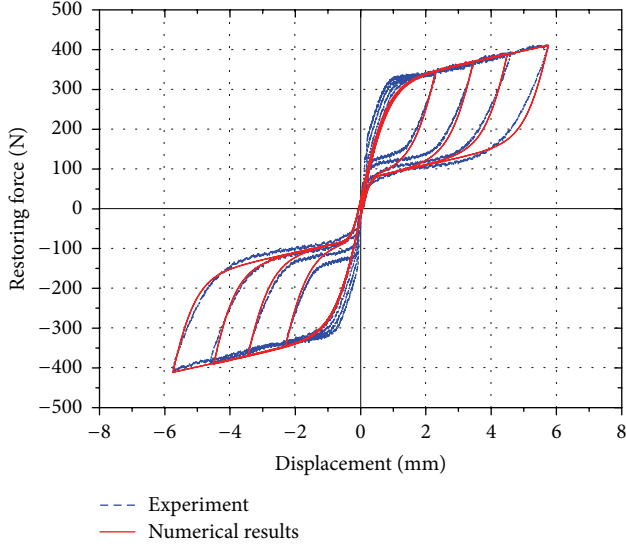


FIGURE 9: Comparison between experimental and numerical fitting curves of RSMAD.

per cycle, W_D , the restoring force at peak displacement per cycle, F_d , and the equivalent viscous damping ratio, ξ_{eq} , which is expressed as

$$\xi_{eq} = \frac{W_D}{2\pi K_s \delta^2}, \quad (10)$$

where δ is the displacement amplitude of the cycle.

3.2.2. Experimental Results. Figure 5 shows the hysteresis loops of RSMAD at different prestrains and displacement amplitudes. The tests were carried out at 0.05 Hz frequency of loading and room temperature of 20°C. As seen from Figure 5, the SMA damper shows double-flag hysteresis behavior without any residual strain.

Figure 6 shows the mechanical properties of RSMAD as a function of prestrain and displacement amplitude. As we can see in Figure 6, the greater the amplitude is, the greater the energy dissipation per cycle and restoring force are. However, the secant stiffness reduces markedly while increasing the amplitude. With the increasing of the predisplacement, the energy dissipation per cycle decreases, and restoring force and the secant stiffness increase at large displacement. The effectiveness of a damper is generally measured by the equivalent viscous damping ratio. With the increasing of the predisplacement, the equivalent damping ratio reduces. The most important finding is that when the predisplacement is less than 2.3 mm (2% prestrain), the equivalent damping ratio increased with the increasing of the amplitude; however, when the predisplacement is 4.6 mm (4% prestrain), the maximum of the equivalent damping ratio is at 2.3 mm (2% prestrain). This is because the maximum of the equivalent damping ratio of the NiTi SMA specimens is at about 6% total strain, as noted in [10].

Figure 7 shows the hysteresis loops of RSMAD with 0.6 mm predisplacement at different loading frequencies and displacement amplitudes at the temperature of 20°C. Figure 8

shows mechanical properties of RSMAD as a function of frequency of loading and displacement amplitude. As we can see in Figures 7 and 8, the energy dissipation per cycle and the equivalent damping decrease as the loading frequency increases in the range of 0.01–0.5 Hz but are not much sensitive to frequencies greater than 0.5 Hz. The restoring force and the secant stiffness increase slightly as the loading frequency increases in the total range of experimental frequency.

3.3. Numerical Simulation. Based on the improved Graesser and Cozzarelli model of SMA wire, a theoretic model of the SMA damper is developed. The differential equations of the model are given as

$$\begin{aligned} \dot{F} &= K_0 \left[\dot{x} - |\dot{x}| \left| \frac{F-B}{B_c} \right|^{(n-1)} \left(\frac{F-B}{B_c} \right) \right] \\ B &= K_0 \alpha \{ x_{in} + f_T |x|^c \operatorname{erf}(ax) [u(-x\dot{x})] \\ &\quad + f_M [x - x_{Mf} \operatorname{sgn}(x)]^m \\ &\quad \times [u(x\dot{x})] [u(|x| - x_{Mf})] \}, \end{aligned} \quad (11)$$

where F is restoring force; x is displacement; B is back-force; K_0 is initial stiffness; B_c , α , f_T , n , a , c , x_{Mf} , f_M , and m are constants controlling the size of the hysteresis loop; x_{in} is the inelastic displacement and $x_{in} = x - F/K_0$; $\operatorname{erf}(x)$, $u(x)$, and $\operatorname{sgn}(x)$ are, respectively, the error function, the step function, and the signum function, which have already been listed in Section 2.

Figure 9 shows the comparison of experimental results with numerical prediction based on the theoretical model at different displacement amplitudes. The parameters of the constitutive equation used in this study to simulate the behaviors of RSMAD are given as follows: $K_0 = 380$ N/mm, $B_c = 330$ N, $\alpha = 0.05$, $f_T = 21$, $c = 0.0001$, $a = 3$, $n = 2$, $x_{Mf} = 5.75$ mm, $f_M = 42500$, and $m = 3$. To accurately simulate the hysteresis behavior, the above parameters were directly obtained from the cyclic test results of the SMA damper according to the parameters' meanings and roles. The values also can be converted through the section area and the length of NiTi wires. However, there is slight difference between the two parameter groups. This is possible because of the effect of loading conditions on the cyclic behavior of NiTi wires. As can be seen in Figure 9, numerical predictions agree well with the experimental results.

Table 1 shows the comparison of the experimental data and numerical results, respectively, of the energy dissipation per cycle, the secant stiffness, and the equivalent viscous damping. As can be seen in Table 1, the maximum differences of energy dissipation per cycle, secant stiffness, and equivalent viscous damping are 5.0%, 1.2%, and 5.1%, respectively. These results indicate that the mechanical behavior of the SMA damper is well predicted by the numerical model, which verifies its suitability for the damper.

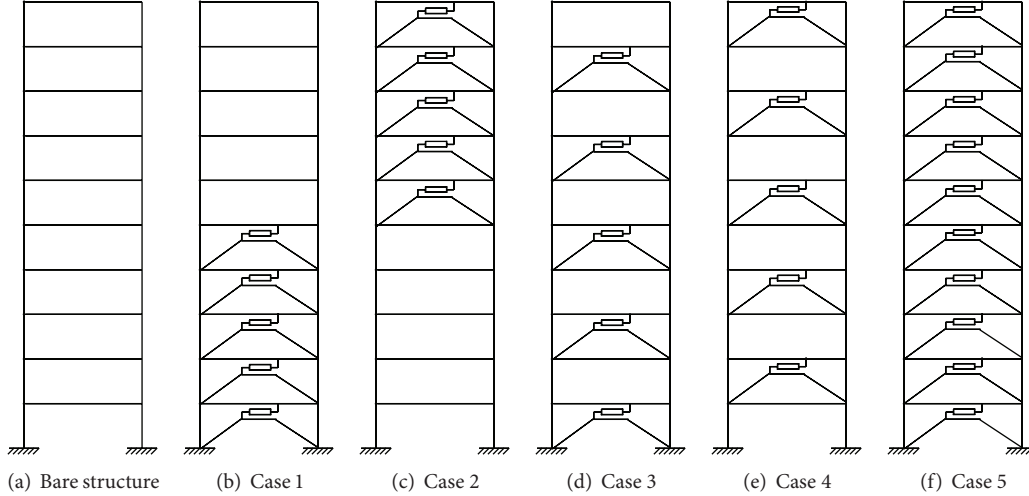


FIGURE 10: Different cases of the ten-story frame structure.

TABLE 1: Comparison between the experimental and theoretical results.

Peak displacement (mm)	Energy dissipation per cycle (N·mm)			Secant stiffness (N/mm)			Equivalent viscous damping (%)		
	Experimental data	Numerical results	Difference	Experimental data	Numerical results	Difference	Experimental data	Numerical results	Difference
2.3	573.90	545.00	5.0%	150.90	150.44	0.3%	11.40	10.90	4.4%
3.4	1021.10	1026.81	0.6%	109.17	108.27	0.8%	12.80	13.06	2.0%
4.6	1534.70	1586.28	3.4%	85.77	84.78	1.2%	13.40	14.08	5.1%
5.7	2097.80	2099.43	0.1%	72.37	71.92	0.6%	14.20	14.30	0.7%

TABLE 2: Parameters of the structure.

Story height h (m)	Story mass m (kg)	Story initial stiffness k_s (kN/mm)	Story yield shear Q_{sy} (kN)	Story yield displacement d_{sy} (mm)	Inelastic stiffness ratio γ	Damping ratio Z
4 m	64×10^3	40	400	10	0.01	2%

4. Model of Structure with SMA Dampers

The main objective of including energy dissipating devices in a structure is to reduce structural response through energy dissipation. To protect the original structural members under strong seismic loading, nonlinear deformation in energy dissipating devices will be allowed. In frame structures, the devices are usually incorporated in steel braces connecting two consecutive stories of the building. The dynamic response of the structure subjected to earthquake loading is governed by the following equation:

$$M_s \ddot{x}(t) + C_s \dot{x}(t) + F_s(x(t)) + F_d(x(t)) = -M_s I \ddot{x}_g(t), \quad (12)$$

where M_s is the mass matrix, C_s is the damping coefficient matrix, F_s is the vector of the frames restoring force, and F_d is the vector of restoring force resulting from SMA dampers. The x , \dot{x} , and \ddot{x} are the structural displacement, velocity, and acceleration vectors, respectively. On the right-hand side of

the equation, the vector I is the influence vector and the vector \ddot{x}_g is the ground motion acceleration input.

With the aid of the SIMULINK module of MATLAB, a dynamical simulation system was developed, in which the Wen model [36] is utilized to simulate the restoring force curve of the steel frame structure, and the improved Graesser and Cozzarelli model presented above is used for NiTi SMA damper.

5. Seismic Structural Control Using SMA Dampers

In this section, to assess the effectiveness of the proposed recentering SMA dampers (RSMAD) in mitigating the seismic response of building structure, nonlinear time history analysis on a multistory steel frame with and without the dampers subjected to representative earthquake ground motions was performed. The improved Graesser and Cozzarelli model for RSMAD given in Section 3.3 was employed in this numerical study. A ten-story steel moment resisting

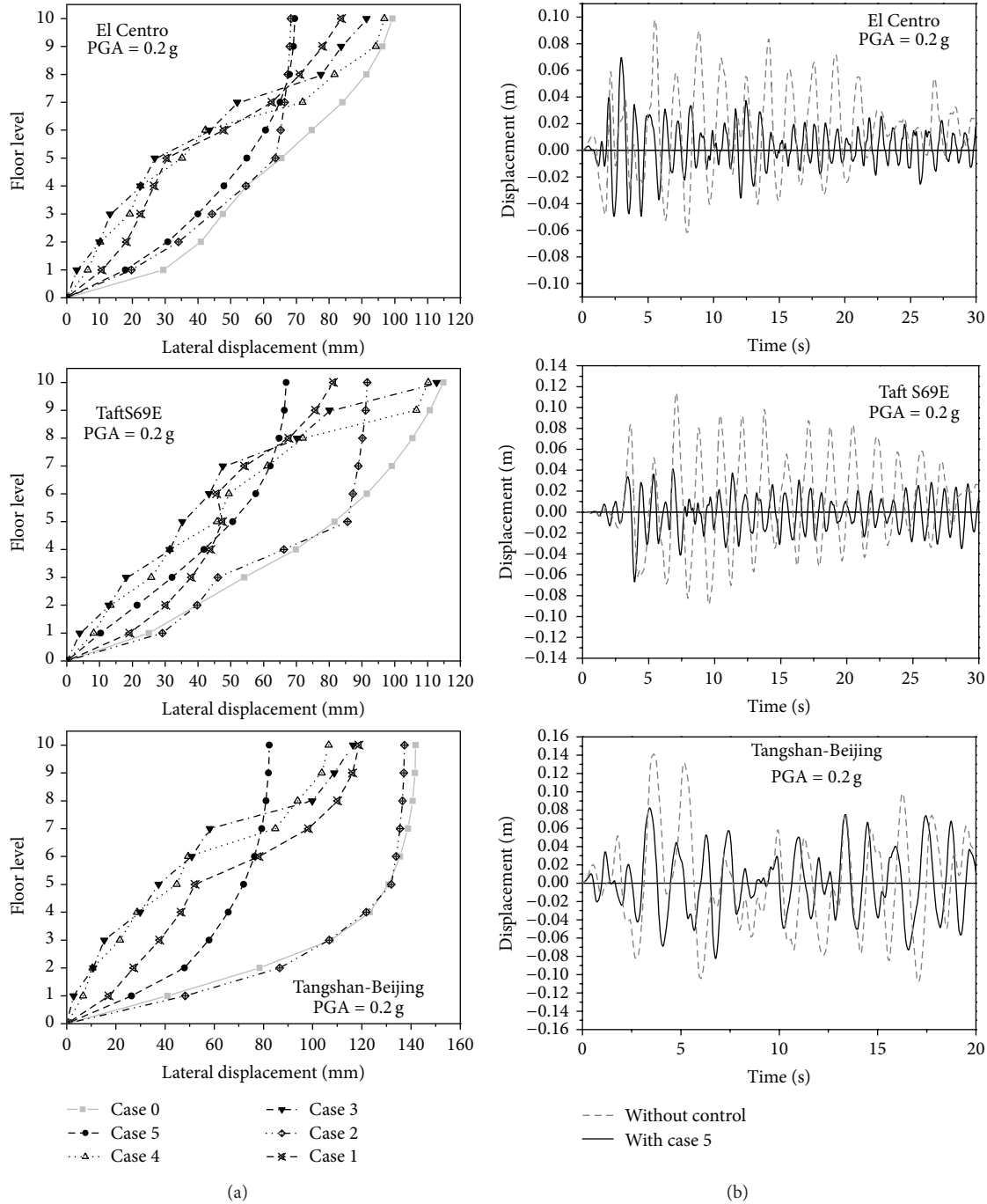


FIGURE 11: Lateral displacement envelopes (a) and roof displacement time histories (b) with and without SMA dampers under basic (moderate) ground motions.

frame structure was selected for this study. The building is designed for a location in Beijing, China. The parameters of the structure are listed in Table 2.

Three representative earthquake ground motions were used to considering the site effect. Three earthquake ground motions, namely, Imperial Valley 1940 El Centro, Lincoln School 1952 Taft, and Beijing Hotel 1976 Tangshan, were selected. These three ground motions represent different site conditions. According to Chinese code for seismic design

of building [37], the local seismic precautionary intensity is eight degrees. The peak ground accelerations (PGA) were adjusted to 0.2 g and 0.4 g corresponding to a seismic hazard level of 10% and 2% probability of exceedance in a 50-year period, respectively.

Simulation analysis is conducted on the bare structure and on the structure with five or ten SMA dampers installed as shown in Figure 10. Parameters of the SMA damper are listed as follows: $K_0 = K_d = 120 \text{ kN/mm}$, $B_c = 360 \text{ KN}$,

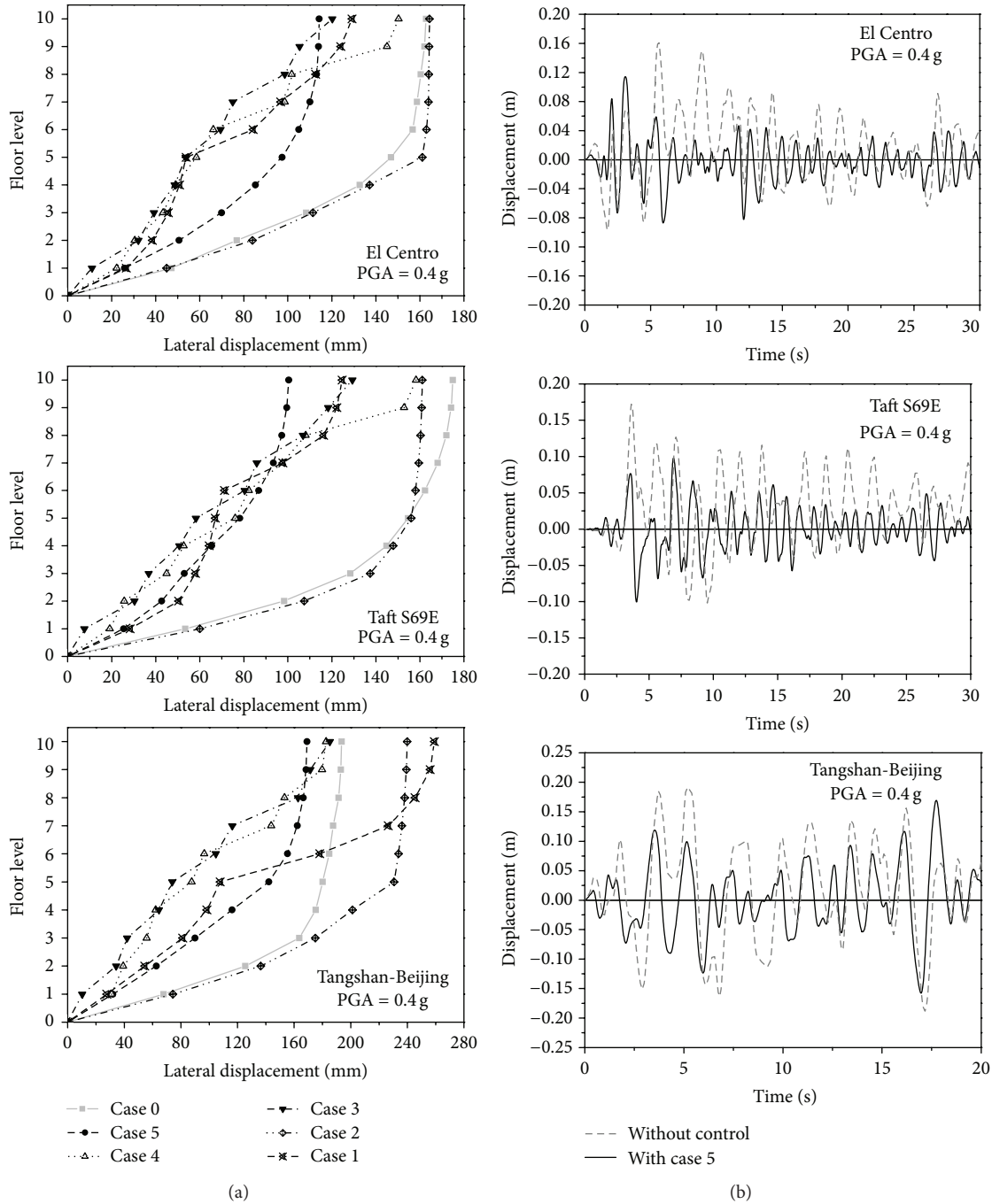


FIGURE 12: Lateral displacement envelopes (a) and roof displacement time histories (b) with and without SMA dampers under strong (severe) ground motions.

$\alpha = 0.010$, $f_T = 0.34$, $c = 0.0001$, $a = 2500$, $n = 5$, $x_{Mf} = 0.015$, $f_M = 100000$, and $m = 3$.

Figures 11 and 12 show the lateral displacement envelopes with and without SMA dampers under basic ground motions (0.2 g) and strong ground motions (0.4 g), respectively. As we can see, for most cases, the lateral displacement of the structure decreases remarkably with the introduction of the SMA dampers. However, the location and the number of the dampers have significant effects on the control results. Case 5, in which dampers are installed in all stories, is

the best for the overall structural vibration control. For other 4 configurations, in which five dampers are installed in different stores, cases 3 and 4 with dampers installed in alternate stories perform better than cases 1 and 2 with dampers placed in consecutive stories. Moreover, case 3 is better than case 4 since the first story is retrofitted. Case 1 is slightly worse due to the whiplash effect, and case 2 is the worst since the stiffness of the lower half is significantly greater than that of the upper half of the structure. The roof displacement time histories with (case 5) and without

SMA dampers under basic ground motions (0.2 g) and strong ground motions (0.4 g) are also, respectively, provided in Figures 11 and 12, which confirm that the SMA dampers significantly reduce the structural vibration.

6. Concluding Remarks

This paper presents the results of a study on evaluating the efficacy of using an innovative SMA-based damper to reduce the seismic response of structures. To describe the hysteresis behavior of the SMA damper, an improved Graesser and Cozzarelli model was proposed and verified by the cyclic tensile test on SMA wires.

Cyclic tests on the SMA damper model utilizing four superelastic SMA wires with 0.5 mm diameter with various prestrains under different loading frequencies and displacement amplitudes were carried out. The results show satisfying hysteresis properties, including both recentering and energy dissipating features under various conditions.

A comparative study on nonlinear time history analysis of the seismic response of a ten-story steel frame with the SMA dampers was performed. Five cases were considered for the location and the number of the dampers in the stories. The numerical analysis results indicate that the proposed SMA damper is capable of significantly reducing seismic response of structures, which verifies its effectiveness as energy dissipating device for structures. However, it is also indicated that the location and number have significant effects on the results of the response.

In future multiobjective optimization model will be proposed to obtain the number and the location of the SMA dampers and large scale shake table tests will be performed on a steel frame building with SMA dampers to prove the efficacy of these dampers in dissipating seismic energy.

Acknowledgments

This work was funded by National Science Foundation of China (no. 51108426 and no. 41104106), China Postdoctoral Science Foundation (no. 20100471008), and Research Fund for the Doctoral Program of Higher Education of China (no. 20104101120009). These supports are greatly appreciated. The opinions expressed in this study are those of the authors and do not necessarily reflect the views of the sponsor.

References

- [1] H. N. Li and L. S. Huo, "Advances in structural control in civil engineering in China," *Mathematical Problems in Engineering*, vol. 2010, Article ID 936081, 23 pages, 2010.
- [2] G. Song, N. Ma, and H. N. Li, "Applications of shape memory alloys in civil structures," *Engineering Structures*, vol. 28, no. 9, pp. 1266–1274, 2006.
- [3] SEAOC Vision 2000 Committee, *Performance-Based Seismic Engineering*, Structural Engineering Association of California, Sacramento, Calif, USA, 1995.
- [4] ATC-40, *Seismic Evaluation and Retrofit of Concrete Buildings*, Applied Technology Council, 1996.
- [5] FEMA 273, *NEHRP Guidelines for Seismic Rehabilitation of Buildings*, Federal Emergency Management Agency, 1997.
- [6] Y. Fujino, T. T. Soong, and B. F. Spencer Jr., "Structural control: basic concepts and applications," in *Proceedings of the ASCE Structures Congress*, pp. 15–18, Chicago, Ill, USA, April 1996.
- [7] B. F. Spencer and S. Nagarajaiah, "State of the art of structural control," *Journal of Structural Engineering*, vol. 129, no. 7, pp. 845–856, 2003.
- [8] T. T. Soong and G. F. Dargush, *Passive Energy Dissipation Systems in Structural Engineering*, John Wiley & Sons, New York, NY, USA, 1997.
- [9] F. M. Mazzolani, "Passive control technologies for seismic-resistant buildings in Europe," *Progress in Structural Engineering and Materials*, vol. 3, no. 3, pp. 277–287, 2001.
- [10] M. Dolce and D. Cardone, "Mechanical behaviour of SMA elements for seismic applications—part 2: austenite NiTi wires subjected to tension," *International Journal of Mechanical Sciences*, vol. 43, no. 11, pp. 2657–2677, 2001.
- [11] H. N. Li and X. X. Wu, "Limitations of height-to-width ratio for base-isolated buildings under earthquake," *The Structural Design of Tall and Special Buildings*, vol. 15, no. 3, pp. 277–287, 2006.
- [12] R. Desroches, J. McCormick, and M. A. Delemont, "Cyclic properties of superelastic shape memory alloy wires and bars," *Journal of Structural Engineering*, vol. 130, no. 1, pp. 38–46, 2004.
- [13] T. W. Duerig, K. N. Melton, D. Stockel, and C. M. Wayman, *Engineering Aspects of Shape Memory Alloys*, Butterworth Heinemann, London, UK, 1990.
- [14] K. Wilde, P. Gardoni, and Y. Fujino, "Base isolation system with shape memory alloy device for elevated highway bridges," *Engineering Structures*, vol. 22, no. 3, pp. 222–229, 2000.
- [15] M. Dolce, D. Cardone, and R. Marnetto, "Implementation and testing of passive control devices based on shape memory alloys," *Earthquake Engineering and Structural Dynamics*, vol. 29, no. 7, pp. 945–968, 2000.
- [16] M. Dolce, D. Cardone, F. C. Ponzo, and C. Valente, "Shaking table tests on reinforced concrete frames without and with passive control systems," *Earthquake Engineering and Structural Dynamics*, vol. 34, no. 14, pp. 1687–1717, 2005.
- [17] M. Indirli, M. G. Castellano, P. Clemente, and A. Martelli, "Demo-application of shape memory alloy devices: the rehabilitation of the S. Giorgio Church Bell-Tower," in *Smart Structures and Materials 2001: Smart Systems for Bridges, Structures, and Highways*, vol. 4330 of *Proceedings of SPIE*, pp. 262–272, Newport Beach, Calif, USA, March 2001.
- [18] B. Andrawes and R. Desroches, "Unseating prevention for multiple frame bridges using superelastic devices," *Smart Materials and Structures*, vol. 14, no. 3, pp. S60–S67, 2005.
- [19] R. DesRoches and M. Delemont, "Seismic retrofit of simply supported bridges using shape memory alloys," *Engineering Structures*, vol. 24, no. 3, pp. 325–332, 2002.
- [20] H. Li, M. Liu, and J. Ou, "Vibration mitigation of a stay cable with one shape memory alloy damper," *Structural Control and Health Monitoring*, vol. 11, no. 1, pp. 21–36, 2004.
- [21] Y. Zhang and S. Zhu, "A shape memory alloy-based reusable hysteretic damper for seismic hazard mitigation," *Smart Materials and Structures*, vol. 16, no. 5, pp. 1603–1613, 2007.
- [22] J. Ocel, R. DesRoches, R. T. Leon et al., "Steel beam-column connections using shape memory alloys," *Journal of Structural Engineering*, vol. 130, no. 5, pp. 732–740, 2004.

- [23] J. McCormick, R. Desroches, D. Fugazza, and F. Auricchio, "Seismic assessment of concentrically braced steel frames with shape memory alloy braces," *Journal of Structural Engineering*, vol. 133, no. 6, pp. 862–870, 2007.
- [24] Y. M. Parulekar, G. R. Reddy, K. K. Vaze et al., "Seismic response attenuation of structures using shape memory alloy dampers," *Structural Control and Health Monitoring*, vol. 19, no. 1, pp. 102–119, 2012.
- [25] K. Tanaka, "A thermomechanical sketch of shape memory effect: one-dimensional tensile behavior," *Res Mechanica*, vol. 18, no. 3, pp. 251–263, 1986.
- [26] C. Liang and C. A. Rogers, "One-dimensional thermomechanical constitutive relations for shape memory materials," *Journal of Intelligent Material Systems and Structures*, vol. 1, no. 2, pp. 207–234, 1990.
- [27] L. C. Brinson, "One-dimensional constitutive behavior of shape memory alloys: thermomechanical derivation with non-constant material functions and redefined martensite internal variable," *Journal of Intelligent Material Systems and Structures*, vol. 4, no. 2, pp. 229–242, 1993.
- [28] F. Falk, "Model free energy, mechanics, and thermodynamics of shape memory alloys," *Acta Metallurgica*, vol. 28, no. 12, pp. 1773–1780, 1980.
- [29] Q. P. Sun and K. C. Hwang, "Micromechanics modelling for the constitutive behavior of polycrystalline shape memory alloys—II: study of the individual phenomena," *Journal of the Mechanics and Physics of Solids*, vol. 41, no. 1, pp. 19–33, 1993.
- [30] J. G. Boyd and D. C. Lagoudas, "A thermodynamical constitutive model for shape memory materials—part I: the monolithic shape memory alloy," *International Journal of Plasticity*, vol. 12, no. 6, pp. 805–842, 1996.
- [31] Q. P. Sun and K. C. Hwang, "Micromechanics modelling for the constitutive behavior of polycrystalline shape memory alloys—I: derivation of general relations," *Journal of the Mechanics and Physics of Solids*, vol. 41, no. 1, pp. 1–17, 1993.
- [32] H. Qian, H. Li, G. Song, and W. Guo, "A constitutive model for superelastic shape memory alloys considering the influence of strain rate," *Mathematical Problems in Engineering*, vol. 2013, Article ID 248671, 8 pages, 2013.
- [33] W. J. Ren, H. N. Li, and G. Song, "A one-dimensional strain-rate dependent constitutive model for superelastic shape memory alloys," *Smart Materials and Structures*, vol. 16, no. 1, pp. 191–197, 2007.
- [34] E. J. Graesser and F. A. Cozzarelli, "Shape-memory alloys as new materials for aseismic isolation," *Journal of Engineering Mechanics*, vol. 117, no. 11, pp. 2590–2608, 1991.
- [35] H. Özdemir, *Nonlinear transient dynamic analysis of yielding structures [Ph.D. thesis]*, University of California, Berkeley, Calif, USA, 1976.
- [36] Y. K. Wen, "Method for random vibration of hysteretic systems," *Journal of the Engineering Mechanics Division*, vol. 102, no. 2, pp. 249–263, 1976.
- [37] GB, 50011-2010, *Code for Seismic Design of Buildings*, Ministry of Housing and Urban-Rural Development of the People's Republic of China, 2010.

Research Article

A Static Control Algorithm for Adaptive Beam String Structures Based on Minimal Displacement

Yanbin Shen, Huaqiang Cheng, Pengcheng Yang, and Yaozhi Luo

College of Civil Engineering and Architecture, Zhejiang University, Hangzhou 310058, China

Correspondence should be addressed to Yaozhi Luo; mstcad@163.com

Received 1 August 2013; Revised 6 October 2013; Accepted 15 October 2013

Academic Editor: Hong-Nan Li

Copyright © 2013 Yanbin Shen et al. This is an open access article distributed under the Creative Commons Attribution License, which permits unrestricted use, distribution, and reproduction in any medium, provided the original work is properly cited.

The beam string structure (BSS) is a type of prestressed structure and has been widely used in large span structures nowadays. The adaptive BSS is a typical smart structure that can optimize the working status itself by controlling the length of active struts via certain control device. The control device commonly consists of actuators in all struts and sensors on the beam. The key point of the control process is to determine the length adjustment values of actuators according to the data obtained by preinstalled sensors. In this paper, a static control algorithm for adaptive BSS has been presented for the adjustment solution. To begin with, an optimization model of adaptive BSS with multiple active struts is established, which uses a sensitivity analysis method. Next, a linear displacement control process is presented, and the adjustment values of struts are calculated by a simulated annealing algorithm. A nonlinear iteration procedure is used afterwards to calibrate the results of linear calculation. Finally, an example of adaptive BSS under different external loads is carried out to verify the feasibility and accuracy of the algorithm. And the results also show that the adaptive BSS has much better adaptivity and capability than the noncontrolled BSS.

1. Introduction

The beam string structure (BSS) is a type of prestressed system initially presented by Saitoh in the early 1980s [1, 2]. It has good mechanical behavior and now has been widely used in large span structures such as airport, exhibition hall, and gym. Three most typical cases that are frequently cited in China are Shanghai Pudong International Airport Terminal, Guangzhou International Convention and Exhibition Center, and the Main Stadium of Harbin International Convention and Exhibition Center. Their span reaches 82.6 m, 126.6 m, and 128.5 m, respectively. The BSS commonly consists of three parts, namely, the upper beam (or a truss), the lower cable, and the vertical link strut, as shown in Figure 1. The prestress in the cable balances the horizontal thrust on the support and decreases the bending moment value on the upper beam, which greatly improves the structural stiffness and capability of the BSS. Despite its relatively light internal force, the vertical link strut still plays an important role in the entire system. Tiny changes on the length of struts will cause wide force redistribution in the entire BSS. Therefore, if the vertical link strut is converted into a kind of adjustable component,

the traditional BSS would become a new kind of smart structure with self-adjustment ability and better mechanical behavior.

In recent years, smart structures have become a hot spot of research, which represents the future direction of structure development. A smart civil structure is a civil structure (e.g., buildings, bridges, dams, etc.) that can monitor and react to environmental conditions and the structure's own conditions, in a predesigned and beneficial manner [3]. Currently, in civil engineering, most research works on smart structures focus on vibration control and have made tremendous achievement. Various types of techniques and devices such as magnetorheological (MR) damper, shape memory alloy (SMA) actuator, hybrid active mass damper (AMD), and piezoceramic actuator, concentrically braced frames (CBF) are applied to vibration control [4–12]. Meanwhile, a few studies have paid attention to the smart structure based on the control of static characteristics such as deformation and internal force. Some typical cases involve the applications of smart prestress, smart strut, and smart beam [13, 14].

This paper illustrates a typical kind of smart structure based on static characteristics control, namely, the adaptive

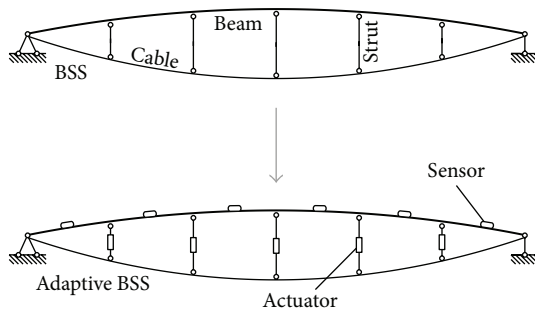


FIGURE 1: Diagram of an adaptive BSS.

BSS. The adaptive BSS can optimize the working status itself by controlling the length of one or several adjustable link struts according to the changes of external loads, as shown in Figure 1. The control device commonly consists of actuators in each strut and sensors on the beam. Following a typical smart structure style, the working principle is as follows. Due to the excitation of external loads, the static characteristics of the structure have made changes. The sensors placed on the structure monitor that change and transfer data to the controller. Via analysis and calculation, an adjustment strategy is generated by the controller and sent to actuators. The actuators then execute the adjustment strategy, and a complete control process ends. The key point of the control process is to determine the length adjustment values of actuators according to the displacement values obtained by sensors.

The adaptive BSS is a novel smart structure, so there are rarely systemic research works to be referenced. Some similar researches on smart beams have been reported, but those beams cannot be considered as a true BSS system and usually contain one or two struts. Basically, the static control of those kinds of smart beams includes internal force control and displacement control. Noack et al. studied the control strategy of a smart beam with one active strut under moving loads, taking the displacement as the control objective [13]. Sobek and Teuffel carried on similar work and updated the system to beams with two active struts [14]. For the smart beam with one or two active struts, heuristic selection and exhaustive method could meet the requirement of static control analysis, while for a typical adaptive BSS with a set of struts, the entire search space becomes too large and the brute methods can no longer satisfy the requirement. For large solution spaces searching problems, stochastic search techniques such as genetic algorithm (GA) and simulated annealing (SA) algorithm are usually applied. On the other hand, all works mentioned above assume that the smart prestressed system works in linearity; therefore, the linear static control method is employed. However, the BSS system usually contains a set of struts and cables which make the structure flexible to a certain degree. For a flexible structure with large displacement behavior, nonlinear method is commonly incorporated into control algorithm for better accuracy. Similar nonlinear static control method had been used in cable-strut structures in the past [15]. Although the static control optimization model for cable-strut structures is not suitable for the adaptive BSS,

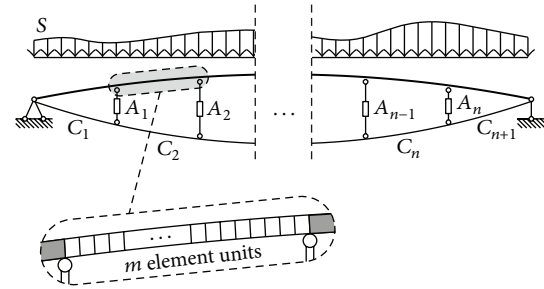


FIGURE 2: Model of an adaptive BSS.

its nonlinear static control method could still be a good reference.

In this paper, a static control algorithm for adaptive BSS has been presented for the adjustment solution. It is based on nonlinear finite element method and SA algorithm. The paper is organized as follows. Section 2 establishes an optimization model of adaptive BSS with multiple active struts, and a sensitivity analysis method is applied. Section 3 presents a linear displacement control process mainly by means of an SA algorithm and then proposes a nonlinear iteration to calibrate the result of the linear calculation. Section 4 carries out an example of a three-strut adaptive BSS under different external loads and conducts the comparisons between results from noncontrolled BSS and adaptive BSS. Finally, a summary of the research work is given in Section 5.

2. The Static Control Model Based on Minimal Displacement

The mechanical model of adaptive BSS with multiple active struts is established for static control analysis at first, and a sensitivity analysis method is used to evaluate the influence of each of the multiple adjustable struts. The sensitivity analysis method was proposed early in 1980s by Sobieszczanski-Sobieski et al. to study the sensitivity of optimum solution of problem parameters. The basic principle of sensitivity analysis is to get the derivative of the optimum solution to multiple variables and then obtain the optimum solution and the corresponding variables via calculating the weight factors of different variables [16]. Besides, a working status factor of the BSS system based on displacement is defined as the control objective.

2.1. Mechanical Modeling of Adaptive BSS. The simplified mechanical model of a typical adaptive BSS with multiple active struts is shown in Figure 2. The upper beam is subdivided into plenty of small beam element units for more accuracy. Each active strut is considered as a single link element, and the cable segment between two joints is treated as a single cable element unit. Some assumptions are given when performing static control analysis: (1) the material nonlinearity of the adaptive BSS is not considered; (2) the fixed hinge bearing is on the left end of the beam and the sliding hinge bearing is on the right; (3) the weight of the structure is converted into equivalent dead loads, and all external loads

are applied on the beam only; and (4) the joint connecting the cable and the strut is a hinge, and the cable between two joints is considered as a straight line with tension only, ignoring the effect of the cable sag.

The BSS is assumed to adopt linear behavior, and according to superposition principle, the internal force and displacement value of the structure after adjustment are

$$\begin{aligned}\mathbf{F}_C &= \mathbf{F}_0 + \Delta\mathbf{F}, \\ \mathbf{d}_C &= \mathbf{d}_0 + \Delta\mathbf{d},\end{aligned}\quad (1)$$

where \mathbf{F}_0 and \mathbf{d}_0 represent the internal force and displacement value of the structure before adjustment, respectively. After an arbitrary adjustment, the structure has new internal force of \mathbf{F}_C and displacement of \mathbf{d}_C . $\Delta\mathbf{F}$ and $\Delta\mathbf{d}$ are the increments of the internal force and displacement, respectively, which are given by

$$\begin{aligned}\Delta\mathbf{F} &= \mathbf{S}_{A,F}\mathbf{e}_A, \\ \Delta\mathbf{d} &= \mathbf{S}_{A,D}\mathbf{e}_A,\end{aligned}\quad (2)$$

where $\mathbf{S}_{A,F}$ and $\mathbf{S}_{A,D}$ are the sensitivity matrix of internal force and displacement, respectively. \mathbf{e}_A denotes the length adjustment values of active struts. For a specific BSS with elements amounted to N_e , nodes amounted to N_n , and adjustable struts amounted to N_a , (2) can be expressed as

$$\begin{bmatrix} \Delta\mathbf{F}_1 \\ \Delta\mathbf{F}_2 \\ \dots \\ \Delta\mathbf{F}_{N_e} \end{bmatrix} = \begin{bmatrix} \Delta\mathbf{F}_1^1 & \Delta\mathbf{F}_1^2 & \dots & \Delta\mathbf{F}_1^{N_a} \\ \Delta\mathbf{F}_2^1 & \Delta\mathbf{F}_2^2 & \dots & \Delta\mathbf{F}_2^{N_a} \\ \dots & \dots & \Delta\mathbf{F}_i^j & \dots \\ \Delta\mathbf{F}_{N_e}^1 & \Delta\mathbf{F}_{N_e}^2 & \dots & \Delta\mathbf{F}_{N_e}^{N_a} \end{bmatrix} \begin{bmatrix} e_{A1} \\ e_{A2} \\ \dots \\ e_{AN_a} \end{bmatrix}, \quad (3)$$

$$\begin{bmatrix} \Delta\mathbf{d}_1 \\ \Delta\mathbf{d}_2 \\ \dots \\ \Delta\mathbf{d}_{N_n} \end{bmatrix} = \begin{bmatrix} \Delta\mathbf{d}_1^1 & \Delta\mathbf{d}_1^2 & \dots & \Delta\mathbf{d}_1^{N_a} \\ \Delta\mathbf{d}_2^1 & \Delta\mathbf{d}_2^2 & \dots & \Delta\mathbf{d}_2^{N_a} \\ \dots & \dots & \Delta\mathbf{d}_i^j & \dots \\ \Delta\mathbf{d}_{N_n}^1 & \Delta\mathbf{d}_{N_n}^2 & \dots & \Delta\mathbf{d}_{N_n}^{N_a} \end{bmatrix} \begin{bmatrix} e_{A1} \\ e_{A2} \\ \dots \\ e_{AN_a} \end{bmatrix}, \quad (4)$$

where $\Delta\mathbf{d}_i^j$ denotes the displacement increment of node j when the adjustable strut i changes a unit value, and it is described as $[\Delta\mathbf{d}_i^{j,x}, \Delta\mathbf{d}_i^{j,y}, \Delta\mathbf{d}_i^{j,z}]^T$. $\Delta\mathbf{F}_i^j$ indicates the internal force increment of element j when the adjustable strut i changes a unit value, and it is described as $[\Delta N_i^{j,L}, \Delta S_i^{j,L}, \Delta M_i^{j,L}, \Delta N_i^{j,R}, \Delta S_i^{j,R}, \Delta M_i^{j,R}]^T$ for beam element and $[\Delta N_i^{j,L}, \Delta N_i^{j,R}]^T$ for cable and link elements.

2.2. The Minimal Displacement Control Objective. The BSS is a self-balancing system with a set of link struts connecting the beam and the cable. The beam withstands external loads directly and bears bending moment and pressure. The prestress applied in the cable largely decreases the maximum

values of internal force and displacement of the beam. Technically, the function of the prestressed cable and link struts is to improve the capability of the beam, and the mechanical behavior of the beam reflects the performance of the entire BSS system. In this paper, a displacement state factor f_{Dj} of the beam is specified with (5) to identify the performance of the system:

$$f_{Dj} = \begin{cases} \frac{d_{Bj}}{d_B^U}, & d_{Bj} \geq 0, \\ \frac{d_{Bj}}{d_B^L}, & d_{Bj} < 0, \end{cases} \quad (5)$$

in which d_B^U and d_B^L refer to the upper bound and lower bound of the adjustable displacement range of node j on the beam, respectively. Normally the length of 1/250 span of the structure is considered as the allowable value according to design code. d_{Bj} is the displacement value of node j .

A working status factor β_D of the BSS system based on displacement is given by

$$\beta_D = \max(f_{Dj}), \quad j = 1, 2, \dots, n+1, \quad (6)$$

where n is the amount of subdivisions of the beam.

The optimum design for a traditional BSS is to search the structural shape, component cross-section size, and cable prestress to satisfy the requirement of $\beta_D \leq 1$ under the most unfavorable load. For an adaptive BSS, the basic principle of displacement control is to improve the internal force distribution and decrease the maximal value of displacement via adjusting the length of the active struts. When β_D reaches the minimum, the working status of the BSS is probably the best.

In addition, during the control process, some other conditions such as the structural material strength and the adjustment range of the active struts should be satisfied at the same time. All constraint conditions are detailed as

$$d_B^L \leq d_{Bj} \leq d_B^U, \quad (7)$$

$$\sigma_B^C \leq \sigma_{Bj} \leq \sigma_B^T, \quad (8)$$

$$\sigma_A^C \leq \sigma_{Aj} \leq 0, \quad (9)$$

$$N_C^L \leq N_{Cj} \leq N_C^T, \quad (10)$$

$$e_A^L \leq e_{Aj} \leq e_A^U, \quad (11)$$

where σ_B^C and σ_B^T are the allowable compressive and tensional stress values of the beam, respectively. σ_A^C is the allowable compressive stress value of the active strut. N_C^T denotes the allowable tensional force value of cables, and N_C^L is the lower bound of tensional force range that usually equals 5% of N_C^T . e_A^L and e_A^U stand for the lower bound and upper bound of the adjustment length range of the active strut. d_{Bj} , σ_{Bj} , σ_{Aj} , N_{Cj} , and e_{Aj} denote the displacement value of node j of the beam, the stress value of element unit j of the beam, the stress value of active struts j , the tensional force of cable j , and the length

adjustment value of active strut j , respectively. Detailed stress expressions of different structural components are specified as

$$\sigma_{Bj} = \frac{N_{Bj,L}}{A_{Bj}} \pm \max \left(\left| \frac{M_{Bj,L}}{W_{Bj}} \right|, \left| \frac{M_{Bj,R}}{W_{Bj}} \right| \right), \quad (12)$$

$$\sigma_{Aj} = \frac{N_{Aj,L}}{A_{Aj}},$$

where $N_{Bj,L}$, $M_{Bj,L}$, and $M_{Bj,R}$ are the axial force, moment on left end and moment on right end of the unit j of the beam, respectively. A_{Bj} and W_{Bj} are the cross-section area and inertia modulus of the unit j of the beam, respectively. $N_{Aj,L}$ and A_{Aj} are the axial force and cross-section area of the active strut j .

In summary, the static control analysis based on minimal displacement to adaptive BSS is treated as an optimization problem, with β_D as the cost function and (7) to (11) as constraints, which is indicated in

$$\begin{aligned} & \text{solve } e_A \\ & \text{make } \beta_D(e_A) \longrightarrow \min \\ & \text{s.t. } (7) \text{ to } (11). \end{aligned} \quad (13)$$

3. The Static Control Algorithm

3.1. Linear Displacement Control Process Using SA. Linear displacement control (LDC) is a basis of nonlinear displacement control (NDC). In this paper, SA algorithm is employed to search an optimal adjustment solution. It is a stochastic search method that has been successfully applied to a variety of problems in optimization research. In its application to this paper, the entire calculation process starts with randomly generating a set of e_A that satisfy (11) and evaluating the working status factor β_D and all static results of this selection. And then a new selection of e_A is generated by a random alteration within a neighborhood of last selection. The β_D of the new selection is calculated and compared with the minimum β_D of all the previous selections. If the current β_D is lower than the minimum β_D , the new selection takes over directly. Otherwise, a Metropolis algorithm is used to determine whether the new selection of e_A is accepted or not. And for every Mapkobl length of repetitions of the above procedure, a cooling operation is performed once. It will not stop until the optimized value to the minimum β_D is lower than the given criterion ε or the system is cooled over. The flowchart of the entire process described above is summarized in Figure 3.

3.2. Nonlinear Displacement Control Procedures. The linear displacement control algorithm presented in the previous section is no longer suitable when considering the structural nonlinearity of the BSS system. Referring to the nonlinear finite element method and based on the LDC algorithm, the NDC algorithm is established via applying an iterative procedure analogous to the Newton-Raphson method, as shown in Figure 4. Firstly, an approximate solution has been obtained by using the LDC algorithm, as shown by AB in Figure 4.

And then the structural response from the linear solution is revised to its real state C by nonlinear finite element method (NFEM). The above process can be repeated at any new state (e.g., C) until the structure converges to the target state.

For NDC algorithm, (1) is no longer valid and should be replaced by the iterative equations as

$$\begin{aligned} \mathbf{F}_C^{(k)} &= \mathbf{F}_C^{(k-1)} + \delta \mathbf{F}^{(k)}, \\ \mathbf{d}_C^{(k)} &= \mathbf{d}_0^{(k-1)} + \delta \mathbf{d}^{(k)}, \end{aligned} \quad (14)$$

where $\mathbf{F}_C^{(k)}$ and $\mathbf{d}_C^{(k)}$ are the estimated solution of the internal force and displacement on k step, respectively. $\mathbf{F}_C^{(k-1)}$ and $\mathbf{d}_C^{(k-1)}$ are the real state of the internal force and displacement on $k-1$ step. $\delta \mathbf{F}^{(k)}$ and $\delta \mathbf{d}^{(k)}$ are calculated according to $\delta e^{(k)}$ which is generated by LDC with $\beta_{D,\min}^{(k)}$ as the target. Accordingly, at each iteration step, the deviation of the working status factor from the real state is defined as

$$\beta_D'^{(k)} = \beta_{D,\min}^{(k)} - \beta_D^{(k)}, \quad (15)$$

where $\beta_D'^{(k)}$ means the deviation of the working status factor on k step, $\beta_{D,\min}^{(k)}$ is the minimal working status factor generated by LDC on k step, and $\beta_D^{(k)}$ denotes the working status factor of real state after revision by NFEM. Accordingly, the deviation of the internal force and displacement from the real state can also be expressed by $F_C'^{(k)}$ and $d_C'^{(k)}$, respectively. By introducing a Newton-Raphson iterative procedure to (14), they can converge to the optimal state of the structure finally.

The flowchart of the solution searching process of NDC algorithm is shown in Figure 5. A Matlab program has been written to implement the algorithm and has been used for the example in the next section.

4. Example

As shown in Figure 6, a three-strut adaptive BSS with a span of 48 meters and an inverted rise of 6 meters is considered as an example for the control algorithm verification. The straight beam (thick line) employs a square cross section steel tube, and the size of the cross section is 300 mm in width, 400 mm in height, and 20 mm in wall thickness. The beam is subdivided into 120 small beam element units for more accurate calculation. The three active link struts (middle thick line) are circular pipes with a diameter of 140 mm and a wall thickness of 6 mm. The cable (light line) consists of 61 steel wires with a diameter of 5 mm, and the prestress in the cable is produced by the dead load. In calculation, all constraint conditions are detailed as shown in Table 1. The elasticity modulus of the beam and struts is $2.06 \times 10^5 \text{ N/mm}^2$, and that of the cable is $1.95 \times 10^5 \text{ N/mm}^2$.

For a roof structure, there are usually four types of external loads being considered, namely, the dead load, the full span live load, the half span live load, and the upward wind load. They are notated as S_G , S_{Q1} , S_{Q2} , and S_W , respectively. Assume that all loads are applied on the beam, and $S_G = 5 \text{ kN/m}$. Three typical load cases are calculated for the next

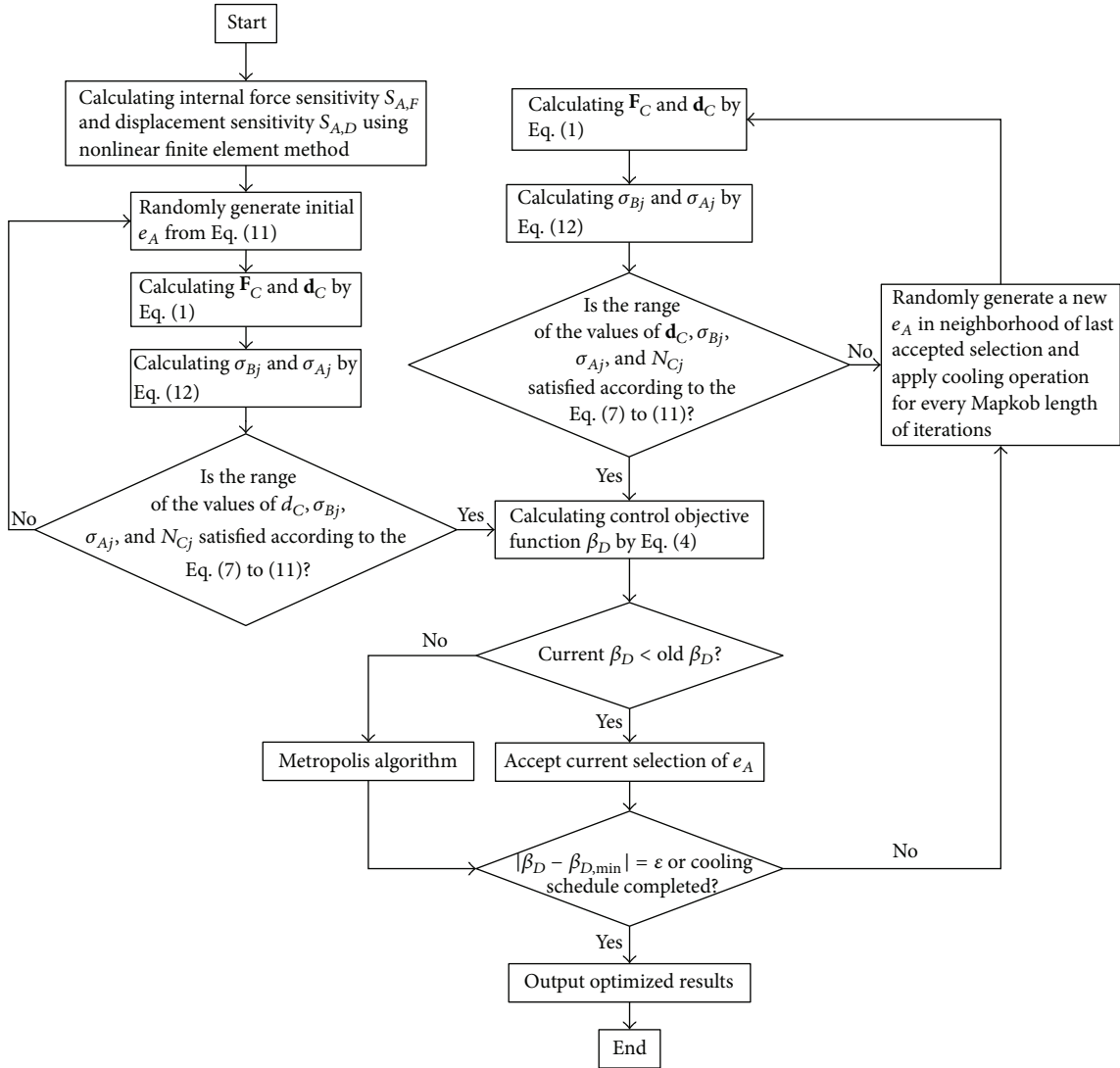


FIGURE 3: SA process for LDC solution.

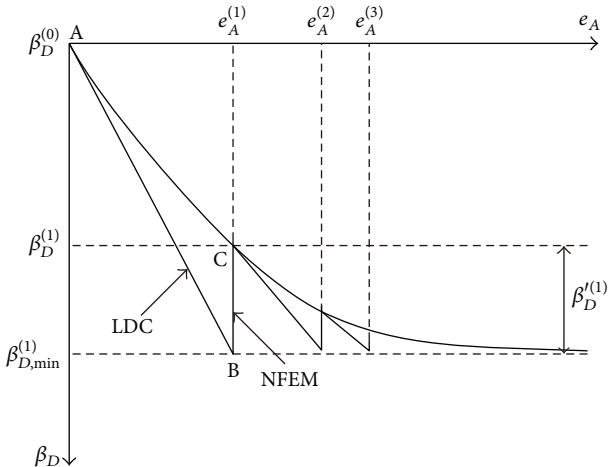


FIGURE 4: Illustration of iterations in searching for solution of NDC.

discussion. Load Case 1, $S_G + S_{Q1}$, is the most unfavorable downward load case with uniform distribution. Load Case 2, $S_G + S_{Q2}$, is the most unfavorable downward load case with unsymmetrical distribution. Load Case 3, $S_G + S_W$, is the most unfavorable upward load case with uniform distribution. In this section, the ultimate loads of S_{Q1} , S_{Q2} , and S_W under the three load cases above are calculated in the case of noncontrolled and controlled structure, respectively. And all the static state results of noncontrol, LDC, and NDC are discussed in details to validate the algorithm and prove the capability of the adaptive system.

4.1. Load Case 1: $S_G + S_{Q1}$. The ultimate load of S_{Q1} for noncontrolled BSS is calculated as $S_{Q1} = 5.2 \text{ kN/m}$, which is subject to all constraint conditions in Table 1. With the value of S_{Q1} obtained, calculation under load Case 1, $S_G (5 \text{ kN/m}) + S_{Q1} (5.2 \text{ kN/m})$, for noncontrol, LDC, and NDC is then

TABLE 1: Constraint conditions for calculation.

Allowable displacement of the beam (mm)		Allowable stress of struts (N/mm ²)	Allowable adjustment of struts (mm)		Allowable tension of cables (kN)		Allowable stress of the beam (N/mm ²)	
d_B^L	d_B^U	σ_A^C	e_A^L	e_A^U	N_C^L	N_C^T	σ_B^C	σ_B^T
-192	192	-215	-400	400	98	1880	-215	215

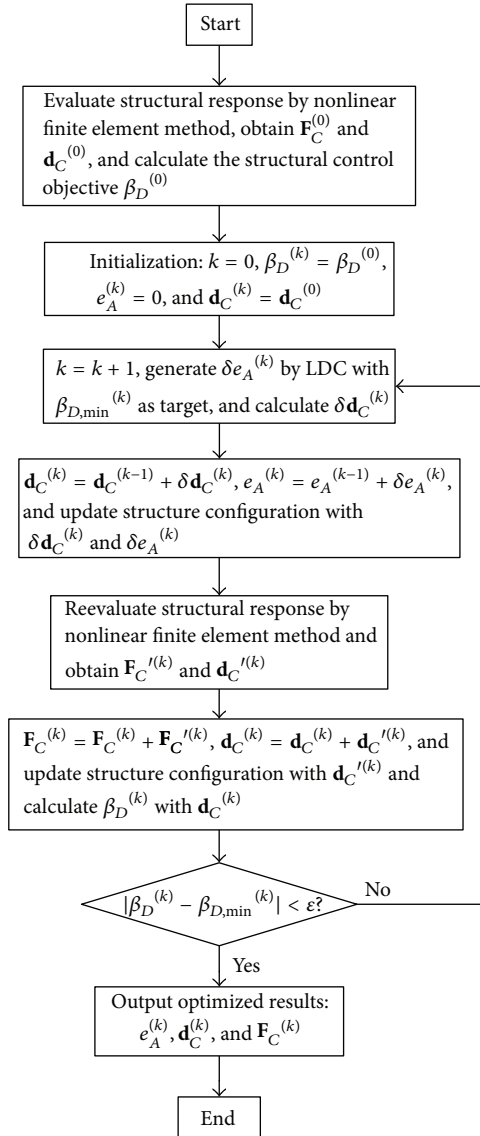


FIGURE 5: Procedures of solution searching for NDC.

followed, and all the static state results are shown in Table 2. It turns out that the ultimate load of S_{Q1} is literally subject to the allowable displacement of the beam; that is, β_D is close to 1. And the adjustment effect of NDC is slightly better than LDC according to β_D .

For the main bearing component, namely, the beam, the displacement and moment state directly reflect its working state, as shown in Figures 7 and 8, where the abscissa axis represents the location on the beam. After control, the displacement state improvement is obvious to see and the

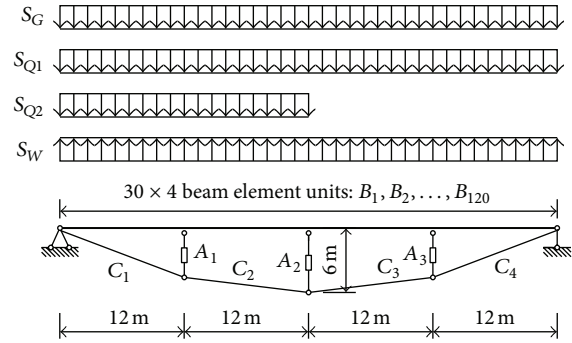


FIGURE 6: A three-strut adaptive BSS.

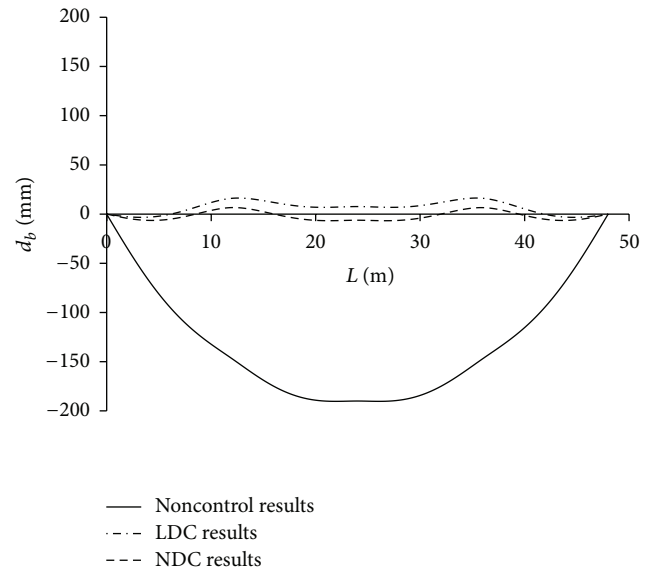


FIGURE 7: Displacement state of the beam under load Case 1.

moment values become well distributed around the abscissa axis.

For further comparison, the ultimate load of S_{Q1} for the adaptive BSS is calculated as $S_{Q1} = 28.0$ kN/m, which is also subject to all constraint conditions. That is to say, after the NDC, the ultimate load level of the structure has increased up to 438 percent. With calculation done under load Case 1: S_G (5 kN/m) + S_{Q1} (28.0 kN/m) and all constraint conditions for the noncontrolled structure released, the static state results of noncontrol and NDC are shown in Table 3. It is clear that the ultimate load of S_{Q1} is subject to the allowable stress of the beam; that is, $|\sigma_B|_{\max}$ is close to 215 N/mm²; meanwhile, the adjustments of strut 1 and strut 3 all reach the upper bound.

TABLE 2: Static state results under load Case 1 with $S_{Q1} = 5.2 \text{ kN/m}$.

Notations	Working status factors	Compressive stress values of struts (N/mm^2)			Adjustment values of struts (mm)			Minimal and maximum tension values of cables (kN)		Maximum stress values of the beam (N/mm^2)
		σ_{A1}	σ_{A2}	σ_{A3}	e_{A1}	e_{A2}	e_{A3}	$N_{C,\min}$	$N_{C,\max}$	
Noncontrol results	$0.992\uparrow$	-51.23	-50.76	-51.23	0.00	0.00	0.00	503.60	535.10	77.15
LDC results	0.085	-59.18	-39.71	-59.18	261.60	-47.70	261.70	506.77	540.58	87.16
NDC results	0.035	-59.31	-39.52	-59.31	253.80	-66.00	253.50	506.84	540.63	85.90

TABLE 3: Static state results under load Case 1 with $S_{Q1} = 28.0 \text{ kN/m}$.

Notations	Working status factor	Compressive stress of struts (N/mm^2)			Adjustment value of struts (mm)			Minimal and maximum tension of cables (kN)		Maximum stress of beam (N/mm^2)
		σ_{A1}	σ_{A2}	σ_{A3}	e_{A1}	e_{A2}	e_{A3}	$N_{C,\min}$	$N_{C,\max}$	
Noncontrol results	4.247	-180.25	-174.15	-180.25	0.00	0.00	0.00	1637.07	1750.32	486.89
NDC results	0.516	-178.55	-151.45	-178.55	399.90 \uparrow	385.70	399.90 \uparrow	1557.37	1666.44	214.99 \uparrow

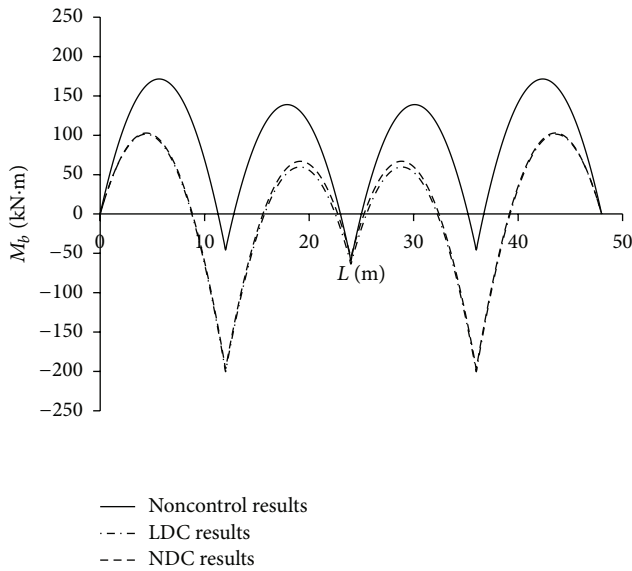


FIGURE 8: Moment state of the beam under load Case 1.

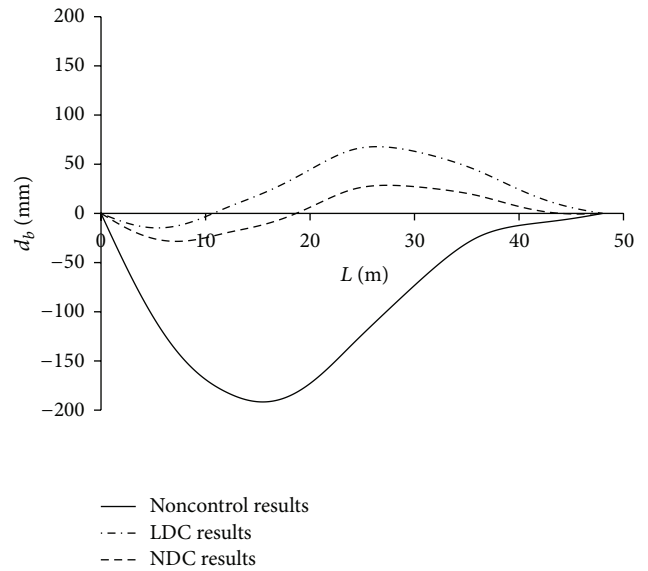


FIGURE 9: Displacement state of the beam under load Case 2.

The noncontrol results show that the displacement and stress values of the beam all largely exceed the limitation.

4.2. *Load Case 2: $S_G + S_{Q2}$.* Similarly, the ultimate load of S_{Q2} for noncontrolled BSS is calculated as $S_{Q2} = 4.3 \text{ kN/m}$. Table 4 shows all the static state results of noncontrol, LDC, and NDC under load Case 2: $S_G (5 \text{ kN/m}) + S_{Q2} (4.3 \text{ kN/m})$. Apparently, the ultimate load of S_{Q2} is still subject to the allowable displacement of the beam, and the adjustment effect of NDC is somewhat more significant than LDC. The adjustments of strut 1 and strut 3 reach the upper bound, and lower bound respectively, which indicates that wider adjustment range is required for unsymmetrically distributed loads.

The displacement and moment distributions of the beam are shown in Figures 9 and 10, respectively. After control, the displacement and moment states turn to be well distributed, and the negative influence of the unsymmetrical loads has decreased substantially.

For the adaptive BSS, the ultimate load of S_{Q2} is calculated as $S_{Q2} = 15.3 \text{ kN/m}$. It increases up to 256 percent after the NDC, which may be limited by the adjustment bound of the struts. Another round of calculation is conducted under load Case 2: $S_G (5 \text{ kN/m}) + S_{Q2} (15.3 \text{ kN/m})$, and all constraint conditions for the non-controlled structure are released. Results shown in Table 5 reveal that the ultimate load of S_{Q2} is still subject to the allowable displacement of the beam; meanwhile, the adjustments of strut 1 and strut 2 have reached the upper bound. The noncontrol results show that the displacement and stress values of the beam have largely exceeded the limitation as well.

4.3. *Load Case 3: $S_G + S_W$.* The ultimate upward load of S_W for noncontrolled BSS is calculated as $S_W = -3.0 \text{ kN/m}$. Table 6 presents calculation results under load Case 3: $S_G (5 \text{ kN/m}) + S_W (-3.0 \text{ kN/m})$. It turns out that the ultimate upward load of S_W is subject to the allowable minimal tension of the cable.

TABLE 4: Static state results under load Case 2 with $S_{Q2} = 4.3 \text{ kN/m}$.

Notations	Working status factors	Compressive stress values of struts (N/mm^2)			Adjustment values of struts (mm)			Minimal and maximum tension values of cables (kN)		Maximum stress values of the beam (N/mm^2)
		σ_{A1}	σ_{A2}	σ_{A3}	e_{A1}	e_{A2}	e_{A3}	$N_{C,\min}$	$N_{C,\max}$	
Noncontrol results	0.999 \uparrow	-37.40	-35.32	-33.68	0.00	0.00	0.00	352.66	375.00	96.48
LDC results	0.353	-41.93	-41.99	21.58	399.90 \uparrow	311.60	-394.10 \uparrow	359.53	383.38	80.29
NDC results	0.148	-42.87	-40.41	-22.53	399.40 \uparrow	233.10	-398.70 \uparrow	358.39	382.39	68.75

TABLE 5: Static state results under load Case 2 with $S_{Q2} = 15.3 \text{ kN/m}$.

Notations	Working status factors	Compressive stress values of struts (N/mm^2)			Adjustment values of struts (mm)			Minimal and maximum tension values of cables (kN)		Maximum stress values of the beam (N/mm^2)
		σ_{A1}	σ_{A2}	σ_{A3}	e_{A1}	e_{A2}	e_{A3}	$N_{C,\min}$	$N_{C,\max}$	
Noncontrol results	3.513	-76.02	-63.63	-52.13	0.00	0.00	0.00	623.13	665.73	476.22
NDC results	0.991 \uparrow	-79.05	-75.39	-31.05	399.90 \uparrow	399.90 \uparrow	-354.90	625.84	669.20	202.83

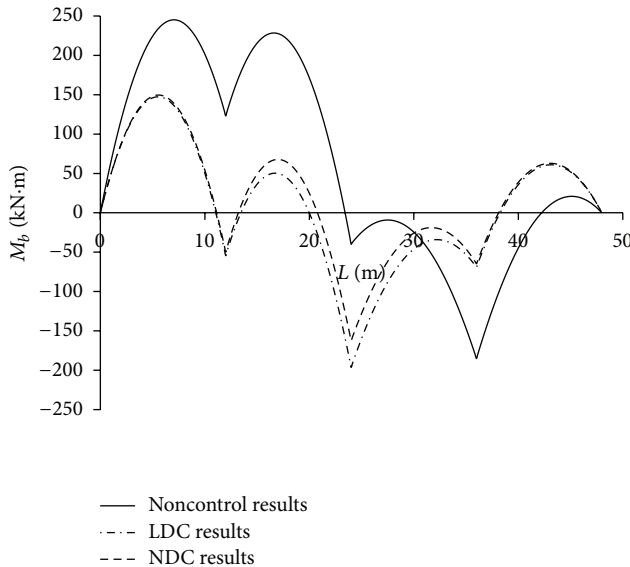


FIGURE 10: Moment state of the beam under load Case 2.

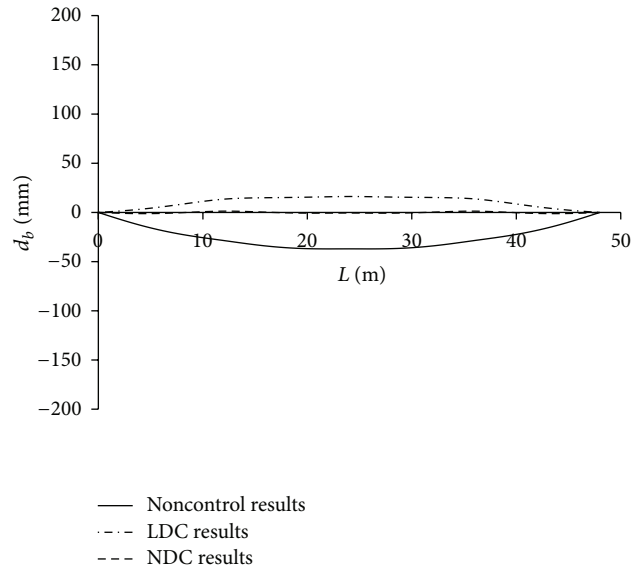


FIGURE 11: Displacement state of the beam under load Case 3.

All the static state results are small and close, which means the effect of adjustment is not that obvious.

As shown in Figures 11 and 12, the improvements of the displacement and moment states after control are slight.

Finally, the ultimate load of S_W for the adaptive BSS is calculated as $S_W = -3.3 \text{ kN/m}$ which increases only 10 percent. Calculation under load Case 3: $S_G (5 \text{ kN/m}) + S_W (-3.3 \text{ kN/m})$ is done with all constraint conditions for the noncontrolled structure released. The static state results of noncontrol and NDC are shown in Table 7. Obviously, the ultimate load of S_W is still subject to the allowable minimal tension of the cable; meanwhile, the adjustments of strut 2 reach the lower bound. The noncontrol results indicate that the minimal tension value of the cable has exceeded the limitation significantly.

5. Conclusions

The adaptive BSS is a typical smart structure that can optimize its own working status by controlling the length of several active struts. The core issue here is to determine the length adjustment values of the active struts according to the working status of the structure. In this paper, an optimization model of adaptive BSS with multiple active struts is established at first. It is based on a sensitivity analysis method and takes displacement as control objective. Then, on the basis of an SA algorithm, an LDC process has been proposed to calculate the adjustment. An iteration procedure consisting of the LDC process and a nonlinear iteration is constructed afterwards to achieve the displacement control of structures with nonlinear behaviour. In the final section, an example of a three-strut active BSS under different external loads has been

TABLE 6: Static state results under load Case 3 with $S_W = -3.0$ kN/m.

Notations	Working status factors	Compressive stress values of struts (N/mm ²)			Adjustment values of struts (mm)			Minimal and maximum tension values of cables (kN)		Maximum stress values of the beam (N/mm ²)
		σ_{A1}	σ_{A2}	σ_{A3}	e_{A1}	e_{A2}	e_{A3}	$N_{C,min}$	$N_{C,max}$	
Noncontrol results	0.194	-9.74	-9.72	-9.74	0.00	0.00	0.00	94.56↑	104.50	14.71
LDC results	0.084	-11.74	-7.83	-11.79	141.20	-191.40	147.90	103.08	109.73	19.25
NDC results	0.007	-11.52	-7.89	-11.51	125.90	-190.60	125.60	101.81	108.35	16.42

TABLE 7: Static state results under load Case 3 with $S_W = -3.3$ kN/m.

Notations	Working status factors	Compressive stress values of struts (N/mm ²)			Adjustment values of struts (mm)			Minimal and maximum tension values of cables (kN)		Maximum stress values of the beam (N/mm ²)
		σ_{A1}	σ_{A2}	σ_{A3}	e_{A1}	e_{A2}	e_{A3}	$N_{C,min}$	$N_{C,max}$	
Noncontrol results	0.164	-8.27	-8.26	-8.27	0.00	0.00	0.00	83.77	88.82	12.49
NDC results	0.428	-12.06	-5.02	-12.02	269.90	-399.90↑	261.60	93.97↑	100.29	30.85

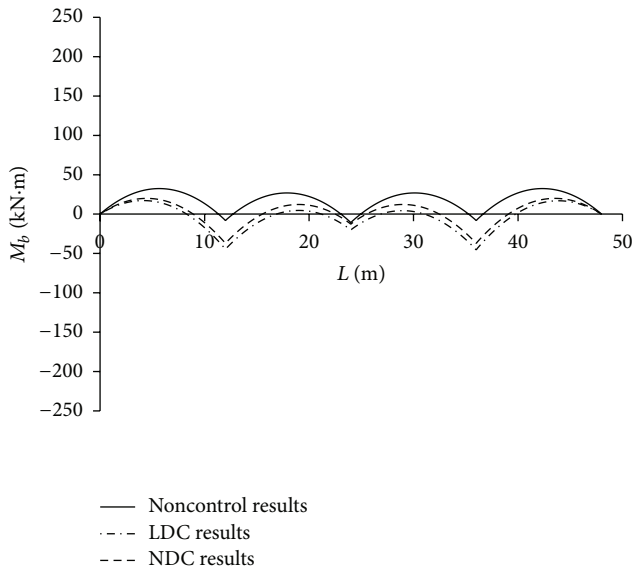


FIGURE 12: Moment state of the beam under load Case 3.

carried out to verify the feasibility and accuracy of the static control algorithm. With the example study completed, some conclusions are summarized as follows.

- (1) As a semirigid structure, the BSS has certain non-linear behaviour. Comparisons between results from the NDC and LDC show that the computational-controlled effect of the NDC is somewhat more significant than LDC.
- (2) When the structure is under downward loads, the working status of the adaptive BSS has been significantly improved after control, and the adaptive BSS has much stronger capability than the non-controlled one. To unsymmetrical distributed loads, wider adjustment range of the active struts is required.

Obviously, the displacement and moment states of the beam become well distributed after control.

- (3) The upward loads make the cable slack, and the capability of the structure is mainly subject to the allowable minimal tension of the cable. The adjustment effect of the active struts to the upward loads is not obvious.

Acknowledgments

The work described in this paper was financially supported by the National Key Technology R&D Program (2012BAJ07B03), the National Science Foundation of China (Grant no. 51178415), and Qianjiang Scholar Foundation of Zhejiang Province (2013R10038).

References

- [1] M. Saitoh, "Hybrid form-resistance structure," in *Shells, Membranes, and Space Frames: Proceedings of the IASS Symposium on Membrane Structures and Space Frames, Osaka, Japan, Butterworth-Heinemann Limited, 1986.*
- [2] M. Saitoh, A. Okada, K. Maejima, and T. Gohda, "Study on mechanical characteristics of a light-weight complex structure composed of a membrane and a beam string structure," in *Proceedings of the IASS-ASCE International Symposium on Spatial, Lattice and Tension Structures*, pp. 632–641, April 1994.
- [3] Y. Wang and K. H. Law, "Wireless sensor networks in smart structural technologies," in *Recent Advances in Wireless Communications and Networks*, J.-C. Lin, Ed., InTech, 2011.
- [4] Z.-D. Xu, Y.-P. Shen, and Y.-Q. Guo, "Semi-active control of structures incorporated with magnetorheological dampers using neutral networks," *Smart Materials and Structures*, vol. 12, no. 1, pp. 80–87, 2003.
- [5] Z.-D. Xu, "Earthquake mitigation study on viscoelastic dampers for reinforced concrete structures," *Journal of Vibration and Control*, vol. 13, no. 1, pp. 29–43, 2007.
- [6] Z.-D. Xu, Q. Tu, and Y.-F. Guo, "Experimental study on vertical performance of multi-dimensional earthquake isolation and

- mitigation devices for long-span reticulated structures,” *Journal of Vibration and Control*, vol. 18, no. 13, pp. 1971–1985, 2012.
- [7] H. Li, H. Qian, and G. Song, “Experimental and analytical investigation on innovative hybrid shape memory alloys dampers for structural control,” in *Active and Passive Smart Structures and Integrated Systems 2008*, vol. 6928 of *Proceedings of SPIE*, March 2008.
- [8] G. Song, B. Kelly, B. N. Agrawal, P. C. Lam, and T. S. Srivatsan, “Application of shape memory alloy wire actuator for precision position control of a composite beam,” *Journal of Materials Engineering and Performance*, vol. 9, no. 3, pp. 330–333, 2000.
- [9] L. Li, G. Song, and J. Ou, “Hybrid active mass damper (AMD) vibration suppression of nonlinear high-rise structure using fuzzy logic control algorithm under earthquake excitations,” *Structural Control and Health Monitoring*, vol. 18, no. 6, pp. 698–709, 2011.
- [10] V. Sethi and G. Song, “Multimodal vibration control of a flexible structure using piezoceramic sensor and actuator,” *Journal of Intelligent Material Systems and Structures*, vol. 19, no. 5, pp. 573–582, 2008.
- [11] G. Li and L. A. Fahnestock, “Seismic response of single-degree-of-freedom systems representing low-ductility steel concentrically braced frames with reserve capacity,” *Journal of Structural Engineering*, vol. 139, no. 2, pp. 199–211, 2013.
- [12] G. Li, L. A. Fahnestock, and H.-N. Li, “Simulation of steel brace hysteretic response using the force analogy method,” *Journal of Structural Engineering*, vol. 139, no. 4, pp. 526–536, 2013.
- [13] T. Noack, J. Ruth, and U. Müller, “Adaptive hybrid structures,” in *Proceedings of the International Conference on Adaptable Building Structures*, Eindhoven, The Netherlands, 2006.
- [14] W. Sobek and P. Teuffel, “Adaptive systems in architecture and structural engineering,” in *Smart Structures and Materials 2001: Smart Systems for Bridges, Structures, and Highways*, vol. 4330 of *Proceedings of SPIE*, pp. 36–45, March 2001.
- [15] J. Du, H. Bao, D. Yang, Y. Wang, and C. Cui, “Initial equilibrium configuration determination and shape adjustment of cable network structures,” *Mechanics Based Design of Structures and Machines*, vol. 40, no. 3, pp. 277–291, 2012.
- [16] J. Sobieszczanski-Sobieski, J.-F. Barthelemy, and K. M. Riley, “Sensitivity of optimum solutions of problem parameters,” *AIAA Journal*, vol. 20, no. 9, pp. 1291–1299, 1982.

Research Article

Optimal Design of Liquid Dampers for Structural Vibration Control Based on GA and H_{∞} Norm

Linsheng Huo, Wenhe Shen, Hongnan Li, and Yaowen Zhang

State Key Laboratory of Coastal and Offshore Engineering, Dalian University of Technology, Dalian 116024, China

Correspondence should be addressed to Linsheng Huo; lshuo@dlut.edu.cn

Received 4 July 2013; Accepted 7 October 2013

Academic Editor: Gang Li

Copyright © 2013 Linsheng Huo et al. This is an open access article distributed under the Creative Commons Attribution License, which permits unrestricted use, distribution, and reproduction in any medium, provided the original work is properly cited.

This paper focused on the optimal design of liquid dampers for the seismic response control of structures. The H_{∞} norm of the transfer function from the ground motion to the structural response is selected as the optimal objective. The optimization procedure is carried out by using Genetic Algorithms (GAs) in order to reach an optimal solution. The proposed method has the advantages that it is unnecessary to solve the equation of motion for the control system and that the obtained optimal parameters of dampers are not dependent on the ground motion records. The influences of weighted functions on the optimization results are analyzed. The generality and effectiveness of the proposed method are verified by the time history analysis of a 3-story structure subjected to earthquake records in different sites. The results show that the structural responses can be effectively reduced subjected to earthquake excitation at different sites.

1. Introduction

The installation of vibration absorbers on tall buildings or other flexible structures can be a successful method for reducing the effects of dynamic excitations, such as strong wind or earthquakes, which may exceed either serviceability or safety criteria. Tuned liquid column damper (TLCD) is an effective passive control device by the motion of liquid in a column container. A TLCD is a U-shaped tube of uniform rectangular or circle cross section, containing liquid. Vibration energy is transferred from the structure to the TLCD liquid through the motion of the rigid container exciting the TLCD liquid. And the vibration of a structure is suppressed by a TLCD through the gravitational restoring force acting on the displaced TLCD liquid and the energy is dissipated by the viscous interaction between the liquid and the rigid container, as well as liquid head loss due to orifices installed inside the TLCD container. The potential advantages of liquid vibration absorbers include low manufacturing and installation costs, the ability of the absorbers to be incorporated during the design stage of a structure or to be retrofitted to serve a remedial role, relatively low maintenance requirements, and the availability of the liquid to be used

for emergency purposes or for the everyday function of the structure if fresh water is used [1, 2].

Analytical and experimental research works on this type of vibration reduction approach have been conducted, in which viscous interaction between a liquid and solid boundary has been investigated and used to control vibration [3, 4]. Their experiments, defining the relationship between the coefficient of liquid head loss (as well as its dependence on the orifice opening ratio) and the liquid damping, confirm the validity of their proposed equation of motion in describing liquid column relative motion under moderate excitation. A variation of TLCD, called a liquid column vibration absorber (LCVA), has also been investigated, which has different cross-sectional areas in its vertical and horizontal sections depending on performance requirements [5–8]. Yan and Li presented the adjustable frequency tuned liquid column damper by adding springs to the TLCD system, which modified the frequency of TLCD and expanded its application ranges [9]. Gao et al. analyzed the characteristics of multiple liquid column dampers (MTLCD) [10]. It was found that the frequency of range and the coefficient of liquid head loss have significant effects on the performance of a MTLCD; increasing the number of TLCD can enhance the efficiency of

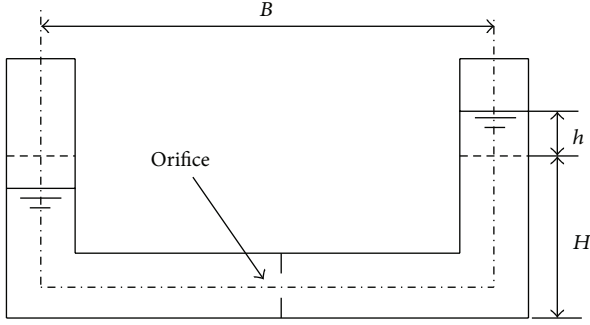


FIGURE 1: Configuration of TLCD.

MTLCD, but no further significant enhancement is observed when the number of TLCD is over five. It was also confirmed that the sensitivity of an optimized MTLCD to its central frequency ratio is not much less than that of an optimized single TLCD to its frequency ratio, and an optimized MTLCD is even more sensitive to the coefficient of head loss.

How to decide the parameters and location of dampers in structures to achieve the optimal response reduction is still an open problem currently. One of the commonly used methods for the optimization of the damper parameters is to set the objective function to be the stochastic response of structures based on the seismic frequency spectrum input and the optimal parameters can be achieved by Genetic Algorithms (GAs). Another commonly used method of optimization is to set the objective function to be the structural responses or their combination in time domain based on the actual earthquake records. The shortcoming for the above two methods is that the equation of motion of the structural system has to be solved in every optimization step, which is time consuming. Besides, the optimal parameters acquired by the above methods are related to specific earthquakes and may not be optimal in some earthquakes. Hence, it is necessary to find a more general and effective method to optimize the parameters of liquid dampers to reduce structural vibration. The active control theory has been used to optimize the parameters of passive control systems and a lot of results have been achieved [11–22]. Based on H_∞ norm and Genetic Algorithms (GAs), this paper proposed the optimization method for liquid dampers, which has the advantages that it is unnecessary to solve the equation of motion for the system and that the optimized parameters are not related to specific earthquake records.

2. Problem Descriptions

2.1. Equation of Motion for TLCD. The configuration of the tuned liquid column damper (TLCD) is shown in Figure 1. According to Lagrange theory, the equation of motion for TLCD on the structure subjected earthquake excitation is derived as

$$\rho A (2H + B) \ddot{h} + \frac{1}{2} \rho A \xi |\dot{h}| \dot{h} + 2\rho A g h = -\rho A B (\ddot{x}_n + \ddot{x}_g), \quad (1)$$

where ρ is the density of the liquid; h is the relative movement of the liquid in TLCD; H is the static height of the liquid in the container; A is the cross-sectional area of TLCD; g is the gravitational acceleration; B is the length of the horizontal part of TLCD; ξ is the coefficient of head loss, which can be controlled by varying the orifice area; \ddot{x}_n is the acceleration of the n th floor where TLCD is installed; \ddot{x}_g is the acceleration of ground motion.

Due to the nonlinear damping of the aforementioned equation, by the equivalently linearization of it (1) can be converted to

$$m_T \ddot{h} + c_T \dot{h} + k_T h = -\alpha_x m_T (\ddot{x}_n + \ddot{x}_g), \quad (2)$$

where $m_T = \rho A L_e$ is the mass of the liquid in the TLCD, $L_e = 2H + B$ is the length of the liquid in the TLCD, $c_T = (\rho A \xi |\dot{h}|)/2$ is the equivalent damping of the TLCD, and $k_T = 2\rho A g$ is the “stiffness” of the liquid in vibration. Hence, the circular frequency of the motion can be written as $\omega_T = \sqrt{k_T/m_T} = \sqrt{2g/L_e}$. α_x is the shape function of the liquid damper, written as $\alpha_x = B/L_e$.

2.2. Mathematical Model of the Control System. For an n -story shear frame structure, the dynamics of the structural building without TLCD can be described as

$$M\ddot{x} + C\dot{x} + Kx = -MI\ddot{x}_g, \quad (3)$$

where M , C , and K are the mass, damping, and stiffness matrices of the structural building with the dimension of $n \times n$, respectively; I is an identity vector with the dimension of $n \times 1$; the relative displacement vector x is defined as

$$x = [x_1 \ x_2 \ \cdots \ x_n]^T, \quad (4)$$

where x_i is the relative displacement of the i th floor. So the equation of motion for the structural building instrumented with TLCD on the top floor as shown in Figure 2 can be formulated as

$$M_s \ddot{q} + C_s \dot{q} + K_s q = -M_s I \ddot{x}_g, \quad (5)$$

where

$$M_s = \begin{bmatrix} m_1 & 0 & 0 & 0 \\ 0 & \ddots & 0 & 0 \\ 0 & 0 & m_n + m_T & \alpha m_T \\ 0 & 0 & \alpha m_T & m_T \end{bmatrix}, \quad K_s = \begin{bmatrix} k_1 & 0 & 0 & 0 \\ 0 & \ddots & 0 & 0 \\ 0 & 0 & k_n & 0 \\ 0 & 0 & 0 & k_T \end{bmatrix}, \quad C_s = \begin{bmatrix} c_1 & 0 & 0 & 0 \\ 0 & \ddots & 0 & 0 \\ 0 & 0 & c_n & 0 \\ 0 & 0 & 0 & c_T \end{bmatrix}, \quad (6)$$

$$q = (q_1 \ \cdots \ q_n \ q_{n+1})^T = (x_1 \ \cdots \ x_n \ h)^T.$$

The elements m_i , c_i , and k_i in matrices M_s , C_s , and K_s are the mass, damping, and stiffness of the i th floor. Equation (5) can be expressed by the state space form as

$$\begin{aligned} \dot{z}(t) &= Az(t) + Bw(t), \\ y(t) &= Cz(t) + Dw(t), \end{aligned} \quad (7)$$

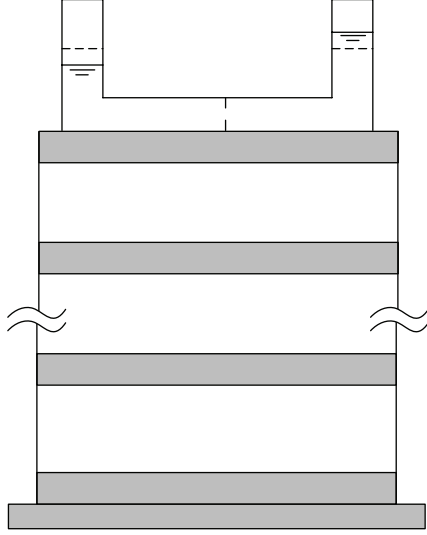


FIGURE 2: The structure with TLCD.

where $z(t)$ and $y(t)$ are, respectively, the state vector and output vector of the system and

$$z(t) = \begin{bmatrix} q(t) \\ \dot{q}(t) \end{bmatrix}, \quad A = \begin{bmatrix} 0 & I \\ -M_s^{-1}K_s & -M_s^{-1}C_s \end{bmatrix}, \quad (8)$$

$$B = \begin{bmatrix} 0 \\ -I \end{bmatrix}, \quad w(t) = \ddot{u}_g(t).$$

The matrices C and D would be determined according to the optimization object.

2.3. H_∞ Norm. The transfer function of (7) can be expressed by

$$T(s) = C(sI - A)^{-1}B + D. \quad (9)$$

The H_∞ norm is defined as

$$\|T(s)\|_\infty = \sup_w \sigma_{\max} [T(jw)]. \quad (10)$$

In another word, the H_∞ norm is the maximum singular value of frequency response of the system. In the frequency domain, the H_∞ norm can be derived by

$$\|T(s)\|_\infty = \sup_{\|w(t)\|_2 \neq 0} \frac{\|y(t)\|_2}{\|w(t)\|_2} = \sup_{\|w(t)\|_2=1} [\|y(t)\|_2], \quad (11)$$

where $\|y(t)\|_2$ is the L_2 norm of the output $y(t)$ and can be determined by the following equation:

$$\|y(t)\|_2 = \left(\int_0^\infty y^T(t) y(t) dt \right)^{1/2}. \quad (12)$$

It can be found that $\|y(t)\|_2$ is the energy measurement of the output $y(t)$. Similarly, the L_2 norm of $w(t)$ is the energy measurement of the seismic input, which can be determined by

$$\|w(t)\|_2 = \left(\int_0^\infty w^T(t) w(t) dt \right)^{1/2}. \quad (13)$$

If the H_∞ norm of the transfer function $T(s)$ achieves its minimum, the energy measurement of the output will meet its minimum and the control performance of the system will be in its best state based on H_∞ norm.

3. Selection of the Weighted Function

Theoretically, the optimum control based on H_∞ norm is to meet the minimum of H_∞ norm in the frequency domain. However, it is impractical to control the dynamic response of the system in the whole frequency domain due to the property limitation of dampers. Hence, the weighted functions are usually used to regulate the system's performance in the active controller design or parameters optimization of passive dampers. The advantages of using weighted functions are obvious in controller design. First, some components of a vector signal are usually more important than others. Second, each component of the signal may not be measured in the same units. Also, we might be primarily interested in the dynamic response of a certain frequency range [23]. Therefore, some frequency-dependent weights must be chosen to obtain a high performance controller. Two weighted functions, $W_g(s)$ and $W_1(s)$, will be used to facilitate the parameter optimization of liquid dampers, in which $W_g(s)$ and $W_1(s)$ are used to weigh the seismic excitation and structural dynamics, respectively. However, there is no definite conclusion how the weighted functions will influence the optimization results and how to select appropriate weighted functions to get the optimal results with less computational efforts. This paper will analyze the influences of weighted functions on the optimal results of liquid dampers.

The weighted function W_g is used to reflect the frequency content of an earthquake. The most commonly used stochastic model of earthquakes is the Kanai-Tajimi spectrum, as shown in the following equation:

$$S(\omega) = S_0 \left[\frac{\omega_g^4 + 4\omega_g^2 \zeta_g^2 \omega^2}{(\omega^2 - \omega_g^2)^2 + 4\omega_g^2 \zeta_g^2 \omega^2} \right]. \quad (14)$$

The weighted function W_g is chosen as the square root of the Kanai-Tajimi spectrum:

$$W_g(s) = \frac{\sqrt{S_0} (\omega_g^2 + 2\zeta_g \omega_g s)}{s^2 + 2\zeta_g \omega_g s + \omega_g^2}. \quad (15)$$

The values of ω_g and ζ_g can be determined according to the site types.

For the regulated response, we are only interested in the low-frequency response. Therefore, the weighted function W_1 can be selected as a low-pass filter. The influences of weighted functions on the optimization results will be discussed in the following section.

4. Genetic Algorithm

Genetic Algorithm (GA) is a search heuristic that mimics the process of natural evolution to generate useful solutions to optimization and search problems. In a genetic algorithm,

a population of candidate solutions to an optimization problem is evolved toward better solutions. Each candidate solution has a set of properties which can be mutated and altered. The evolution usually starts from a population of randomly generated individuals and is an iterative process, with the population in each iteration called a generation. In each generation, the fitness of every individual in the population is evaluated; the fitness is usually the value of the objective function in the optimization problem being solved. The more fit individuals are stochastically selected from the current population, and each individual's property is modified to form a new generation. The new generation of candidate solutions is then used in the next iteration of the algorithm. Commonly, the algorithm terminates when either a maximum number of generations have been produced or a satisfactory fitness level has been reached for the population. A typical genetic algorithm requires a genetic representation of the solution domain and a fitness function to evaluate the solution domain. Once the genetic representation and the fitness function are defined, a GA proceeds to initialize a population of solutions and then to improve it through repetitive application of the mutation, crossover, inversion and selection operators. The steps of problem solution by genetic algorithm can be summarized as follows.

- (1) Determine variables and constraint conditions; in other words, determine the individuals' form and the solution space.
- (2) Define the fitness function. The fitness function is defined as the H_∞ norm of the controlled system.
- (3) Find the chromosome coding and decoding method for the feasible solution.
- (4) Define the rules of transforming the value of objective function to individual fitness.
- (5) Define the genetic operators, which are the methods of selection, crossover, and mutation to generate the next generation.
- (6) Choose the parameters of the genetic algorithm, including the population size, iteration number, termination condition, selection probability, crossover probability, and mutation probability.
- (7) Run the genetic algorithm and acquire the individuals with maximum fitness values.

5. Numerical Analysis

5.1. Structural Parameters. A 3-story frame structure is used as a numerical example to verify the significance of weighted

functions. The values of mass, stiffness and damping matrices are, respectively, as follows:

$$M = \begin{bmatrix} 5 & & \\ & 5 & \\ & & 5 \end{bmatrix} \times 10^5 \text{ Kg},$$

$$C = \begin{bmatrix} 1.3506 & -0.5286 & 0 \\ -0.5286 & 1.3506 & -0.5286 \\ 0 & -0.5286 & 0.8220 \end{bmatrix} \times 10^6 \text{ N} \cdot \text{s/m}, \quad (16)$$

$$K = \begin{bmatrix} 4 & -2 & 0 \\ -2 & 4 & -2 \\ 0 & -2 & 2 \end{bmatrix} \times 10^8 \text{ N/m}.$$

The natural frequencies of the structure without control are 1.58 Hz, 4.44 Hz, and 6.42 Hz, respectively. A TLCD is installed on the top floor to control the structural vibration.

With the consideration of structural safety, optimization objective is set to make the H_∞ norm of the transfer function of the top floor's displacement minimum. Parameters of liquid dampers to be optimized include mass ratio μ , frequency ratio f , and damping ratio d , of which their physical meanings and optimization ranges are presented as follows.

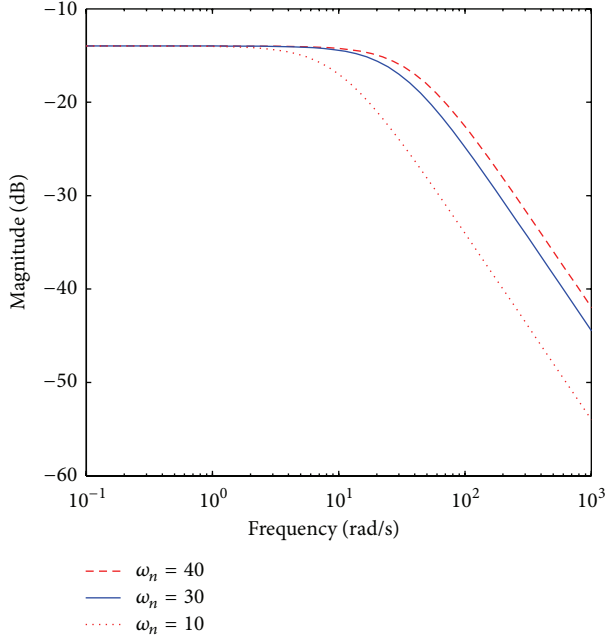
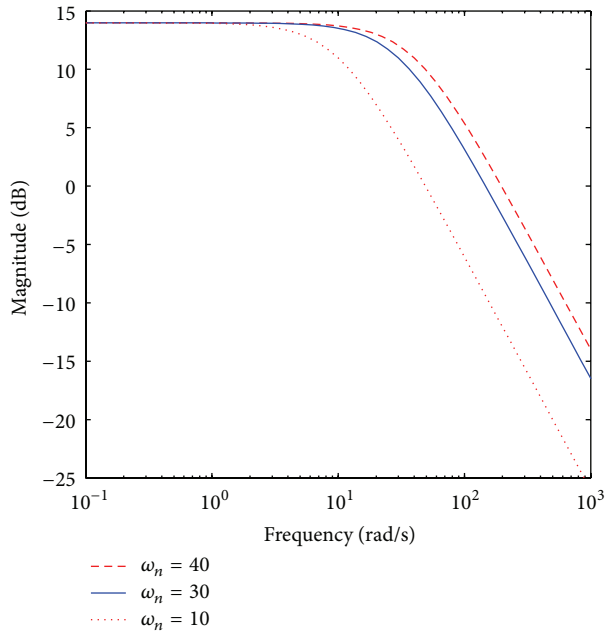
- (1) Mass ratio μ means the ratio of the mass of the liquid in the container to the one of the whole structure. In the paper, the ratio is supposed to be in the range from 0.1% to 3% according to the actual condition.
- (2) Frequency ratio f is the ratio of the frequency of the damper to the first frequency of the structure. It is supposed to be in the range from 0 to 2.5.
- (3) Damping ratio d denotes the ratio of the damper's damping to its critical one. It is supposed to be in the range from 0% to 10%.

5.2. First-Order Weighted Function $W_1(s)$. For building structures with multiple degrees of freedom, the first few modes will dominate the dynamic response. Generally, the high-order modes are usually ignored and only the first few modes are used for analysis. The low-pass filter can regulate the system response in the low-frequency range and can be used as the weighted function. The influence of the first-order weighted function $W_1(s)$ on the optimization result will be analyzed in this section. The first-order weighted function $W_1(s)$ can be written as

$$W_1(s) = \frac{k}{s/\omega_n + 1}, \quad (17)$$

where k means the system gain and ω_n is the cut-off frequency.

5.2.1. The Influence of ω_n on Optimization Results. The preliminary analysis shows that the frequency contents of the top floor's displacement are below 40 rad/s. Given the value of k to be 0.2 and 5, and ω_n to be 10 rad/s, 30 rad/s, and 40 rad/s, then a series of frequency response curves of $W_1(s)$ can be obtained, as shown in Figures 3 and 4.


 FIGURE 3: Frequency response curve of $W_1(k = 0.2)$.

 FIGURE 4: Frequency response curve of $W_1(k = 5)$.

The parameters of TLCD with the above weighted functions are optimized by genetic algorithm and the results are shown in Table 1, in which γ_∞ means the H_∞ norm of the system with optimized values. It can be seen from Table 1 that the values of ω_n and k have significant influences on the optimal mass ratio and frequency ratio of TLCD. The frequency response curves of the top floor's displacement for the structure without control and with TLCD control in different optimal parameters are shown in Figures 5 and 6. It can be

TABLE 1: The optimal parameters of TLCD.

k	ω_n	μ	f	d	γ_∞
0.2	10	0.018016	0.90971	0.099155	0.0074883
	30	0.016761	0.93214	0.099347	0.0097854
	40	0.013865	0.94394	0.099712	0.010142
5	10	0.023371	0.88797	0.098486	0.18629
	30	0.015675	0.93541	0.096908	0.24828
	40	0.018858	0.92501	0.099791	0.24220

TABLE 2: The optimal parameters of liquid dampers.

ω_n	k	μ	f	d	γ_∞
10	0.2	0.018016	0.90971	0.099155	0.0556
10	2	0.027219	0.87352	0.09968	0.0554
10	5	0.01647	0.9038	0.099394	0.0556
10	10	0.019613	0.90336	0.09991	0.0500

found from the figures that the top floor's displacement of the structure can be suppressed obviously with TLCD control. For the controlled structure with optimized parameters in consideration of the weighted function, compared with the one without consideration of the weighted function, the peak response reduces the most when ω_n is 10 rad/s.

5.2.2. The Influence of k on Optimization Results. Given the value of ω_n as 10 rad/s and k as 0.2, 2, 5, and 10, respectively, the optimal parameters of liquid dampers can be obtained by GA, as shown in Table 2. The corresponding frequency response curves are shown in Figure 7.

It can be seen from Table 2 that the variation of k has significant influences on the optimal value of the mass ratio μ and little influence on the frequency ratio f and damping ratio d . Figure 7 shows that the structural displacement can be effectively controlled with optimized TLCD parameters and the best control case is the one optimized with the first-order weighted function of $\omega_n = 10$ rad/s and $k = 2$.

5.3. Second-Order-Weighted Function. The second-order weighted function can be written as

$$W_2(s) = \frac{k}{(s/\omega_n)^2 + 2(\zeta/\omega_n)s + 1}. \quad (18)$$

With fixed $k = 2$ and $\omega_n = 10$ rad/s, the effect of structural response by different values of ζ is analyzed in the following. Take ζ as 0.1, 0.2, and 0.5, and then a series of frequency response curves of second-order weighted function can be obtained as shown in Figure 8.

With the second-order weighted function, the parameters of the tuned liquid temper are optimized by genetic algorithm. The results are shown in Table 3, and the corresponding frequency response curves in are shown Figure 9. Table 3 shows that the optimized mass ratio μ decreases and better control effect can be achieved with the increasing of ζ . Figure 9 shows that the top floor's response is suppressed effectively with optimized TLCD parameters.

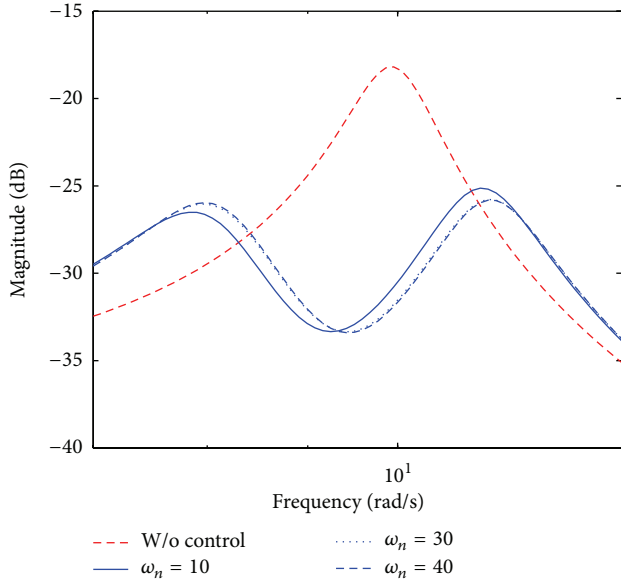


FIGURE 5: Frequency response curve of top floor's displacement ($k = 0.2$).

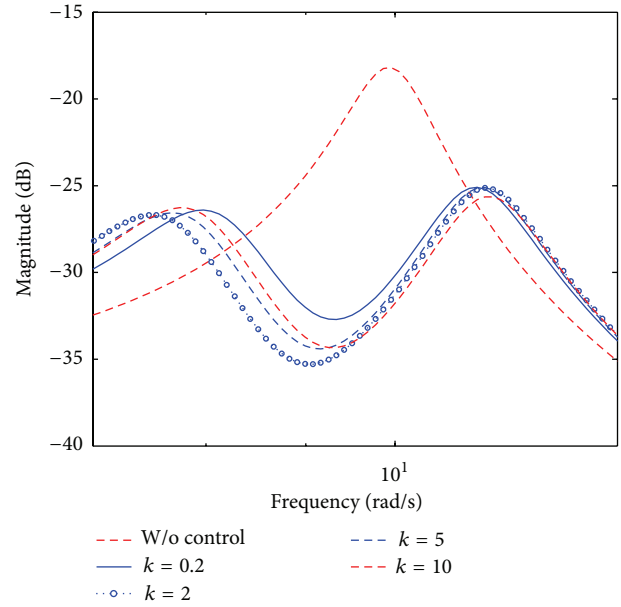


FIGURE 7: Frequency response curve of top floor's displacement.

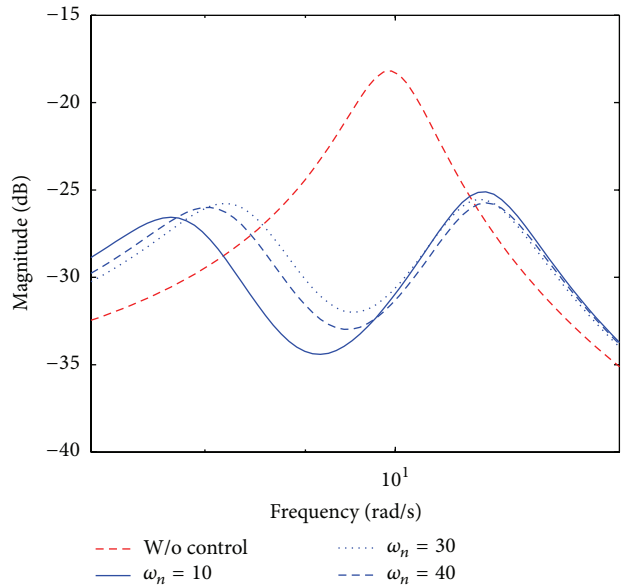


FIGURE 6: Frequency response curve of top floor's displacement ($k = 5$).

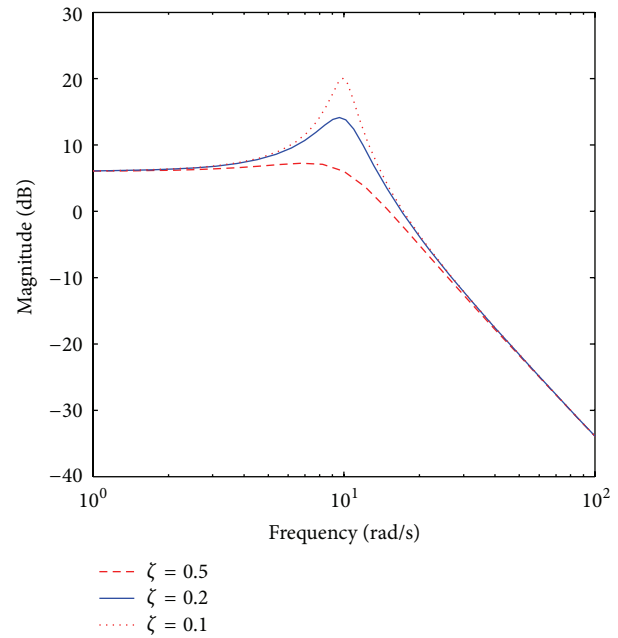


FIGURE 8: Frequency response curve of W_2 .

TABLE 3: The optimal parameters of liquid dampers.

ζ	μ	f	d	γ_∞
0.1	0.028854	0.92344	0.099003	0.25339
0.2	0.027841	0.89932	0.099837	0.19396
0.5	0.011828	0.92507	0.098664	0.10967

Different weighted functions result in the different optimized parameters and different dynamic response curves. The best control performance can be achieved with the ζ of 0.1.

To achieve the better vibration control effect, the use of the first-order and second-order weighted function is compared as follows. The mathematical formulation of the first-order weighted function $W_1(s)$ and second-order weighted function $W_2(s)$ is expressed by $W_1(s) = 2/((s/10) + 1)$ and $W_2(s) = 2/((s^2/100) + (0.2/10)s + 1)$. The frequency response curves of $W_1(s)$ and $W_2(s)$ are shown in Figure 10. The frequency response curves of top floor's displacement and acceleration with optimized TLCD parameters weighted by $W_1(s)$ and $W_2(s)$ are shown in Figures 11 and 12.

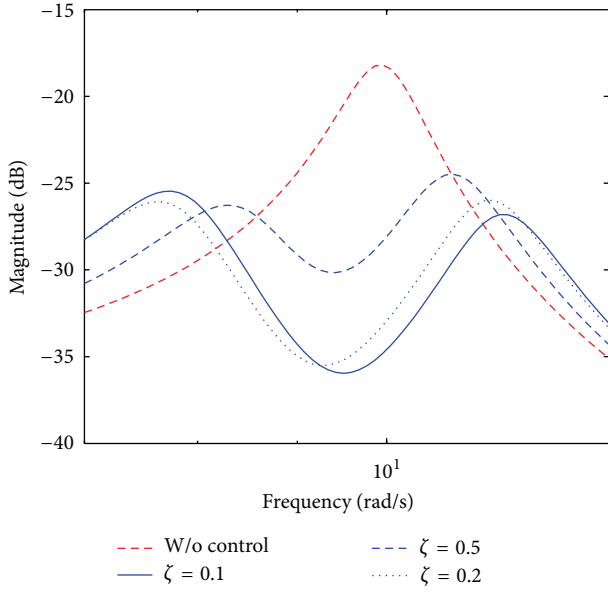


FIGURE 9: Frequency response curve of top floor's displacement.

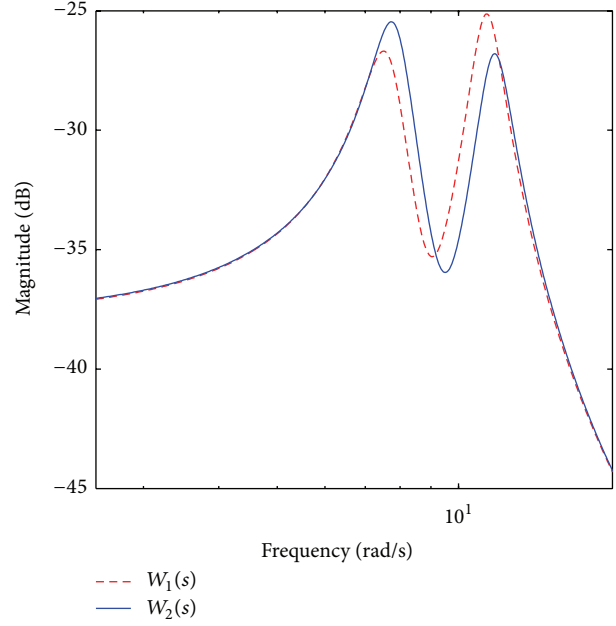


FIGURE 11: Frequency response curve of top floor's displacement.

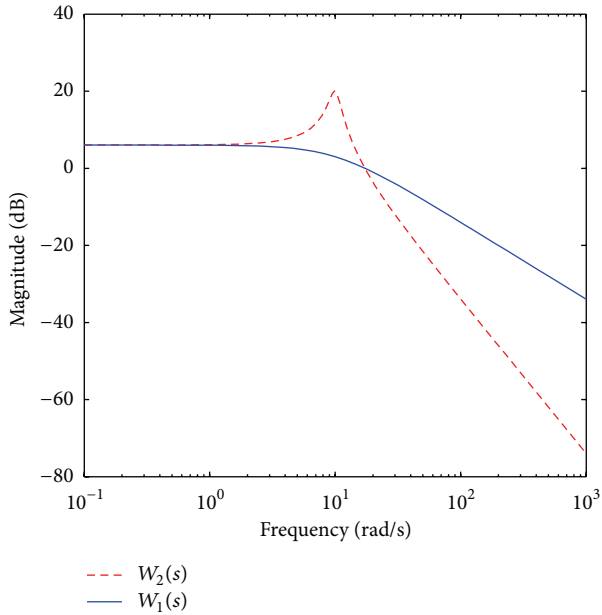


FIGURE 10: Frequency response curves of $W_1(s)$ and $W_2(s)$.

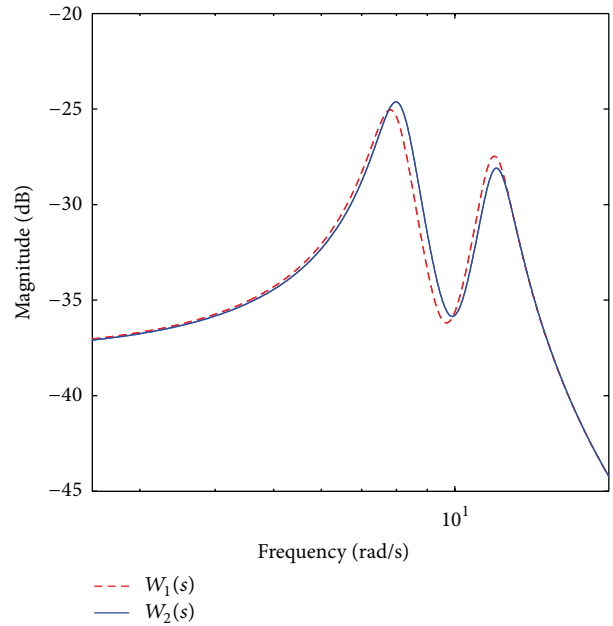


FIGURE 12: Frequency response curve of top floor's acceleration.

It can be seen from the figures that there is little difference for the control results with optimized TLCD parameters weighted by the first-order weighted function or the second-order one. Hence, the low-order weighted function should be selected to facilitate the controller design.

5.4. Time History Analysis. To verify the control performance of TLCD with optimized parameters, the seismic responses of the 3-story building are analyzed in the time domain. Four earthquake records, Kobe, El Centro, Northridge, and Hach, are used as excitation for different sites. The mass ratio,

frequency, and damping ratio of TLCD are 0.013865, 0.94394, and 0.099712, as shown in Table 1. The time histories of top floor's displacement and acceleration are shown in Figures 13, 14, 15, 16, 17, 18, 19, and 20. The detailed values of seismic responses and reduction ratios of the structure at different earthquake records are listed in Table 4. From these figures and the table, it can be concluded that the structural response can be effectively reduced subjected to earthquake excitation at different sites.

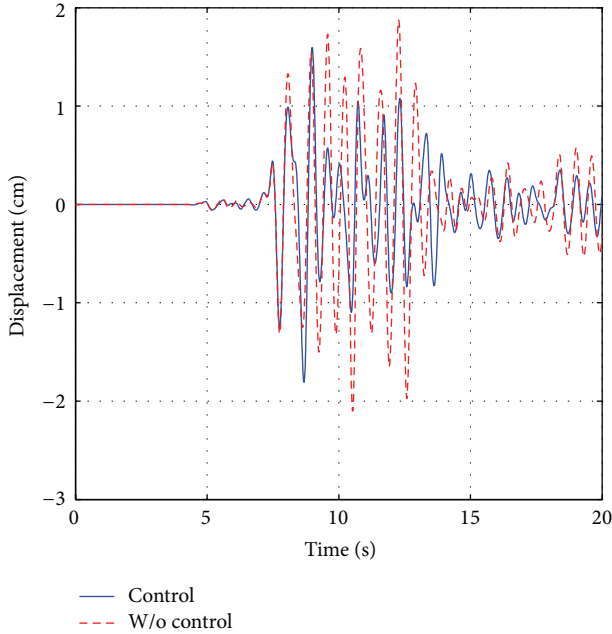


FIGURE 13: Time history of top floor's displacement (Kobe wave).

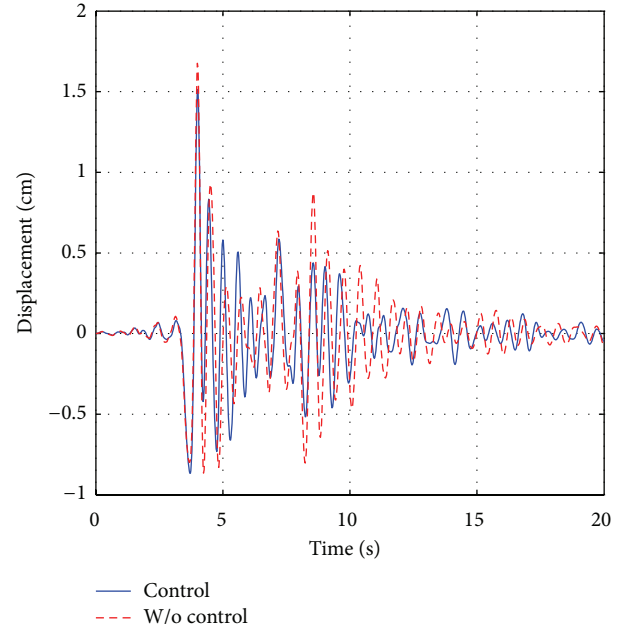


FIGURE 15: Time history of top floor's displacement (Northridge wave).

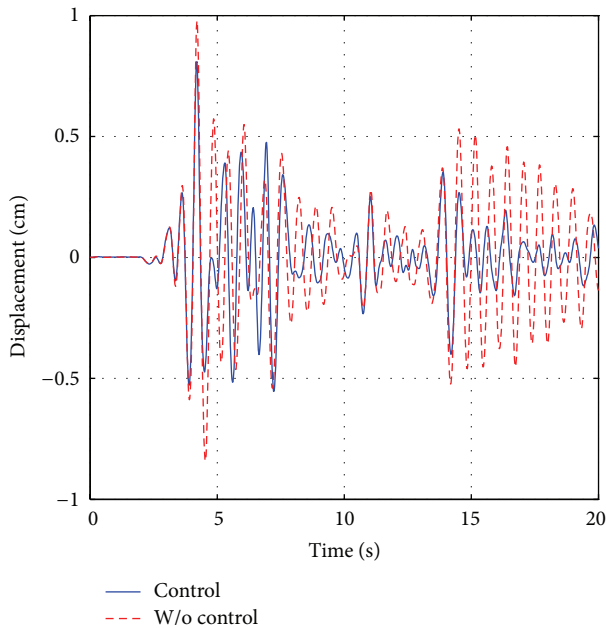


FIGURE 14: Time history of top floor's displacement (EL Centro wave).

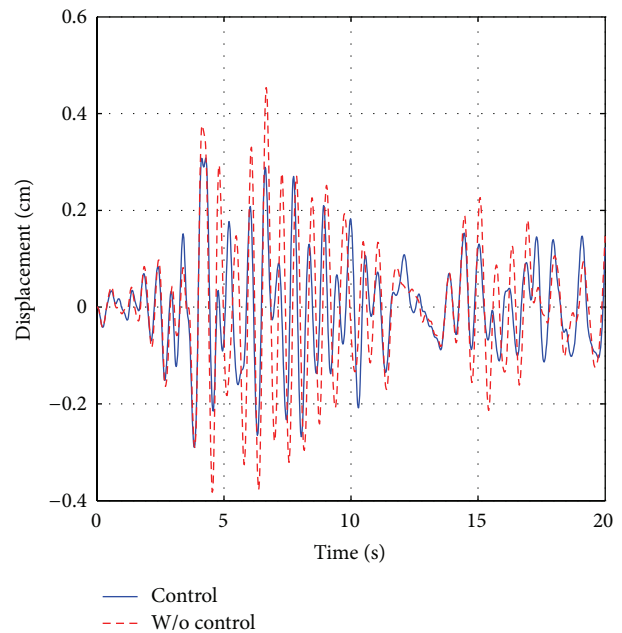


FIGURE 16: Time history of top floor's displacement (Hach wave).

6. Conclusions

The paper proposed a more general and effective method to optimize the parameters of tuned liquid column dampers (TLCD) based on Genetics Algorithm (GA) and H_{∞} norm. The weighted functions are necessary in the optimization process. For the weighted function of earthquake excitation, the square root of the Kanai-Tajimi spectrum is suggested. For the weighted function of output, the first-order function

and second-order one are analyzed with different parameters. The results show that the weighted function of output has great influences on the optimized parameters. To facilitate the parameter optimization, the low-order weighted function of the output is suggested. The structure response with optimized liquid dampers subjected to actual earthquake records is analyzed in the time domain. The results show that TLCD with optimized parameters can effectively reduce

TABLE 4: Reduction ratios of the top story of the structure at different earthquake records.

Earthquake records	Maximum displacements			Maximum accelerations		
	Without control (cm)	TLCD control (cm)	Reduction ratio (%)	Without control (g)	TLCD control (g)	Reduction ratio (%)
Kobe	2.09	1.75	16.27	2.23	1.87	16.14
El Centro	0.98	0.78	20.41	1.02	0.85	16.67
Northridge	1.73	1.52	12.14	1.83	1.60	12.57
Hach	0.48	0.37	22.92	0.48	0.39	18.75

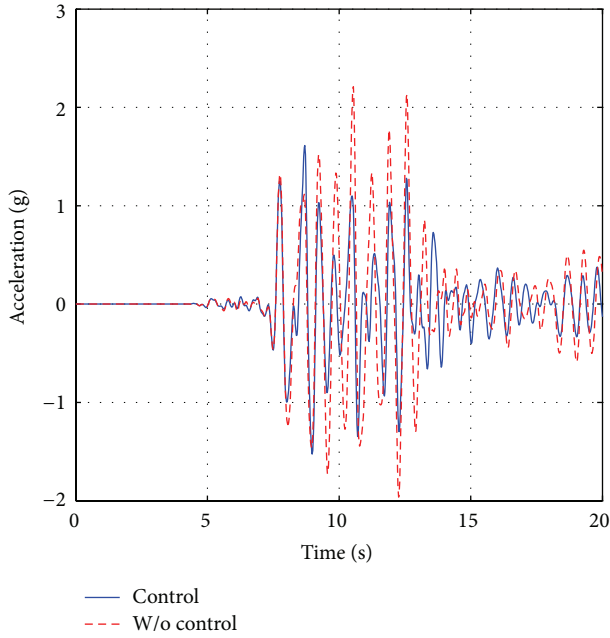


FIGURE 17: Time history of top floor's acceleration (Kobe wave).

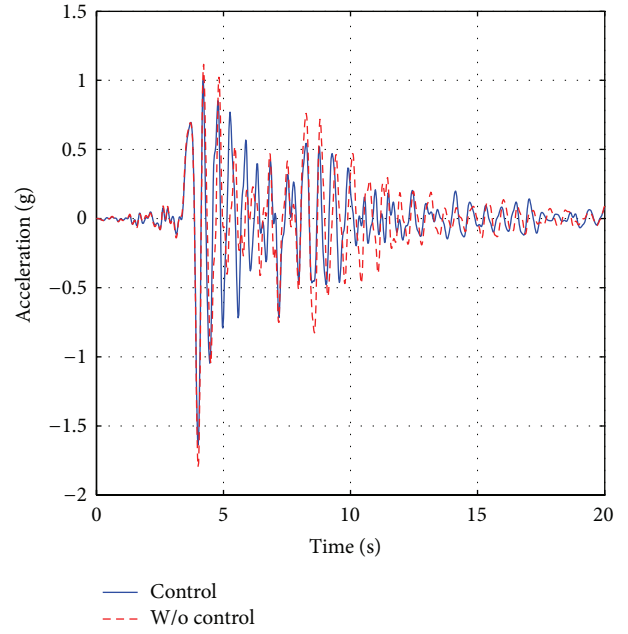


FIGURE 19: Time history of top floor's acceleration (Northridge wave).

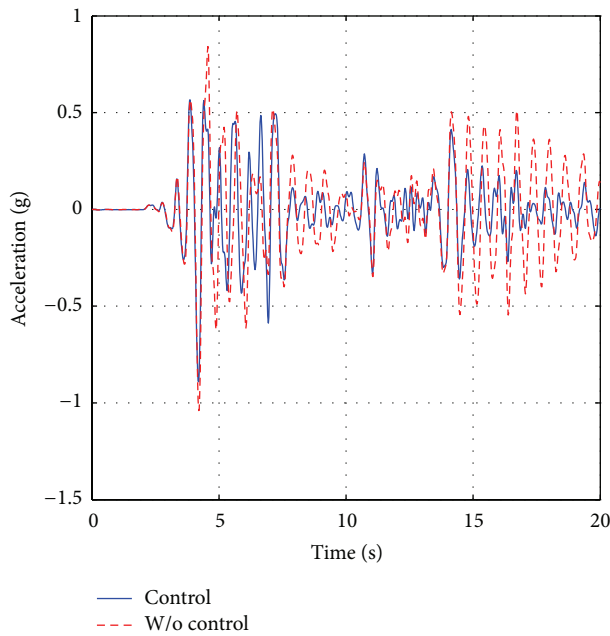


FIGURE 18: Time history of top floor's acceleration (EL Centro wave).

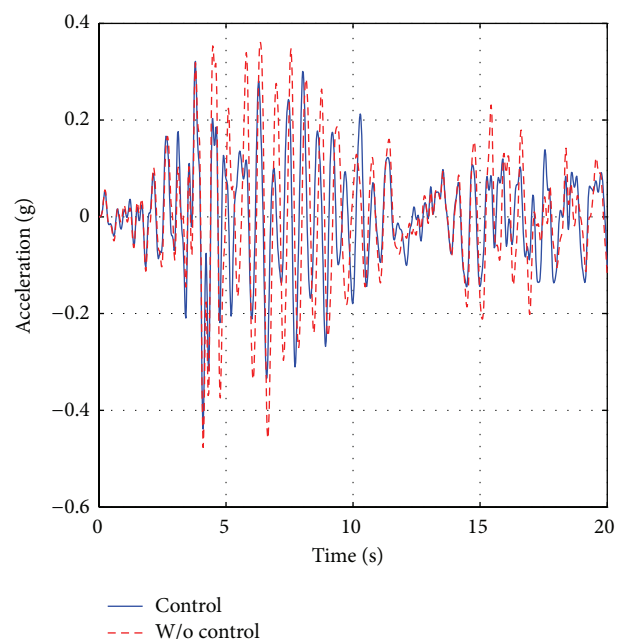


FIGURE 20: Time history of top floor's acceleration (Hach wave).

the seismic responses at different site types, which verify the generality of the proposed optimization method.

Acknowledgment

The authors are grateful for the supports from the National Natural Science Foundation of China (Grant nos. 51261120375 and 51121005).

References

- [1] P. A. Hitchcock, K. C. S. Kwok, R. D. Watkins, and B. Samali, "Characteristics of liquid column vibration absorbers (LCVA)—I," *Engineering Structures*, vol. 19, no. 2, pp. 126–134, 1997.
- [2] P. A. Hitchcock, K. C. S. Kwok, R. D. Watkins, and B. Samali, "Characteristics of liquid column vibration absorbers (LCVA)—II," *Engineering Structures*, vol. 19, no. 2, pp. 135–144, 1997.
- [3] W. L. Qu, Z. Y. Li, and G. Q. Li, "Experimental study on U type water tank for tall buildings and high-rise structures," *China Journal of Building Structures*, vol. 14, no. 5, pp. 37–43, 1993.
- [4] F. Sakai, S. Takaeda, and T. Tamake, "Tuned liquid column damper—new type device for suppression of building vibrations," in *Proceedings of the International Conference on Europe's High-Rise Building*, pp. 926–931, Nanjing, China, 1989.
- [5] H. Gao, K. C. S. Kwok, and B. Samali, "Optimization of tuned liquid column dampers," *Engineering Structures*, vol. 19, no. 6, pp. 476–486, 1997.
- [6] S. Yan, H. N. Li, and G. Lin, "Studies on control parameters of adjustable tuned liquid column damper," *Earthquake Engineering and Engineering Vibration*, vol. 18, no. 4, pp. 96–101, 1998.
- [7] C. C. Chang and C. T. Hsu, "Control performance of liquid column vibration absorbers," *Engineering Structures*, vol. 20, no. 7, pp. 580–586, 1998.
- [8] C. C. Chang, "Mass dampers and their optimal designs for building vibration control," *Engineering Structures*, vol. 21, no. 5, pp. 454–463, 1999.
- [9] S. Yan and H. N. Li, "Performance of vibration control for U type water tank with variable cross section," *Earthquake Engineering and Engineering Vibration*, vol. 19, no. 1, pp. 197–201, 1999.
- [10] H. Gao, K. S. C. Kwok, and B. Samali, "Characteristics of multiple tuned liquid column dampers in suppressing structural vibration," *Engineering Structures*, vol. 21, no. 4, pp. 316–331, 1999.
- [11] N. Gluck, A. M. Reinhorn, J. Gluck, and R. Levy, "Design of supplemental dampers for control of structures," *Journal of Structural Engineering*, vol. 122, no. 12, pp. 1394–1399, 1996.
- [12] C. H. Loh, P. Y. Lin, and N. H. Chung, "Design of dampers for structures based on optimal control theory," *Earthquake Engineering & Structural Dynamics*, vol. 29, no. 9, pp. 1307–1323, 2000.
- [13] A. K. Agrawal and J. N. Yang, "Design of passive energy dissipation systems based on LQR control methods," *Journal of Intelligent Material Systems and Structures*, vol. 10, no. 12, pp. 933–944, 2000.
- [14] A. K. Agrawal and J. N. Yang, "Design of passive energy dissipation systems based on LQR control methods," *Journal of Intelligent Material Systems and Structures*, vol. 10, no. 12, pp. 933–944, 2000.
- [15] J. N. Yang, S. Lin, J.-H. Kim, and A. K. Agrawal, "Optimal design of passive energy dissipation systems based on H_∞ and H₂ performances," *Earthquake Engineering & Structural Dynamics*, vol. 31, no. 4, pp. 921–936, 2002.
- [16] G. Song, P. Qiao, V. Sethi, and A. Prasad, "Active vibration control of a smart pultruded fiber-reinforced polymer I-beam," *Smart Materials and Structures*, vol. 13, no. 4, pp. 819–827, 2004.
- [17] V. Sethi, M. A. Franchek, and G. Song, "Active multimodal vibration suppression of a flexible structure with piezoceramic sensor and actuator by using loop shaping," *Journal of Vibration and Control*, vol. 17, no. 13, pp. 1994–2006, 2011.
- [18] J. L. Meyer, W. B. Harrington, B. N. Agrawal, and G. Song, "Vibration suppression of a spacecraft flexible appendage using smart material," *Smart Materials and Structures*, vol. 7, no. 1, pp. 95–104, 1998.
- [19] V. Sethi and G. Song, "Multimodal vibration control of a flexible structure using piezoceramic sensor and actuator," *Journal of Intelligent Material Systems and Structures*, vol. 19, no. 5, pp. 573–582, 2008.
- [20] H. Gu, G. Song, and H. Malki, "Chattering-free fuzzy adaptive robust sliding-mode vibration control of a smart flexible beam," *Smart Materials and Structures*, vol. 17, no. 3, Article ID 035007, 2008.
- [21] L. Y. Li, G. Song, and J. P. Ou, "Adaptive fuzzy sliding mode based active vibration control of a smart beam with mass uncertainty," *Structural Control & Health Monitoring*, vol. 18, no. 1, pp. 40–52, 2011.
- [22] H. Gu and G. Song, "Active vibration suppression of a composite I-beam using fuzzy positive position control," *Smart Materials and Structures*, vol. 14, no. 4, pp. 540–547, 2005.
- [23] K. Zhou, J. C. Doyle, and K. Glover, *Robust and Optimal Control*, Prentice-Hall, Upper Saddle River, NJ, USA, 1996.

Research Article

A Constitutive Model for Superelastic Shape Memory Alloys Considering the Influence of Strain Rate

Hui Qian,^{1,2} Hongnan Li,¹ Gangbing Song,³ and Wei Guo⁴

¹ School of Civil Engineering, Zhengzhou University, Zhengzhou 450000, China

² Faculty of Infrastructure Engineering, Dalian University of Technology, Dalian 116024, China

³ Department of Mechanical Engineering, University of Houston, Houston, TX 77204-4006, USA

⁴ School of Civil Engineering, Central South University, Changsha, China

Correspondence should be addressed to Hui Qian; qianhui@zzu.edu.cn

Received 9 July 2013; Accepted 7 September 2013

Academic Editor: Jeong-Tae Kim

Copyright © 2013 Hui Qian et al. This is an open access article distributed under the Creative Commons Attribution License, which permits unrestricted use, distribution, and reproduction in any medium, provided the original work is properly cited.

Shape memory alloys (SMAs) are a relatively new class of functional materials, exhibiting special thermomechanical behaviors, such as shape memory effect and superelasticity, which enable their applications in seismic engineering as energy dissipation devices. This paper investigates the properties of superelastic NiTi shape memory alloys, emphasizing the influence of strain rate on superelastic behavior under various strain amplitudes by cyclic tensile tests. A novel constitutive equation based on Graesser and Cozzarelli's model is proposed to describe the strain-rate-dependent hysteretic behavior of superelastic SMAs at different strain levels. A stress variable including the influence of strain rate is introduced into Graesser and Cozzarelli's model. To verify the effectiveness of the proposed constitutive equation, experiments on superelastic NiTi wires with different strain rates and strain levels are conducted. Numerical simulation results based on the proposed constitutive equation and experimental results are in good agreement. The findings in this paper will assist the future design of superelastic SMA-based energy dissipation devices for seismic protection of structures.

1. Introduction

Shape memory alloys (SMAs) are a unique class of materials that have the ability to undergo large deformations, up to 8~10%, that is, at least one order of magnitude greater than common metals and alloys, and revert back to their original and undeformed shape or dimension through either applications of heat, that is, the shape memory effect (SME), or removal of stress, that is, the superelastic effect.

The particular properties of SMAs were first discovered by Chang and Read in 1951; however, it was not until after 1962 when Buechler and his colleagues found the shape memory effect in nickel-titanium (NiTi) at the Naval Ordnance Laboratory that both in-depth research and practical applications emerged. At present, SMAs have been widely implemented in biomedical, aerospace, mechanical, and civil engineering areas [1–5], making it necessary to have a precise understanding of the special mechanical behavior of SMAs in order to fully develop and exploit their potential.

The unique mechanical behaviors of SMAs are made possible by reversible martensitic phase transformation (MPT) induced by temperature or mechanical stress between the austenitic phase (*A*) and martensitic phase (*M*). Austenite has a body-centered cubic crystal structure (crystallographic high symmetry), stable at high temperatures and low stress values, while the martensite has a parallelogram structure (low symmetry), stable at low temperatures and high stress values, having up to 24 variations. In the stress-free state, the material is characterized by four transition temperatures, namely, martensite start temperature M_s , martensite finish temperature M_f , austenite start temperature A_s , and austenite finish temperature A_f . Below the martensite finish temperature, M_f , residual deformations induced by the martensite reorientation due to applied stresses can be recovered by heating the material above the austenite finish temperature, A_f , resulting in the shape memory effect (SME). Above the austenite finish temperature, A_f , martensite is formed associated with forward MPT (from

austenite to detwinned martensite) induced by stress when load exceeds the forward transformation stress; however, the material reverts to austenite at a lower stress without residual deformation associated with inverse MPT (from detwinned martensite to austenite) after unloading, resulting in the superelastic behavior.

Over the past decades, there has been a significant amount of research dedicated to the martensitic phase transformation [6, 7] and the factors that induce the MPT [8–10]. Meanwhile, some constitutive models have been proposed. A short review of the existing models is presented here:

- (1) phenomenological macroscopic constitutive models in terms of stress, strain, and temperature with assumed phase transformation kinetics described by preestablished simple mathematical functions proposed by Tanaka [11], Liang and Rogers [12], Brinson [13], Boyd and Lagoudas [14, 15], Li et al. [16], Tobushi et al. [17], and Sun and Rajapakse [18]; among others.
- (2) one-dimensional polynomial models based on Devonshire's theory with an assumed polynomial-free energy potential, which allows superelasticity and SME description, presented by Falk et al. [19, 20];
- (3) thermodynamic models based on the free energy and dissipation potential developed by Patoor et al. [21], Sun and Hwang [22, 23], Huang and Brinson [24], and Boyd and Lagoudas [25];
- (4) plastic flow models based on dislocation theories of solid state physics proposed by Graesser and Cozzarelli [26, 27], lately improved by Wilde et al. [28], Zhang and Zhu [29], and Ren et al. [30].

For application of SMAs in earthquake engineering, Graesser and Cozzarelli's model [26] will be adopted in this paper due to its advantage of simplicity. Graesser and Cozzarelli's model is capable of capturing both the superelastic effect and the martensitic hysteresis with their subloops due to partial transformation processes. Wilde et al. [28] improve the Graesser and Cozzarelli model by introducing the possibility of describing the material behavior also after phase transformation completion as well as by simulating a smooth transition between the elastic branch and the superelastic plateau. Zhang and Zhu [29] modified Wilde's model to enhance the stability of numerical simulation and speed up the computation time. However, Graesser and Cozzarelli's model and the improved editions cannot describe the strain-rate-dependent property of SMA. To consider the effect of the load path to increase its modeling accuracy, Ren et al. [30] improved Graesser and Cozzarelli's model by dividing the full loop into three parts: the loading branch, unloading branch before the completion of the reverse transformation and the elastic unloading branch after the completion of the reverse transformation, where each part adopts its respective parameters. However, the improved model can only reflect one case of hysteresis for a fixed loading rate, since when the loading rate changes, the model parameters will change. Therefore, it is not convenient to perform continuous simulation of SMA devices under seismic excitations, which involve many different loading rates.

As a further research to improve Graesser and Cozzarelli's model, this paper aims to develop a novel strain-rate-dependent constitutive model, which can simultaneously account for the effects of both strain rates and strain levels. In Section 2 of this paper, Graesser and Cozzarelli's model is improved by adding a stress variable including the influence of strain rate. To verify the effectiveness of the proposed constitutive equation, cyclic tensile tests on superelastic NiTi wires with different strain rates and strain levels are carried out, as described in Section 3, and the experimental results and analysis are given in Section 4. In Section 5, numerical simulations are conducted to demonstrate the accuracy of the improved Graesser and Cozzarelli's model.

2. Constitutive Model of Shape Memory Alloys

In this section, a uniaxial constitutive model, based on Graesser and Cozzarelli's model, is developed to capture the strain-rate-dependent property of superelastic SMA materials.

2.1. Graesser and Cozzarelli's Model. Based on Ozdemir's model [30], Graesser and Cozzarelli proposed a one-dimensional hysteretic model that produced the general macroscopic stress-strain characteristics of SMAs [26]. The equation is given as

$$\dot{\sigma} = E \left[\dot{\varepsilon} - |\dot{\varepsilon}| \left(\frac{\sigma - \beta}{Y} \right)^n \right], \quad (1)$$

where σ is the one-dimensional stress, ε is the strain, E is the elastic modulus, Y is the transformation stress, n is a constant assumed to be any positive odd real value controlling the sharpness of the transition from the elastic state to the phase transformation, $\dot{\sigma}$ and $\dot{\varepsilon}$, respectively, denote the ordinary time derivative of the stress and strain, and β is the one-dimensional back stress, given by

$$\beta = E\alpha \{ \varepsilon_{\text{in}} + f_T |\varepsilon|^c \operatorname{erf}(a\varepsilon) [u(-\varepsilon\dot{\varepsilon})] \}, \quad (2)$$

where f_T , a , and c are material constants controlling the type and size of the hysteresis, the amount of elastic recovery during unloading, and the slope of the unloading stress plateau, respectively. α is a constant controlling the slope of the σ - ε curve in the inelastic range, given by

$$\alpha = \frac{E_y}{E - E_y}, \quad (3)$$

where E_y is the slope of the σ - ε curve in the inelastic range. ε_{in} is the inelastic strain, given by

$$\varepsilon_{\text{in}} = \varepsilon - \frac{\sigma}{E}. \quad (4)$$

$u(x)$ is the unit step function defined as

$$u(x) = \begin{cases} +1 & x \geq 0 \\ 0 & x < 0. \end{cases} \quad (5)$$

$\text{erf}(x)$ is the error function defined by

$$\text{erf}(x) = \frac{2}{\sqrt{\pi}} \int_0^x e^{-t^2} dt. \quad (6)$$

Graesser and Cozzarelli's model has a relatively simple expression with parameters that can be easily acquired and it is easy to implement, yet this model can still be improved. Though the equations are written in differential form, the model is essentially strain rate independent. Studies [8–10] show that the properties are strongly dependent on the strain rate. In this paper, Graesser and Cozzarelli's model will be improved to consider the influence of strain rate.

2.2. Improved Graesser and Cozzarelli's Model. To simulate the strain-rate-dependent hysteretic behavior of superelastic SMAs, Graesser and Cozzarelli's model will be improved. The following assumptions are made for this purpose.

- (i) The ambient temperature is constant.
- (ii) The effect of strain rate on the properties of SMAs can be ignored when it is below $\dot{\epsilon}_0$ ($\dot{\epsilon}_0 = 1.0 \times 10^{-4}/\text{s}$ in this paper).

Based on the above assumptions, the stress is formulated here. The stress under dynamic loading can be separated into two parts; namely,

$$\sigma = \sigma_s + \sigma_k, \quad (7)$$

where σ , σ_s , and σ_k are the stress under dynamic loading, the stress under quasistatic loading, and the stress change due to the influence of the strain rate, respectively. To keep consistency with σ and σ_s in symbol style, σ_k is used to represent the stress change. Actually, the value of σ_k is equal to that of $\Delta\sigma$ which will be illustrated in Section 4.

Differentiating (7) results in

$$\dot{\sigma} = \dot{\sigma}_s + \dot{\sigma}_k, \quad (8)$$

where

$$\dot{\sigma}_s = E \left[\dot{\epsilon} - |\dot{\epsilon}| \left| \frac{\sigma_s - \beta}{Y} \right|^{n-1} \left(\frac{\sigma_s - \beta}{Y} \right) \right]. \quad (9)$$

The parameters in (9) have already been defined in Section 2.1 and can be obtained experimentally by the stress-strain curve under quasistatic loading.

The definition of σ_k depends on the relationship between $\dot{\epsilon}$ and $\dot{\epsilon}_0$. The equations capturing the relationship between σ_k and $\dot{\epsilon}$, ϵ as well as $\dot{\epsilon}_0$ can be presented from the experimental tests (presented in Sections 3 and 4) based on mathematical statistics and numerical fitting method. σ_k is given as follows.

- (1) For $-\dot{\epsilon}_0 \leq \dot{\epsilon} \leq \dot{\epsilon}_0$,

$$\sigma_k = 0. \quad (10)$$

- (2) For $\dot{\epsilon} > \dot{\epsilon}_0$,

$$\sigma_k = p \ln \left(\frac{\dot{\epsilon}}{\dot{\epsilon}_0} \right) \sqrt{\epsilon} = p (\ln \dot{\epsilon} - \ln \dot{\epsilon}_0) \sqrt{\epsilon}, \quad (11)$$

where p is a material constant. If $R = -\ln(\dot{\epsilon}_0)$, then

$$\sigma_k = p (\ln \dot{\epsilon} + R) \sqrt{\epsilon}. \quad (12)$$

Differentiating (12) results in

$$\dot{\sigma}_k = p \left[(\ln \dot{\epsilon} + R) \frac{\dot{\epsilon}}{2\sqrt{\epsilon}} + \frac{\ddot{\epsilon}}{\dot{\epsilon}} \sqrt{\epsilon} \right]. \quad (13)$$

- (3) For $\dot{\epsilon} < -\dot{\epsilon}_0$,

$$\sigma_k = q \ln \left(\frac{|\dot{\epsilon}|}{\dot{\epsilon}_0} \right) \epsilon^2 = q (\ln |\dot{\epsilon}| - \ln \dot{\epsilon}_0) \epsilon^2 \quad (14)$$

$$= q (\ln |\dot{\epsilon}| + R) \epsilon^2.$$

Thus, its time derivative can be written as

$$\dot{\sigma}_k = q \left[2 (\ln |\dot{\epsilon}| + R) |\dot{\epsilon}| \epsilon + \frac{\ddot{\epsilon}}{|\dot{\epsilon}|} \epsilon^2 \right], \quad (15)$$

where q is a material parameter related to the maximum strain amplitude, ϵ_{\max} . Other unnoted parameters have already been defined.

3. Experimental Setup for Tensile Testing of Superelastic SMA Wires

In the following, cyclic tensile tests on superelastic NiTi wires with different strain rates and strain levels are carried out to verify the effectiveness of the proposed constitutive equation.

3.1. Test Specimens and Equipment. The NiTi SMA wires used for testing have a diameter of 0.5 mm. The TiNi SMA is an alloy with approximate 50.9% Ni and 49.1% Ti. Under zero external stress, the martensite start and finish temperatures and the austenite start and finish temperatures (M_f , M_s , A_s , and A_f), measured by DSC (differential scanning calorimeter), are -73°C , -55°C , -23°C , and 5°C , respectively.

Tests were conducted using an electromechanical universal testing machine. The SMA wire specimens, with a 100 mm test length between the two custom-made grips, were subjected to triangular cyclic loading under different strain amplitudes. In order to acquire reliable hysteresis behavior of SMA, three specimens were applied in each testing. The mean values were utilized for analysis. The strains were calculated from the elongation measured by a 50 mm gage length extensometer with the stress calculated from the axial force, which was measured by a 10 kN load cell. In each test, the specimen was required to follow a triangular wave with a constant strain rate. The data was recorded automatically by a PC-based data acquisition system with a 30 Hz sampling rate. All the tests were carried out at room temperature ($\approx 25^\circ\text{C}$). The experimental setup and strain loading curve are shown in Figures 1(a) and 1(b), respectively.

3.2. Test Procedure. The experimental results in references [8, 9] have shown the mechanical behaviors of the SMA trend

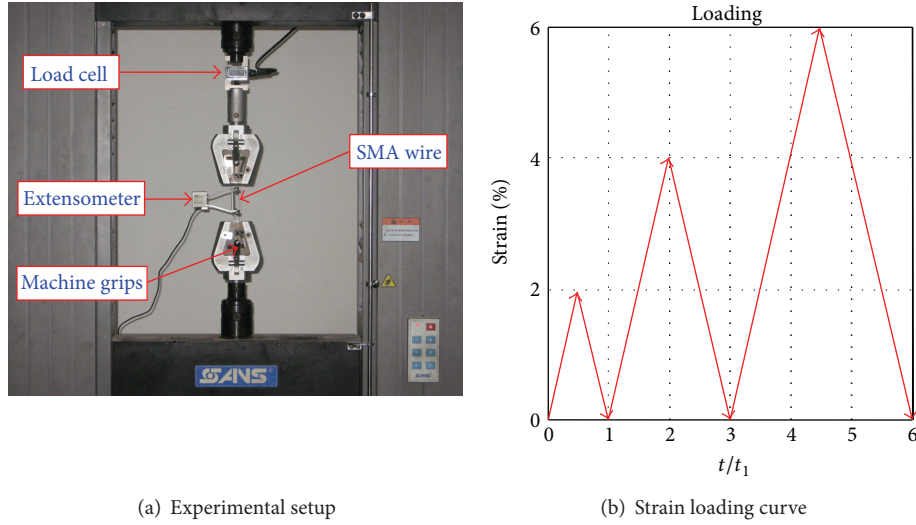


FIGURE 1: Experimental setup and strain loading curve for mechanical testing of SMA wires.

stable with the increasing of the cyclic number. Therefore, prior to testing, the NiTi SMA specimens were cycled 30 times at 6.5% strain amplitude and $1.0 \times 10^{-3}/s$ strain rate as a “training” process to reach a steady-state condition. The scheme of the tests is described as follows.

- (1) At quasistatic loading ($1.0 \times 10^{-4}/s$ strain rate), the NiTi SMA specimens are subjected to cyclic loading with different strain levels, ranging from 2% to 6% at an increment of 2%.
- (2) At strain rates of $5.0 \times 10^{-4}/s$, $1.0 \times 10^{-3}/s$, $2.5 \times 10^{-3}/s$, and $5.0 \times 10^{-3}/s$, the NiTi SMA specimens are subjected to cyclic loading with different strain levels, ranging from 2% to 6% at an increment of 2%.

What needs to be pointed out is that the maximum strain rate is only $5.0 \times 10^{-3}/s$ due to the limitation of the experimental condition. The range is relatively low in seismic engineering. More tests with higher strain rates will be conducted in the future.

4. Results and Analysis

Many experimental studies have shown that the superelastic behavior of SMAs strongly depends on the loading rate [8–10]; however, few quantitative relationships are provided [16–18]. In this section, a stress change variable, $\Delta\sigma$, which is a relative quantity between the dynamic loading condition and the static loading condition at an identical strain, is introduced to evaluate the effect of the strain rate on the superelastic behavior of SMAs.

4.1. Variation of Stress during Forward Martensitic Transformation at Different Strain Rates. Figure 2(a) shows the relationship between the amount of stress change, $\Delta\sigma$, and the strain obtained by the tests during the forward martensitic transformation at different strain rates. The points with different shapes represent the experimental results. As we

can see, $\Delta\sigma$ increases with an increase of strain. The rate of increase of $\Delta\sigma$ is relatively large at small strain levels; however it decreases with an increasing strain. Moreover, the stress change $\Delta\sigma$ increases with an increasing strain rate.

On one hand, for a fixed strain rate, the relationship between stress change $\Delta\sigma$ and strain level ε can be described using a power function with the index less than 1. In order to simplify the equation, the index selected is 1/2. On the other hand, for a fixed strain level, the relationship between stress change $\Delta\sigma$ and strain rate $\dot{\varepsilon}$ can be captured by natural logarithms function. Therefore, based on numerical fitting tools, the stress change $\Delta\sigma$, as a function of the strain level and the strain rate during the forward martensitic transformation, can be expressed by the following equation:

$$\Delta\sigma = 159.6 (\ln \dot{\varepsilon} + 9.21) \sqrt{\varepsilon}, \quad (16)$$

where ε is the strain and $\dot{\varepsilon}$ is the strain rate. The fitted curves calculated from (16) for different strain rates are shown in Figure 2(a). As seen from (16), the material constant p in (12) is equal to 159.6.

4.2. Variation of Stress during Inverse Martensitic Transformation at Different Strain Rates. Figure 2(b) shows the relationship between the amount of stress change $\Delta\sigma$ and the strain during the inverse martensitic transformation at different strain rates with the maximum strain amplitude at 6%. Likewise, the points with different shapes represent the experimental results. As opposed to the forward martensitic transformation, the rate of increase in $\Delta\sigma$ is relatively small at small strain levels; however it increases with an increasing strain. Moreover, the stress change $\Delta\sigma$ increases with an increasing strain rate. This is because the stress-strain loops of superelastic SMA translate upwards, while the branches of the curve relevant to the phase transformations harden with the increasing of strain rate, as noted in references [8, 10].

Similarly, for a given strain rate, the relationship between stress change $\Delta\sigma$ and strain level ε can be described using

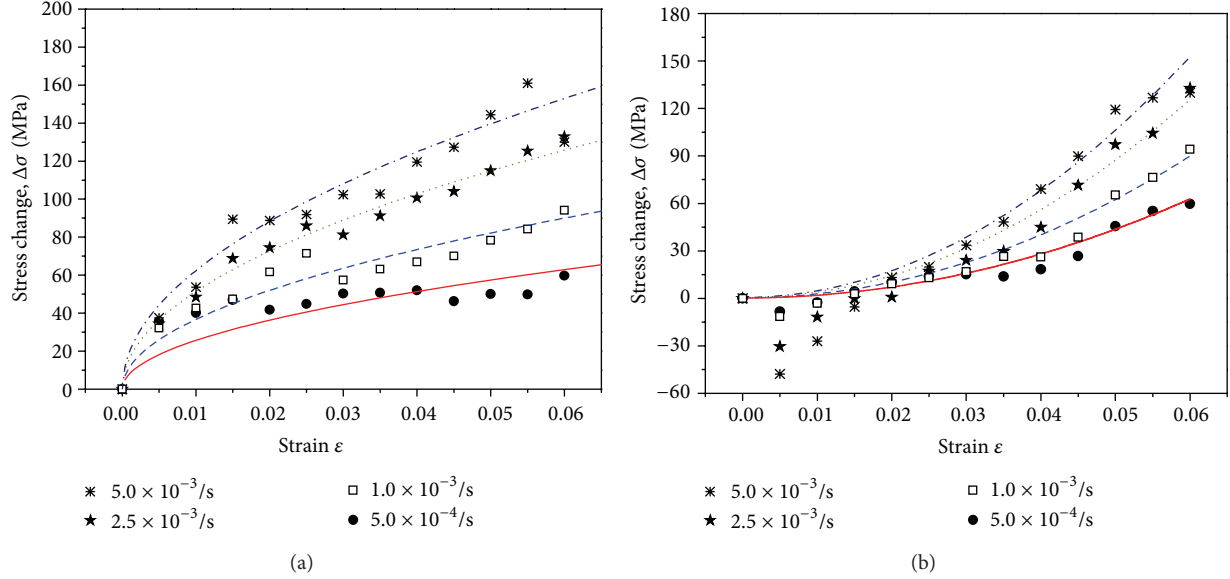


FIGURE 2: Relationship between stress change and strain during. Experimental data is marked with points. The simulation of the proposed equation with the lines. (a) Forward phase transformation. (b) Inverse phase transformation.

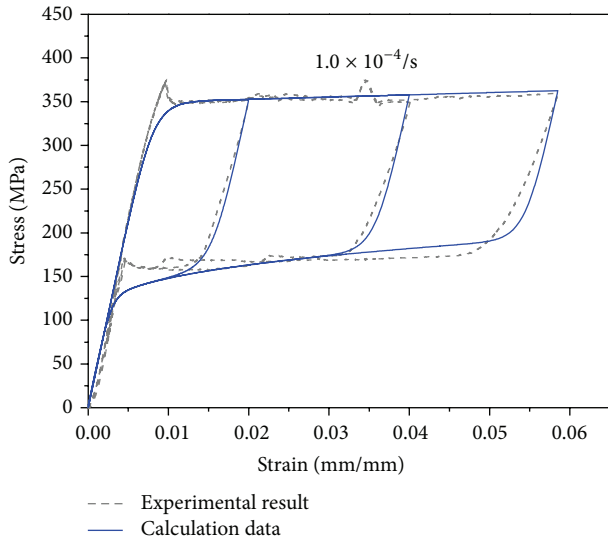


FIGURE 3: Comparison of SMA stress-strain curve between numerical and experimental results under quasistatic loading.

a power function with the index more than 1. The index selected is 2. The relationship between stress change $\Delta\sigma$ and strain rate $\dot{\epsilon}$ is similar to that during the forward martensitic transformation. In the case of the maximum strain amplitude 6%, the stress change, $\Delta\sigma$, as a function of the strain level and the strain rate during the inverse martensitic transformation, can be expressed by the following equation:

$$\Delta\sigma = -500 (\ln |\dot{\epsilon}| + 9.21) \epsilon^2. \quad (17)$$

The fitted curves calculated from (17) for different strain rates are also shown in Figure 2(b). As seen from (17), the material constant q in (14) is equal to 500 for the strain level at 6%.

5. Numerical Simulations

In this section, the effectiveness of the improved model to reproduce the rate-dependent superelastic behavior of SMAs wire is validated by comparing numerical results with experimental data. In order to verify suitability of the model, two different conditions, static loading and dynamic loading, are investigated.

5.1. Comparison of Model Predictions and Experimental Data under Quasistatic Loading. Figure 3 shows the comparison of the model predictions and the experimental responses of the SMA wire at 2%, 4%, and 6% strain levels under quasistatic loading with a strain rate of $1.0 \times 10^{-4}/s$. The key parameters used in the models are $E = 43000$ MPa, $Y = 350$ N, $\alpha = 0.006$, $f_T = 2.3$, $c = 0.04$, $a = 400$, and $n = 6$. As can be seen from Figure 3, the numerical curves predicted by the improved model agree well with the experimental data.

To make an additional quantitative observation, comparisons of the energy dissipation per cycle, tensile stress at peak strain, and equivalent viscous damping between the experimental data and numerical results are shown in Table 1. Note that the maximum differences for energy dissipation per cycle, tensile stress at peak strain, and equivalent viscous damping are 2.9%, 1.8%, and 2.6%, respectively. Therefore, the results indicate that the mechanical behavior of superelastic SMA wire under quasistatic loading was predicted well by the improved model.

5.2. Comparison of Model Predictions and Experimental Data under Dynamic Loading. Figure 4 shows the comparison of model predictions and experimental responses of the SMA wire at 4% strain under the strain rates of $5.0 \times 10^{-4}/s$, $1.0 \times 10^{-3}/s$, $2.5 \times 10^{-3}/s$, and $5.0 \times 10^{-3}/s$, respectively. The key

TABLE 1: Comparisons of model predictions and experimental data for varying peak strains: constant strain rate.

Peak strain (m/m)	Energy dissipation per cycle (MJ/m ³ /cycle)			Tensile stress at peak strain (GPa)			Equivalent viscous damping (%)		
	Experimental data	Numerical results	Difference	Experimental data	Numerical results	Difference	Experimental data	Numerical results	Difference
2.0%	2.20	2.25	2.13%	354.21	352.69	-0.43%	4.95	5.08	2.57%
4.0%	5.84	5.95	1.89%	351.20	357.82	1.88%	6.62	6.63	0.45%
5.85%	8.91	9.17	2.91%	359.32	362.57	0.91%	6.75	6.88	1.98%

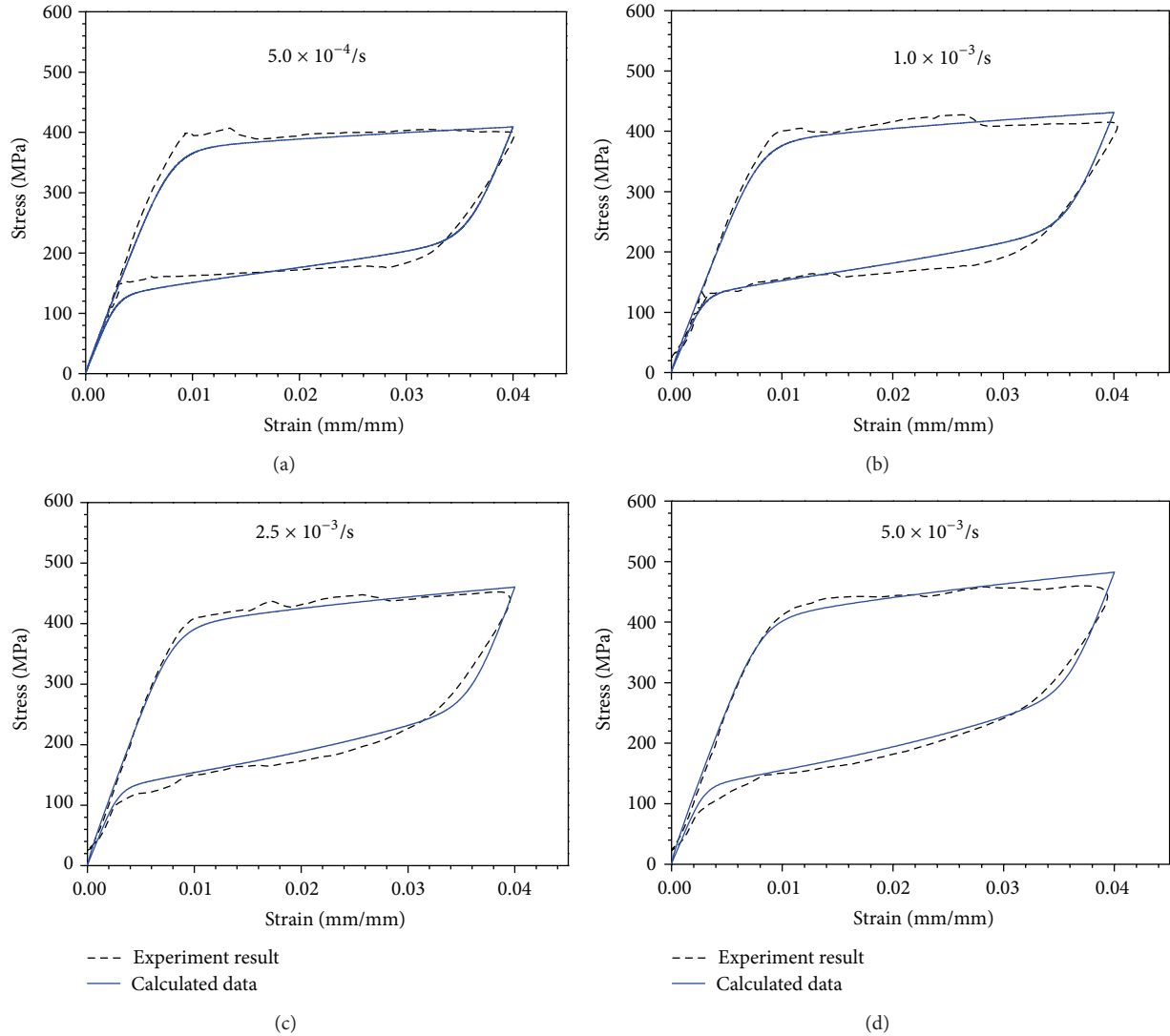


FIGURE 4: Comparison of calculated stress-strain curves based on improved Graesser and Cozzarelli's model and experiment data for varying loading rates.

parameters used in the models are $E = 43000$ MPa, $Y = 350$ N, $\alpha = 0.006$, $f_T = 2.3$, $c = 0.04$, $a = 400$, and $n = 6$, $R = 9.21$, $p = 159.6$, and $q = -500$. It is obvious from Figures 4(a)–4(d) that the superelastic behavior at different strain rates is well predicted by the improved constitutive model.

Table 2 shows the comparisons of the energy dissipation per cycle, the tensile stress at peak strain, and the equivalent viscous damping between the experimental data and numerical results. It is clear that the maximum difference of energy dissipation per cycle, the tensile stress at peak strain, and the equivalent viscous damping are 6.89%, 4.01%, and

TABLE 2: Comparisons of the model predictions and experiments for varying loading rates: fixed peak strain.

Strain rate (m/m/s)	Energy dissipation per cycle (MJ/m ³ /cycle)			Tensile stress at peak strain (GPa)			Equivalent viscous damping (%)		
	Experimental data	Numerical results	Difference	Experimental data	Numerical results	Difference	Experimental data	Numerical results	Difference
5.0×10^{-4}	6.99	6.64	4.93%	400.5	409.07	-2.14%	6.94	6.46	6.93%
1.0×10^{-3}	7.45	6.94	6.89%	414.5	431.14	-4.01%	7.16	6.41	9.36%
2.5×10^{-3}	7.70	7.33	4.88%	453.8	460.32	-1.44%	6.84	6.34	7.39%
5.0×10^{-3}	7.75	7.62	1.60%	464.2	482.39	-3.92%	6.75	6.29	6.74%

9.36%, respectively. From both Figure 4 and Table 2, it can be concluded that the improved Graesser and Cozzarelli's model is able to capture the superelastic behavior in dynamic loading conditions within the range of rates tested in this study.

6. Conclusions

In this paper, the influence of the strain rate on the mechanical properties of SMAs is investigated. A one-dimensional strain-rate-dependent constitutive model based on Graesser and Cozzarelli's model is proposed to predict the hysteretic behavior of superelastic SMAs. In this model, the stress is divided into two parts: the static stress and dynamic stress change. The former is based on the original Graesser and Cozzarelli's model and describes the property under quasistatic loading. The latter one considers the effect of the strain rate. Comparisons of model predictions and experimental results at different strain levels and strain rates are performed and reveal that the improved Graesser and Cozzarelli's model can accurately predict hysteretic behavior of superelastic SMAs under both static and dynamic loading conditions within the range of rates tested in this study. In this paper, the maximum strain rate is only 5.0×10^{-3} /s due to the limitation of the experimental condition. The range is relatively low in seismic engineering. Future research will be conducted at higher strain rates to further validate the effectiveness of the model.

Acknowledgments

The research reported in this paper was supported by the National Natural Science Foundation of China (no. 51108426), China Postdoctoral Science Foundation (no. 20100471008), and Research Found for the Doctoral Program of Higher Education of China (no. 20104101120009). These supports are greatly appreciated.

References

- [1] S. Saadat, J. Salichs, M. Noori et al., "An overview of vibration and seismic applications of NiTi shape memory alloy," *Smart Materials and Structures*, vol. 11, no. 2, pp. 218–229, 2002.
- [2] G. Song, N. Ma, and H.-N. Li, "Review of applications of shape memory alloys in civil structures," in *Proceedings of the Earth and Space Conference (ASCE '04)*, pp. 559–566, March 2004.
- [3] L. Janke, C. Czaderski, M. Motavalli, and J. Ruth, "Applications of shape memory alloys in civil engineering structures—overview, limits and new ideas," *Materials and Structures*, vol. 38, no. 279, pp. 578–592, 2005.
- [4] H. N. Li and L. S. Huo, "Advances in structural control in civil engineering in China," *Mathematical Problems in Engineering*, vol. 2010, Article ID 936081, 23 pages, 2010.
- [5] R. Johnson, J. E. Padgett, M. E. Maragakis, R. Desroches, and M. S. Saiidi, "Large scale testing of nitinol shape memory alloy devices for retrofitting of bridges," *Smart Materials and Structures*, vol. 17, no. 3, Article ID 035018, 13 pages, 2008.
- [6] M. S. Alam, M. A. Youssef, and M. Nehdi, "Utilizing shape memory alloys to enhance the performance and safety of civil infrastructure: A review," *Canadian Journal of Civil Engineering*, vol. 34, no. 9, pp. 1075–1086, 2007.
- [7] K. L. Ng and Q. P. Sun, "Stress-induced phase transformation and detwinning in NiTi polycrystalline shape memory alloy tubes," *Mechanics of Materials*, vol. 38, no. 1-2, pp. 41–56, 2006.
- [8] M. Dolce and D. Cardone, "Mechanical behaviour of shape memory alloys for seismic applications 2. Austenite NiTi wires subjected to tension," *International Journal of Mechanical Sciences*, vol. 43, no. 11, pp. 2657–2677, 2001.
- [9] R. Desroches, J. McCormick, and M. Delemont, "Cyclic properties of superelastic shape memory alloy wires and bars," *Journal of Structural Engineering*, vol. 130, no. 1, pp. 38–46, 2004.
- [10] D. Wolons, F. Gandhi, and B. Malovrh, "Experimental investigation of the pseudoelastic hysteresis damping characteristics of shape memory alloy wires," *Journal of Intelligent Material Systems and Structures*, vol. 9, no. 2, pp. 116–126, 1998.
- [11] K. Tanaka, "A thermomechanical sketch of shape memory effect: one-dimensional tensile behavior," *Res Mechanica*, vol. 18, no. 3, pp. 251–263, 1986.
- [12] C. Liang and C. A. Rogers, "One-dimensional thermomechanical constitutive relations for shape memory materials," *Journal of Intelligent Material Systems and Structures*, vol. 1, no. 2, pp. 207–234, 1990.
- [13] L. C. Brinson, "One-dimensional constitutive behavior of shape memory alloys: thermomechanical derivation with non-constant material functions and redefined martensite internal variable," *Journal of Intelligent Material Systems and Structures*, vol. 4, no. 2, pp. 229–242, 1993.
- [14] J. G. Boyd and D. C. Lagoudas, "A thermodynamical constitutive model for shape memory materials. Part I. The monolithic shape memory alloy," *International Journal of Plasticity*, vol. 12, no. 6, pp. 805–842, 1996.
- [15] J. G. Boyd and D. C. Lagoudas, "A thermodynamical constitutive model for shape memory materials. Part II. The SMA composite material," *International Journal of Plasticity*, vol. 12, no. 7, pp. 843–873, 1996.

- [16] H. Li, C.-X. Mao, and J.-P. Ou, "Strain self-sensing property and strain rate dependent constitutive model of austenitic shape memory alloy: experiment and theory," *Journal of Materials in Civil Engineering*, vol. 17, no. 6, pp. 676–685, 2005.
- [17] H. Tobushi, I. Shimeno, T. Hachisuka, and K. Tanaka, "Influence of strain rate on superelastic behaviour of TiNi shape memory alloy," *Proceedings of the Institution of Mechanical Engineers Part L: Journal of Materials: Design and Applications*, vol. 213, no. 2, pp. 93–102, 1999.
- [18] S. Sun and R. K. N. D. Rajapakse, "Simulation of pseudoelastic behaviour of SMA under cyclic loading," *Computational Materials Science*, vol. 28, no. 3-4, pp. 663–674, 2003.
- [19] F. Falk, "Model free energy, mechanics, and thermodynamics of shape memory alloys," *Acta Metallurgica*, vol. 28, no. 12, pp. 1773–1780, 1980.
- [20] F. Falk and P. Konopka, "Three-dimensional Landau theory describing the martensitic phase transformation of shape-memory alloys," *Journal of Physics*, vol. 2, no. 1, pp. 61–77, 1990.
- [21] E. Patoor, A. Eberhardt, and M. Berveiller, "Thermomechanical behavior of shape memory alloys," *Archives of Mechanics*, vol. 40, pp. 775–794, 1988.
- [22] Q. P. Sun and K. C. Hwang, "Micromechanics modelling for the constitutive behavior of polycrystalline shape memory alloys—I. Derivation of general relations," *Journal of the Mechanics and Physics of Solids*, vol. 41, no. 1, pp. 1–17, 1993.
- [23] Q. P. Sun and K. C. Hwang, "Micromechanics modelling for the constitutive behavior of polycrystalline shape memory alloys—II. Study of the individual phenomena," *Journal of the Mechanics and Physics of Solids*, vol. 41, no. 1, pp. 19–33, 1993.
- [24] M. S. Huang and L. C. Brinson, "A multivariant model for single crystal shape memory alloy behavior," *Journal of the Mechanics and Physics of Solids*, vol. 46, no. 8, pp. 1379–1409, 1998.
- [25] J. G. Boyd and D. C. Lagoudas, "A thermodynamical constitutive model for the shape memory effect due to transformation and reorientation," in *Smart Structures and Materials*, vol. 2189 of *Proceedings of SPIE*, pp. 276–288, 1994.
- [26] E. J. Graesser and F. A. Cozzarelli, "Shape-memory alloys as new materials for aseismic isolation," *Journal of Engineering Mechanics*, vol. 117, no. 11, pp. 2590–2608, 1991.
- [27] E. J. Graesser and F. A. Cozzarelli, "Proposed three-dimensional constitutive model for shape memory alloys," *Journal of Intelligent Material Systems and Structures*, vol. 5, no. 1, pp. 78–89, 1994.
- [28] K. Wilde, P. Gardoni, and Y. Fujino, "Base isolation system with shape memory alloy device for elevated highway bridges," *Engineering Structures*, vol. 22, no. 3, pp. 222–229, 2000.
- [29] Y. Zhang and S. Zhu, "A shape memory alloy-based reusable hysteretic damper for seismic hazard mitigation," *Smart Materials and Structures*, vol. 16, no. 5, pp. 1603–1613, 2007.
- [30] W. J. Ren, H. N. Li, and G. Song, "A one-dimensional strain-rate-dependent constitutive model for superelastic shape memory alloys," *Smart Materials and Structures*, vol. 16, no. 1, pp. 191–197, 2007.

Research Article

Study on Seismic Control of Power Transmission Tower-Line Coupled System under Multicomponent Excitations

Li Tian, Qiqi Yu, and Ruisheng Ma

School of Civil and Hydraulic Engineering, Shandong University, No. 17922 Jingshi Road, Lixia District, Jinan, Shandong 250061, China

Correspondence should be addressed to Li Tian; tianli@sdu.edu.cn

Received 29 July 2013; Accepted 27 August 2013

Academic Editor: Hong-Nan Li

Copyright © 2013 Li Tian et al. This is an open access article distributed under the Creative Commons Attribution License, which permits unrestricted use, distribution, and reproduction in any medium, provided the original work is properly cited.

The seismic control of power transmission tower-line coupled system subjected to multicomponent excitations is studied in this paper. The schematic of tuned mass damper is introduced, and equations of motion of a system with tuned mass damper under multi-component excitations are proposed. Three-dimensional finite tower-line system models are created based on practical engineering in studying the response of this system without and with control. The time domain analysis takes into account geometric nonlinearity due to finite deformation. The optimal design of the transmission tower-line system with tuned mass damper is obtained according to different mass ratio. The effects of wave travel, coherency loss, and different site conditions on the system without and with control are investigated, respectively.

1. Introduction

Power transmission tower-line system is an important facility of a power system. Its failure may lead to the outage of power supply [1]. The transmission tower is usually designed by static load, impulsive load, wind loads, ice load, and so forth. However, most transmission lines need cross high seismic intensity zone in China, and many towers and lines were damaged in past earthquakes. In the 1976 Tangshan earthquake, some towers were collapsed [2]. During the 1995 Kobe earthquake, 38 transmission lines were damaged, and 20 towers were tilted as a result of foundation settlement [3]. During the 1999 Chi-Chi earthquake, many lines were broken, and some towers collapsed [4]. In the 2008 Wenchuan earthquake, Sichuan electric network was damaged seriously [5]. Electric systems were damaged during the 2013 Yaan earthquake in China. Some pictures of damaged towers and lines are shown in Figure 1.

A few foreign and domestic researchers have studied the vibration control of transmission tower-line system in recent years. Battista et al. [6] envisaged nonlinear pendulum-like damper (NLPD) installed on the tower in order to reduce the displacement at the top of tower, and the efficiency of

nonlinear pendulum-like damper was demonstrated. Huang and Tang [7] researched the vibration control effect of tuned liquid damper (TLD) based on large span transmission tower. Chen and Tang [8] investigated the vibration control effect of the multiple tuned mass dampers (MTMD) and viscoelastic damper (VED) under wind excitation based on Jiangyin Yangtze River 500 kV long span transmission line. Deng et al. [9] studied wind vibration control experiment based on 500 kV Jiangyin large span tower and verified the design program of tuned mass damper (TMD) and viscoelastic dissipater (VED). Liu and Li [10] presented a method to simulate tuned mass damper (TMD) and analyzed the control of wind-induced dynamic response for transmission tower-line system. In all these studies, the vibration controls of transmission towers under wind excitation were carried out, but the research about earthquake control of transmission tower-line system is very little.

To date, the seismic control of power transmission tower-line system under multicomponent excitations has not been investigated. In this paper, the schematic of TMD is introduced, and equations of motion of a system with TMD under seismic excitation are proposed. Three-dimensional finite tower-line system models are considered in studying

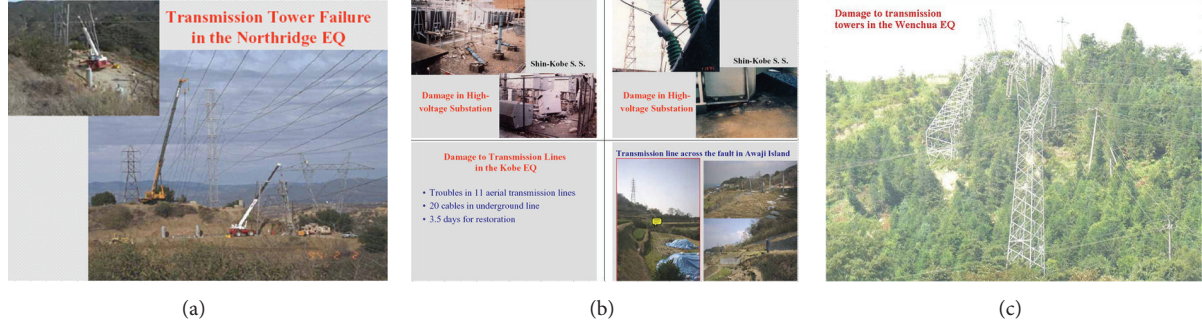


FIGURE 1: Damage to transmission tower-line system in the earthquake.

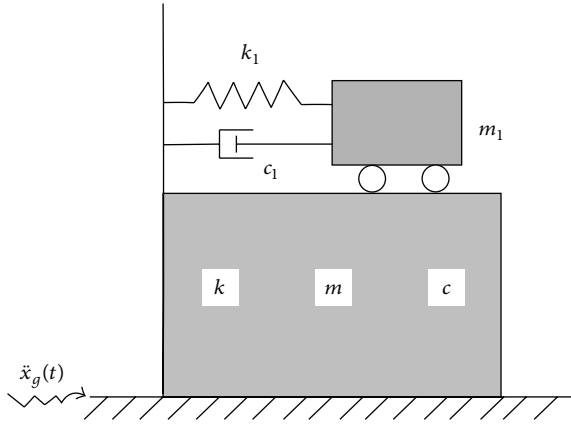


FIGURE 2: Schematic structure with tuned mass damper.

the response of this system without and with control. The transmission towers are modeled by beam elements, while the transmission line is modeled by cable elements that account for the nonlinear geometry of the transmission lines. The time domain analysis takes into account geometric nonlinearity due to finite deformation. The optimal design of the transmission tower-line system with TMD is obtained according to different mass ratio. The transmission tower-line system is the difference among the ground motion components affecting various support points of the structure. The parameters studied include the effect of wave passage, coherency loss, and different local site.

2. Equations of Motion of a System with TMD

2.1. Schematic of TMD. A tuned mass damper (TMD) is a dynamic absorber consisting of a mass, spring, and damping [11]. If the structure is simplified as a single-degree-of-freedom system, the reducing vibration calculation model of the structure with TMD system is shown in Figure 2. Tuned mass damper-structure reducing vibration system is that the tuned mass damper install in the structure.

The equation of motion of tuned mass damper can be written as

$$m_1 \ddot{x}_1 + c_1 \dot{x}_1 + k_1 x_1 = -m_1 \ddot{x} - m_1 \ddot{x}_g(t), \quad (1)$$

where x_1 is the displacement of tuned mass damper, x is the displacement of structure, m_1 , c_1 , and k_1 are the mass, damping, and stiffness of tuned mass damper, respectively.

The equation of motion of structure with TMD can be expressed as

$$m \ddot{x} + c \dot{x} + kx = -m \ddot{x}_g(t) + c_1 \dot{x}_1 + k_1 x_1, \quad (2)$$

where m , c , and k are the mass, damping, and stiffness of structure, respectively, and $\ddot{x}_g(t)$ is the input seismic wave.

2.2. Equation of Motion of a System with TMD under Seismic Excitation. If a tuned mass damper is fixed on the tower under seismic excitation, then the equation of motion of the structure with TMD control can be expressed as

$$\begin{aligned} M \ddot{x} + C \dot{x} + Kx - \{E\} (c_t \dot{x}_t + k_t x_t) &= -M \ddot{u}_g, \\ m_t (\ddot{x}_t + E^T \ddot{x}) + c_t \dot{x}_t + k_t x_t &= 0, \end{aligned} \quad (3)$$

where M , C , and K are the mass, damping, and stiffness matrix of tower structure, respectively; x , \dot{x} , and \ddot{x} are the vector of the displacement, velocity, and acceleration of tower structure, respectively; m_t , c_t , and k_t are the mass, damping, and stiffness of the TMD, respectively; x_t , \dot{x}_t , and \ddot{x}_t are the displacement, velocity and acceleration of the TMD, respectively; E is the tuned mass damper located position vector.

Equations (3) can be written in a unified expression form

$$\begin{aligned} \begin{bmatrix} M_{aa} & M_{ab} & 0 \\ M_{ba} & M_{bb} & 0 \\ 0 & m_t E^T & m_t \end{bmatrix} \begin{Bmatrix} \ddot{x}_a \\ \ddot{x}_b \\ \ddot{x}_t \end{Bmatrix} + \begin{bmatrix} C_{aa} & C_{ab} & 0 \\ C_{ba} & C_{bb} & -EC_t \\ 0 & 0 & c_t \end{bmatrix} \begin{Bmatrix} \dot{x}_a \\ \dot{x}_b \\ \dot{x}_t \end{Bmatrix} \\ + \begin{bmatrix} K_{aa} & K_{ab} & 0 \\ K_{ba} & K_{bb} & -Ek_t \\ 0 & 0 & k_t \end{bmatrix} \begin{Bmatrix} x_a \\ x_b \\ x_t \end{Bmatrix} = \begin{Bmatrix} P_a \\ 0 \\ 0 \end{Bmatrix}, \end{aligned} \quad (4)$$

where M_{aa} , C_{aa} , and K_{aa} are the $m \times m$ mass, damping, and stiffness matrices associated with the supported degrees of freedom, respectively; M_{bb} , C_{bb} , and K_{bb} are the $n \times n$ mass, damping, and stiffness matrices associated with the unconstrained degrees of freedom, respectively; M_{ab} , C_{ab} , and K_{ab} are the $m \times n$ coupling matrices associated with both sets of degrees of freedom; P_a is the m -vector of the reacting

forces at the support degrees of freedom; $\ddot{\mathbf{x}}_a$, $\dot{\mathbf{x}}_a$, and \mathbf{x}_a are the vector of the ground motion; $\ddot{\mathbf{x}}_b$, $\dot{\mathbf{x}}_b$, and \mathbf{x}_b are the vector of the unconstrained degrees of freedom.

Based on the second and third rows of (4), the dynamic balance equation can be expressed as

$$\begin{aligned} \mathbf{M}_{ba}\ddot{\mathbf{x}}_a + \mathbf{M}_{bb}\ddot{\mathbf{x}}_b + \mathbf{C}_{ba}\dot{\mathbf{x}}_a + \mathbf{C}_{bb}\dot{\mathbf{x}}_b \\ - E\mathbf{c}_d\dot{\mathbf{x}}_t + \mathbf{K}_{ba}\mathbf{x}_a + \mathbf{K}_{bb}\mathbf{x}_b - E\mathbf{k}_d\mathbf{x}_t = 0, \quad (5) \\ m_t E^T \ddot{\mathbf{x}}_b + m_t \dot{\mathbf{x}}_t + c_t \dot{\mathbf{x}}_t + k_t \mathbf{x}_t = 0. \end{aligned}$$

Assuming that the mass matrix is diagonal and \mathbf{C}_{ab} is neglected, (5) is reduced to

$$\mathbf{M}_{bb}\ddot{\mathbf{x}}_b + \mathbf{C}_{bb}\dot{\mathbf{x}}_b + \mathbf{K}_{bb}\mathbf{x}_b - E(\mathbf{c}_d\dot{\mathbf{x}}_t + \mathbf{k}_d\mathbf{x}_t) = -\mathbf{K}_{ba}\mathbf{x}_a. \quad (6)$$

Equation (6) can be extended to three components:

$$\begin{aligned} \mathbf{M}_{bb}\ddot{\mathbf{x}}_b + \mathbf{C}_{bb}\dot{\mathbf{x}}_b + \mathbf{K}_{bb}\mathbf{x}_b - E(\mathbf{c}_d\dot{\mathbf{x}}_t + \mathbf{k}_d\mathbf{x}_t) \\ = -\mathbf{K}_{ba}(x_a + y_a + z_a), \quad (7) \end{aligned}$$

where x_a , y_a , and z_a are the input ground motion displacements in two horizontal and one vertical directions, respectively.

2.3. Calculation Formula of TMD. The tuned mass damper is constituted by mass block, spring, and damping. The mass block, spring, and damping can be derived as

$$\begin{aligned} m_d &= \mu M, \\ k_d &= m_d \omega^2, \\ c_d &= 2m_d \omega^2 \xi, \end{aligned} \quad (8)$$

where M is the mass of the tower structure, μ is mass ratio, ω is the frequency of the tower structure, and ξ is the damping ratio of the TMD. The optimal damping ratio is given in [12]

$$\xi = \sqrt{\frac{3\mu}{8(1+\mu)}}. \quad (9)$$

3. Modeling of Power Transmission Tower-Line System

A finite-element computer program SAP2000 is selected to establish the model. A typical transmission tower such as the one shown in Figure 3 is considered in the study. The tower is 49.7 m high, and the weight of the tower is approximately 19 t. The structural members of the tower are made of angle steel with the elastic modulus of 206 GPa. The tower is modeled by 1412 space beam members and 575 nodes, and the connections of members are rigid, and the base points of the tower are assumed fixed. Figure 4 shows the transmission tower finite model. The frequencies of free vibration corresponding to the first three modes of the tower are found to be 1.71, 1.93, and 2.44 Hz, respectively.

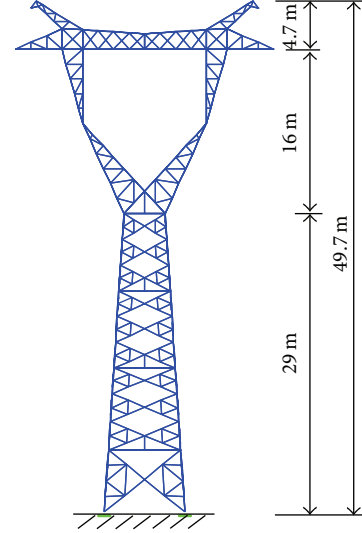


FIGURE 3: Transmission tower.

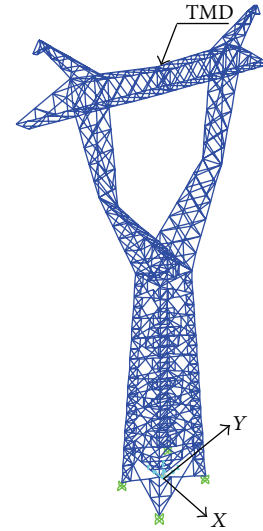


FIGURE 4: Transmission tower finite model.

Each transmission line is modeled by two-node isoparametric cable elements with three translational degrees of freedom at each node. The initial axial force and large deformation effect of cable are taken into consideration. Under self-weight, the cable spatial configuration is a catenary. Based on the coordinate system illustrated in Figure 5, the mathematical expression used to define the initial geometry of the cable profile is given in the following form [13]:

$$z = \frac{H}{q} \left| \cosh(\alpha) - \cosh\left(\frac{2\beta}{l} - \alpha\right) \right|, \quad (10)$$

where $\alpha = \sin h^{-1}|\beta(c/l)/\sin(\beta)| + \beta$, $\beta = (ql/2H)$, in which H represents initial horizontal tension which can be obtained from a preliminary static analysis, and q denotes uniformly distributed gravity loads along the transmission line.

The types of transmission conductor and ground wire are LGJ-400/35 and LGJ-95/55, respectively. Conductor line and

TABLE 1: Conductor line and ground line properties.

Type	Conductor line	Ground line
Transmission line	LGJ-400/35	LGJ-95/55
Outside diameter (m)	$26.82E-3$	$16.00E-3$
Modulus (GPa)	65	105
Transversal cross-section (m ²)	$425.24E-6$	$152.81E-6$
Mass per unit length (Kg/m)	1.3490	0.6967
Line expansion coefficient (1/°C)	$2.05E-005$	$1.55E-005$

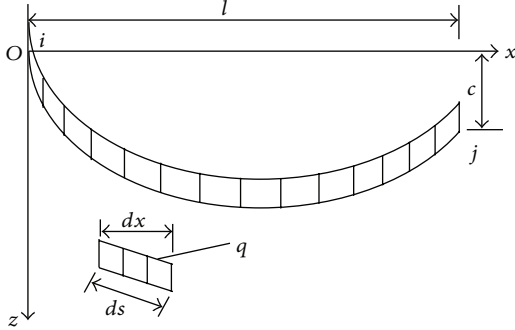


FIGURE 5: Coordinates of a single cable under self-weight.

ground wire properties are shown in Table 1. There are 20 transmission lines including 12 transmission conductors and 8 ground lines. As shown in Figure 6, the transmission tower-line coupled system includes three towers (1[#] tower, 2[#] tower, and 3[#] tower) and four-span line (Span 1, Span 2, Span 3, and Span 4), and the side spans of the lines are hinged at the same height of middle tower [14]. The spans of adjacent towers are all 425 m.

4. Optimal Design of the System with TMD

The transmission tower-line system shown in Figure 6 is used in the numerical simulation analysis. The damping ratio of the tower and line are assumed to be 2% and 1%, respectively. The Newmark- β method is applied in the numerical integration. The top node and along the height of middle transmission tower (2[#] tower) are selected as the object of the study. Three components of the 1940 Imperial Valley earthquake at El Centro site are used for time-history analysis, with peak ground motion scaled to 0.4 g along the Y-direction of system, and the other direction of seismic waves are adjusted according to corresponding proportion. The location of TMD on the tower can be seen in Figure 4. The reduction ratio is better when the location of TMD on the top of tower than other locations, so the reduction ratio about the location is not discussed.

In order to study the effect of control on the seismic responses of structure, vibration reduction ratio, δ , can be defined as

$$\delta = \frac{R_0 - R_1}{R_0} \times 100\%, \quad (11)$$

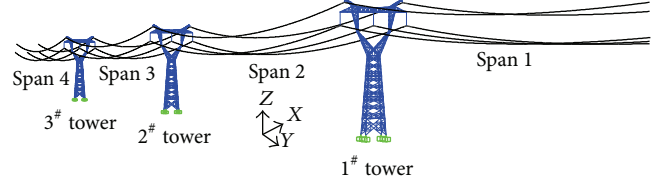


FIGURE 6: Three-dimensional finite model of the transmission tower-line coupled system.

where R_0 and R_1 are the responses of the tower without and with control, respectively.

4.1. Response of Single Tower and Tower-Line System with TMD. To compare the effect of TMD control on the response of single tower and transmission tower-line system, the single tower and tower-line system without and with TMD control are analyzed, respectively. The mass ratio of TMD is 2% in this section.

Figure 7(a) and Figure 8(a) show the top displacements in X-direction of the single tower and 2[#] tower of system, and their vibration reduction ratios are 34.5% and 21.3%, respectively. The top displacements in Y-direction of the single tower and 2[#] tower of system are shown in Figure 7(b) and Figure 8(b), and their vibration reduction ratios are 20.8% and 26.2%, respectively. As shown in Figures 7(c) and 8(c), the axial forces along the height of the single tower and 2[#] tower of system are given, and their vibration reduction ratios are approximately 19.0% and 9.0%, respectively.

The previous results show that the control effect of the displacement of the single tower is larger than that of 2[#] tower of system in X-direction, but the opposite results in Y-direction. The control effect of axial force of the single tower is significantly larger than that of 2[#] tower of system. Because of the coupled effect and flexible connection of the transmission towers and lines, the control effect of transmission tower-line system is different from that of the single tower. Therefore, the vibration control design of transmission tower should consider the effect of transmission lines.

4.2. Effect of Mass Ratio. In order to investigate the effect of mass ratio of TMD on the response of the system, ten different mass ratios are considered in the analysis, 0.01, 0.015, 0.02, 0.025, 0.03, 0.04, 0.05, 0.06, 0.07, and 0.08.

Vibration reduction ratios of 2[#] tower of system with different mass ratios are shown in Figure 9. It can be seen from Figure 9 that the vibration reduction effect can be improved according to increasing mass ratio, but there is an optimal mass ratio, after which adding more mass would slightly improve effect. The vibration reduction ratios of displacement and acceleration in X-direction increase significantly to 33.9% and 34.6% with mass ratio increasing until 4%. The vibration reduction ratios of displacement and acceleration in Y-direction increase significantly to 35.9% and 31.7% with mass ratio increasing until 4%. The

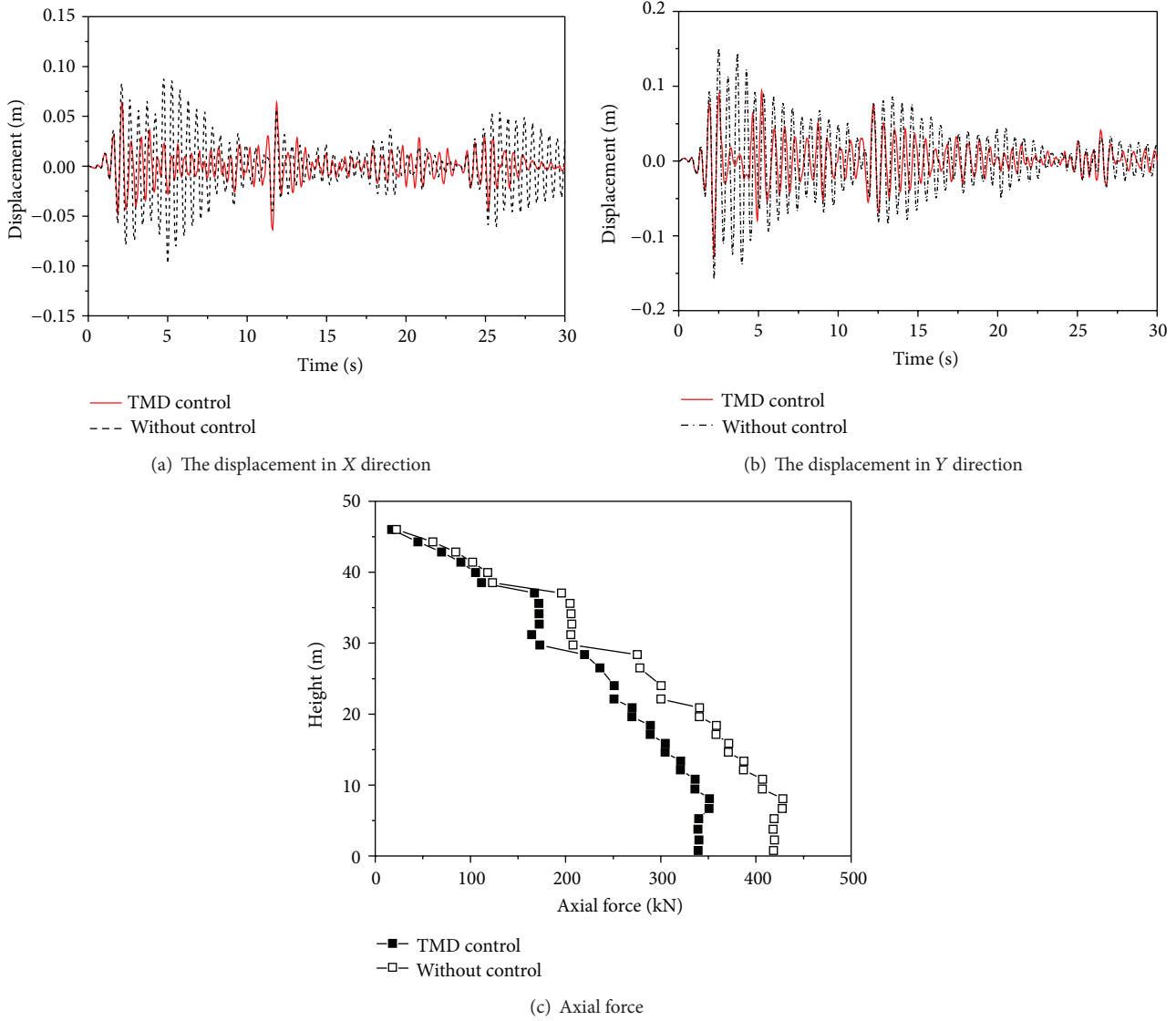


FIGURE 7: The response of single tower under El Centro wave excitation.

vibration reduction ratio of axial force increases significantly to 22% with mass ratio increasing until 4%. Afterwards, the performance is improved to be less than 4% adding 1% more mass. Therefore, the optimal design of the mass ratio of TMD is 4%.

4.3. Robustness Study. In order to study the robustness of TMD, the case where the ice loads are on the transmission tower and line is taken into consideration. The optimal design of the mass ratio of TMD is selected in this section. It is assumed that the whole transmission line is icing; the cover ice thickness is 30 mm, and density of ice coating is 0.9 g/cm^3 .

The displacement time histories of 2[#] tower of system with ice under El Centro wave excitation are shown in Figure 10. It is seen from Figure 10 that the vibration reduction ratios of 2[#] tower of system with ice in X- and Y-directions are 33.8% and

27.7%, respectively. The mass and natural frequency of tower may be changed by ice load, so the vibration reduction ratio would be changed.

5. Parameter Study

Responses of the transmission tower-line system without and with TMD subjected to multicomponent multisupport ground motions are analyzed. The HHT method is applied in the numerical integration. Based on the above research, the optimal design of the mass ratio of TMD is selected.

5.1. Simulation of Multicomponent Multisupport Ground Motions. The ground motion cross-power spectral density function of spatial ground motions at points i and j on ground surface can be written as

$$S_{ij}(\omega) = S_g(\omega) \gamma_{ij}(\omega, d_{ij}), \quad (12)$$

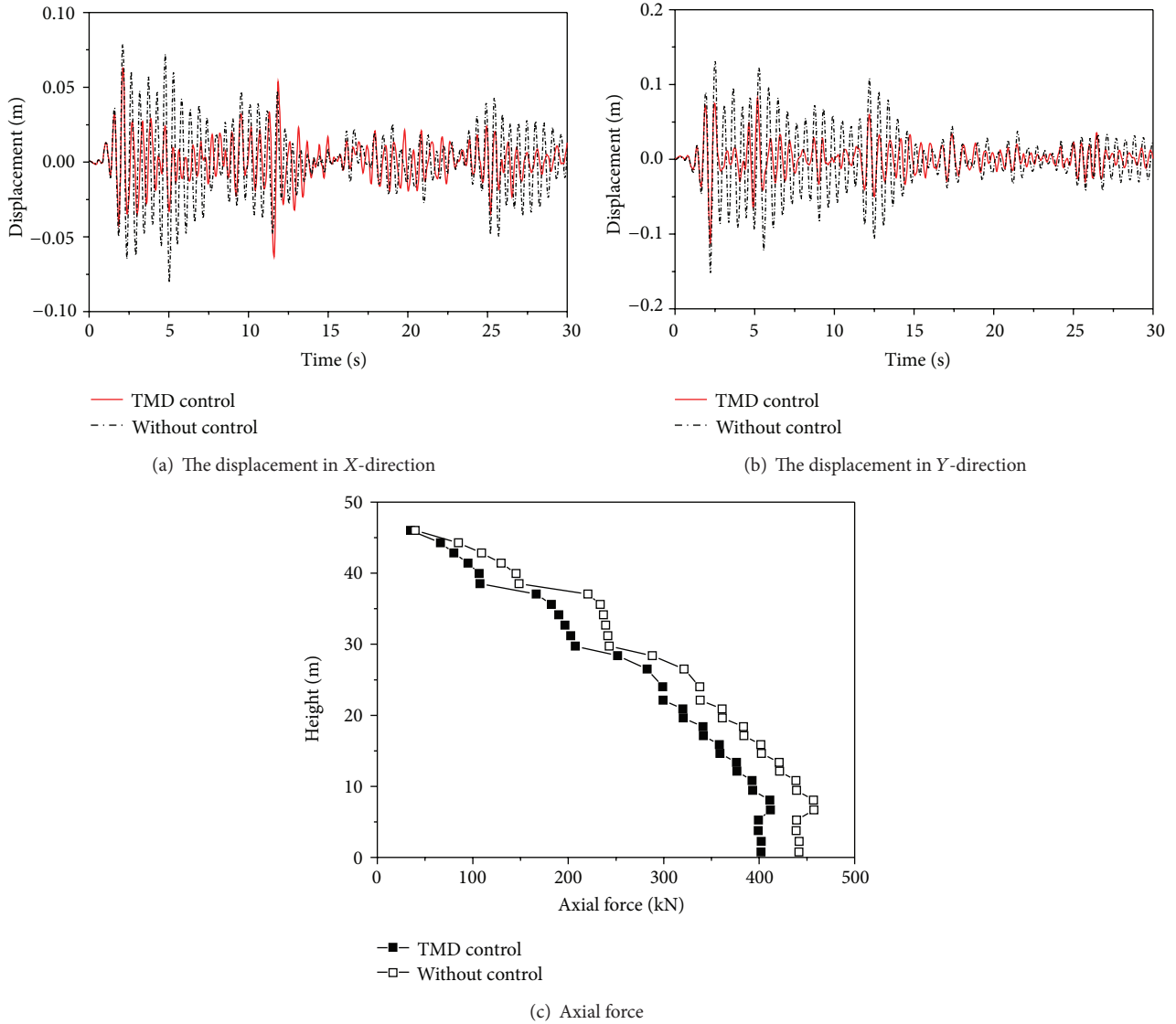


FIGURE 8: The response of 2[#] tower of system under El Centro wave excitation.

where

$$S_g(\omega) = \frac{\omega_g^4 + 4\xi_g^2\omega_g^2\omega^2}{(\omega_g^2 - \omega^2)^2 + 4\xi_g^2\omega_g^2\omega^2} \cdot \frac{\omega^4}{(\omega_f^2 - \omega^2)^2 + 4\xi_f^2\omega_f^2\omega^2} S_0 \quad (13)$$

is a filtered Tajimi-Kanai power spectral density function [15], in which S_0 is a scale factor depending on the ground motion intensity, ω_g and ξ_g are the predominant frequency and damping ratio of the first filter, and ω_f and ξ_f are those of the second filter. Consider the following:

$$\gamma_{ij}(\omega, d_{ij}) = \left| \gamma_{ij}(\omega, d_{ij}) \right| e^{-i\omega d_{ij}/v} \quad (14)$$

is an empirical coherency function. In the present paper, the coherency loss function at points i and j was derived from SMART-1 array data by Hao et al. [16]. The parameters were obtained by processing recorded motions during event 45 at the SMART-1 array. In order to compare, different degrees of coherency loss are selected according to reference [17].

According to Penzien and Watabe's research [18], the three components of ground motions along a set of principal axes are uncorrelated. In this study, the three components of the ground motion are assumed to be directed along the principal axes.

In this study, the transmission tower-line system is assumed to be located in the Chinese Seismic Intensity Zone 9 with peak longitudinal ground acceleration 0.4 g and locate in the medium firm soil. The intensities of the transverse component and vertical component, as stated in the code, are 0.85 and 0.65 times of the longitudinal component. Based on

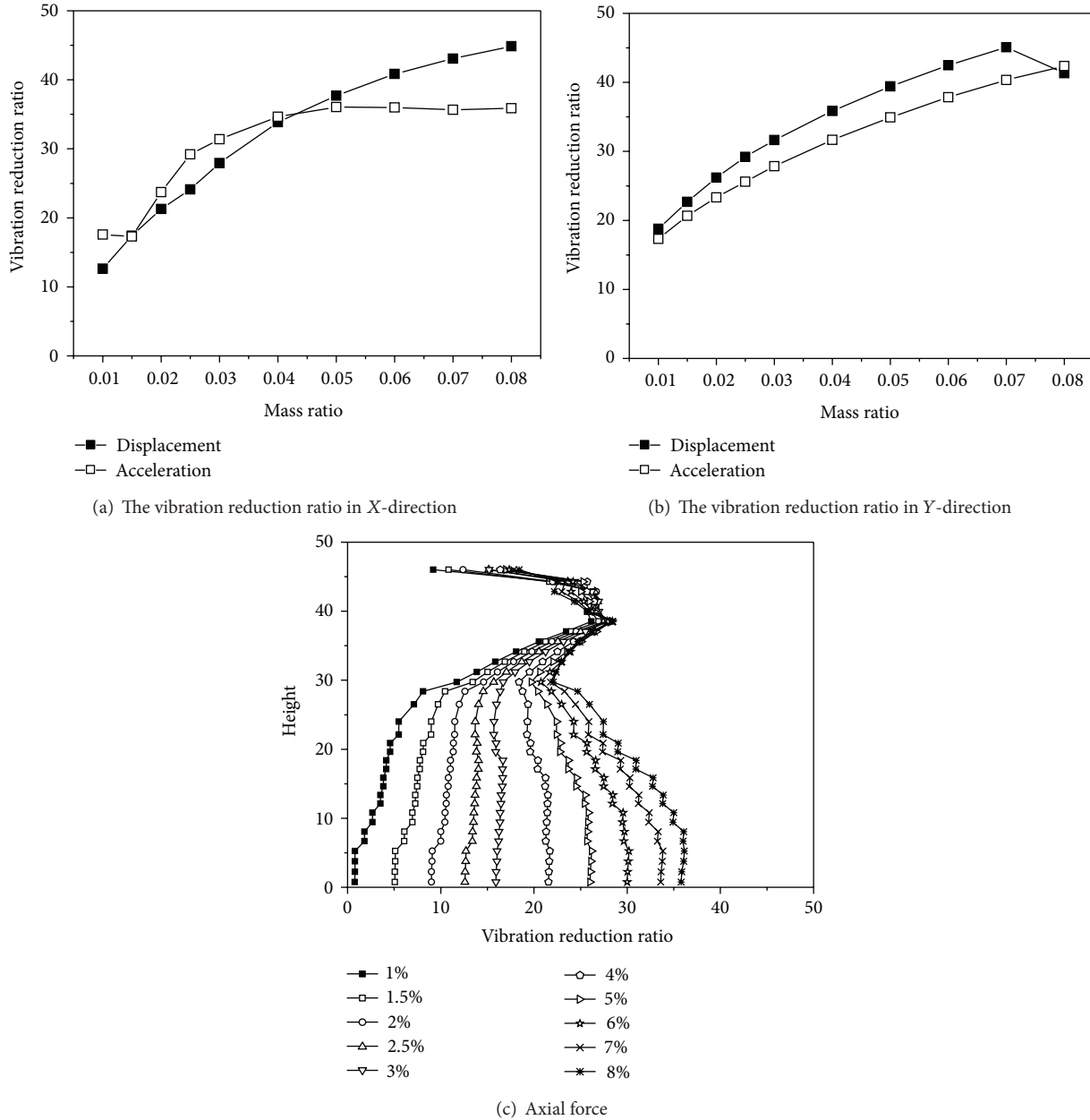


FIGURE 9: Vibration reduction ratios of 2[#] tower of system with different mass ratio.

the reference method [14], the multi-component and multi-support seismic can be generated. Figure 11 shows multi-component multi-support ground motions time histories.

5.2. *Effect of Wave Travel.* To investigate the effect of wave travel on the response of the system with TMD, six different velocities of wave propagation are considered in the analysis, uniform (Case 1), 1000 m/s (Case 2), 1500 m/s (Case 3), 2000 m/s (Case 4), and infinite (Case 5). The case of uniform ground motion at all supports corresponds to a wave propagating with infinite velocity, and the case of infinite ground motion only considers the effect of coherency loss. In all these cases, the coherency loss and soil condition of

ground motion are assumed to be highly correlated and the medium firm, respectively.

Figure 12 shows the vibration reduction ratios of 2[#] tower of system under different wave travel excitations. It can be seen from Figure 12 that the vibration reduction effect can be changed greatly under different wave travel excitations, especially for the vibration reduction ratios of displacement in X-direction. The response of displacement in X-direction with control is larger than that without control when the velocity is 1500 m/s, but the other results with control are smaller than that without control. When the apparent velocity is 1000 m/s, the vibration reduction ratios of displacement and acceleration in Y-direction are larger than other cases. The

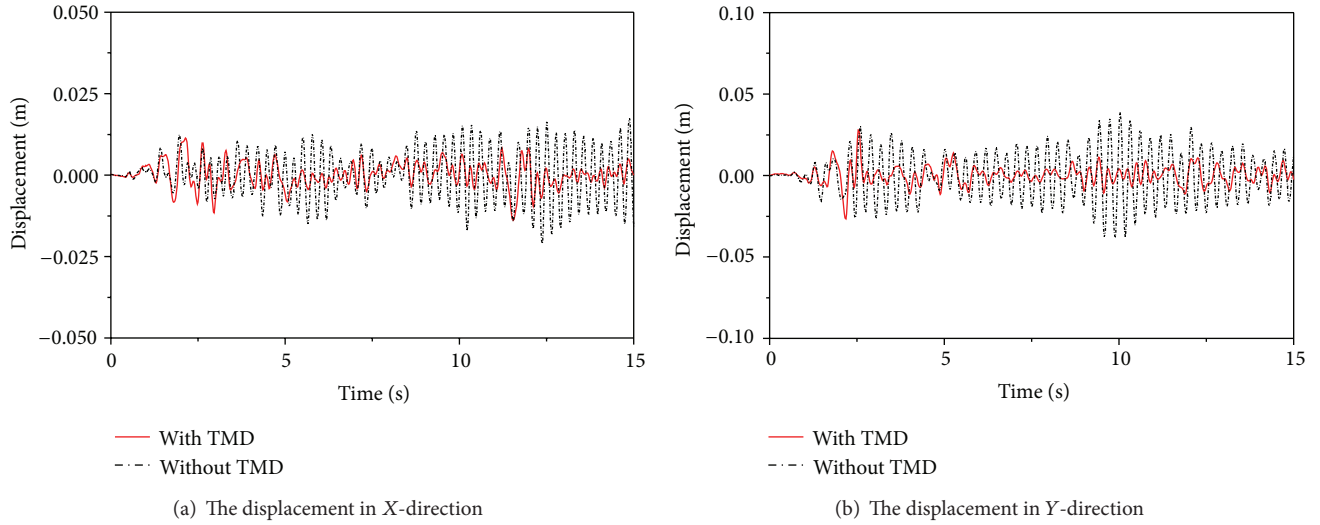


FIGURE 10: Displacement time histories of 2[#] tower of system with ice under El Centro wave excitation.

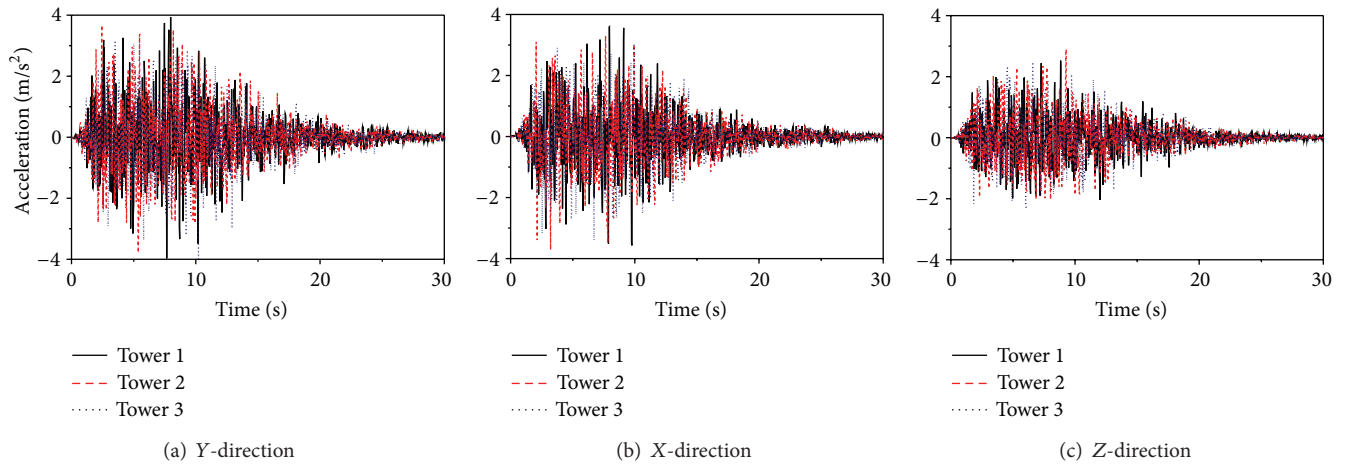


FIGURE 11: Seismic waves of every transmission tower supports in three-dimensional direction.

vibration reduction ratio of axial force at bottom of system under uniform excitation is smaller than those considering the effect of wave travel.

According to the variations of the vibration reduction ratios of system considering the change of traveling wave velocity, the traveling wave velocity has a significant influence on the vibration reduction ratio of the system. Therefore, the traveling wave velocity cannot be ignored for the vibration reduction ratios of transmission tower-line system.

5.3. Effect of Coherency Loss. To study the influence of coherency loss on the response of the system with TMD, uniform (Case 1), completely correlated (Case 2), highly correlated (Case 3), and intermediately correlated (Case 4) ground motions are considered. In all these cases, the apparent velocity and soil condition of ground motion are assumed to be 1000 m/s and the medium firm, respectively.

Figure 13 shows the vibration reduction ratios of 2[#] tower of the system under different degrees of coherency loss.

The vibration reduction ratios of the system are affected significantly by the change of coherency loss. The vibration reduction ratios of acceleration in X displacement of the system have a tendency of increasing with the degrees of coherency loss decreasing, but the displacement has an opposite tendency. The vibration reduction ratios of displacement and acceleration in Y displacement are larger than other cases when the coherency loss is highly correlated. The vibration reduction ratios of axial force of the system have a tendency of decreasing with the degrees of coherency loss decreasing.

The variations of the vibration reduction ratios of the system considering the change of coherency loss can be obtained from above analyses. To obtain a representative analysis, the degrees of coherency of spatial ground motions should be evaluated.

5.4. Effect of Site Condition. In order to research the effect of local site on the response of the system with TMD, uniform (Case 1), MF-MF-MF (Case 2), MF-F-F (Case 3), MF-MS-MS

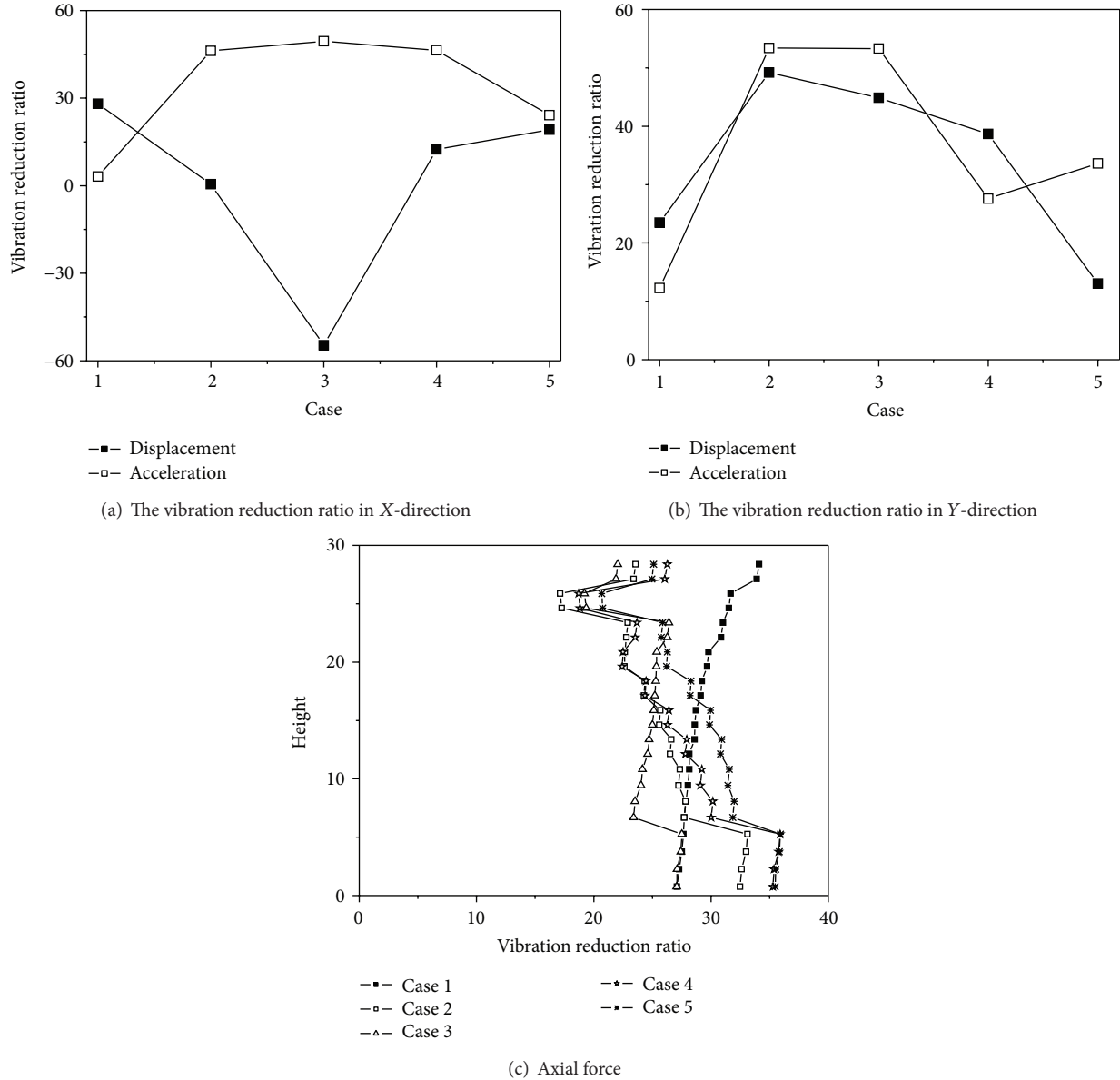


FIGURE 12: Vibration reduction ratios of 2[#] tower of system under different wave travel excitations.

(Case 4), and MF-S-S (Case 5) are considered. F, MF, MS, and S are denoted as firm, medium firm, medium soft, and soft soil. In all these cases, the apparent velocity and coherency of ground motion are assumed to be 1000 m/s and highly correlated, respectively.

Figure 14 shows the vibration reduction ratios of 2[#] tower of system under different site conditions. The responses of displacements of system in X-direction with control are larger than those without control when considering the different local site conditions, but the acceleration has opposite results. The vibration reduction ratios of displacement and acceleration in Y-direction have the same variations, and the vibration reduction ratio is smaller than other cases when local site is MF-F-F. The vibration reduction ratio of axial force of system under MF-MS-MS site conditions excitation is larger than other cases.

The above results demonstrate that the site condition has a great influence on the vibration reduction ratios of system. Therefore, it is necessary to consider the local site of ground motion.

6. Conclusions

The seismic control of the transmission tower-line system under multi-component has been investigated in this paper. The optimal design of the system with TMD is investigated. The parameters studied include the effect of wave passage, coherency loss and different local site. Based on the numerical results and analysis, the following conclusions are drawn.

- (1) The control effect of transmission tower-line system is different from the single tower, so the vibration

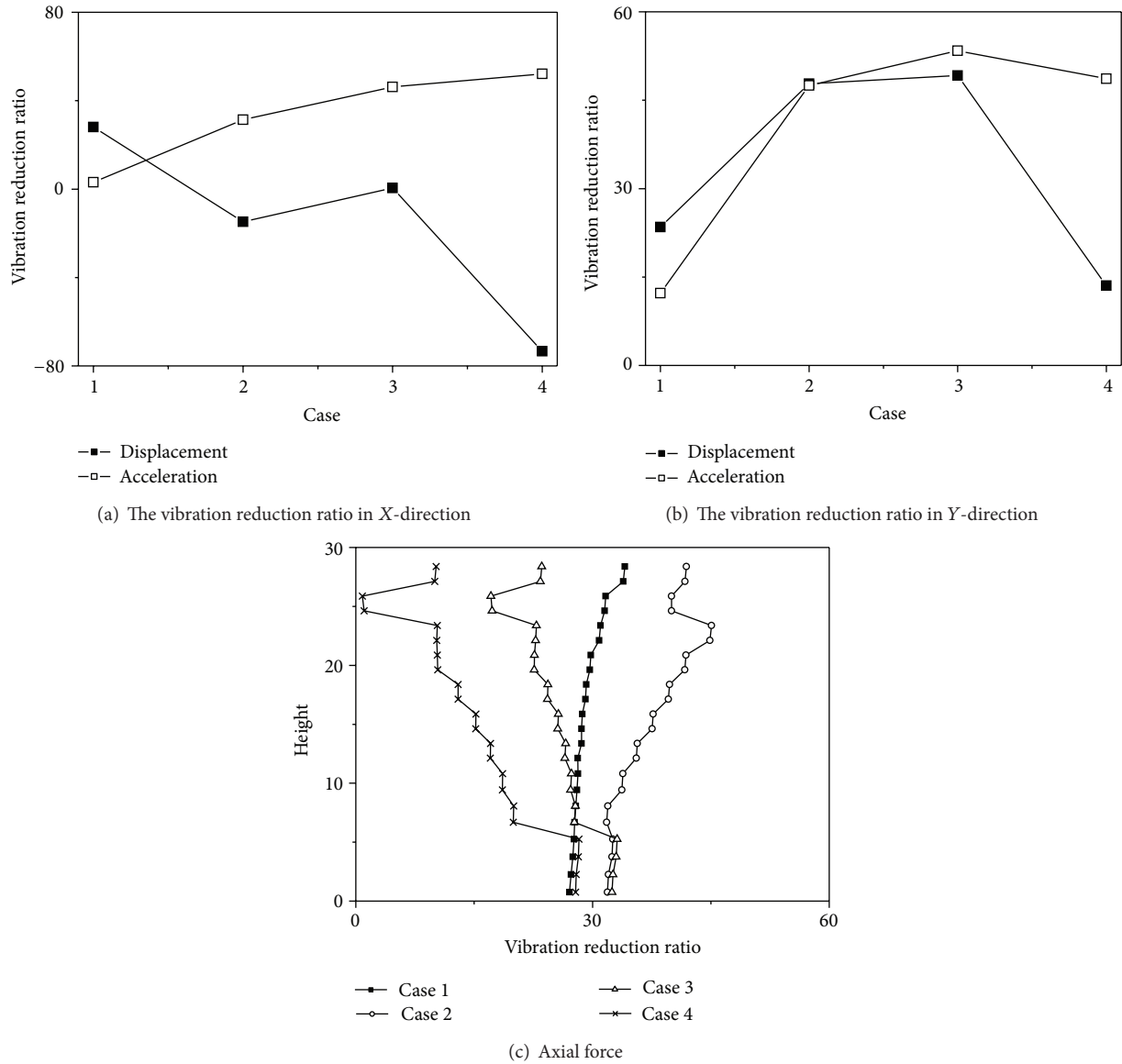


FIGURE 13: Vibration reduction ratios of 2nd tower of system under different degrees of coherency loss.

- control design of transmission tower should consider the effect of transmission lines.
- (2) According to different mass ratio, the optimal design of the transmission tower-line system with TMD could be obtained.
 - (3) The mass and natural frequency of tower may be changed by ice load, so the vibration reduction ratio would be changed.
 - (4) The traveling wave velocity has a significant influence on the vibration reduction ratio of the system, and the traveling wave velocity can not be ignored for the vibration reduction ratios of transmission tower-line system
 - (5) To obtain a representative analysis, the degrees of coherency of spatial ground motions should be evaluated.
 - (6) The site condition has a great influence on the vibration reduction ratios of system, and it is necessary to consider the local site of ground motion.
- This study demonstrates that the multi-component multi-support seismic excitations are very important to power transmission tower-line system. Therefore, more studies are deemed necessary to further investigate the multi-component multi-support ground motions effects on responses of these systems with control.

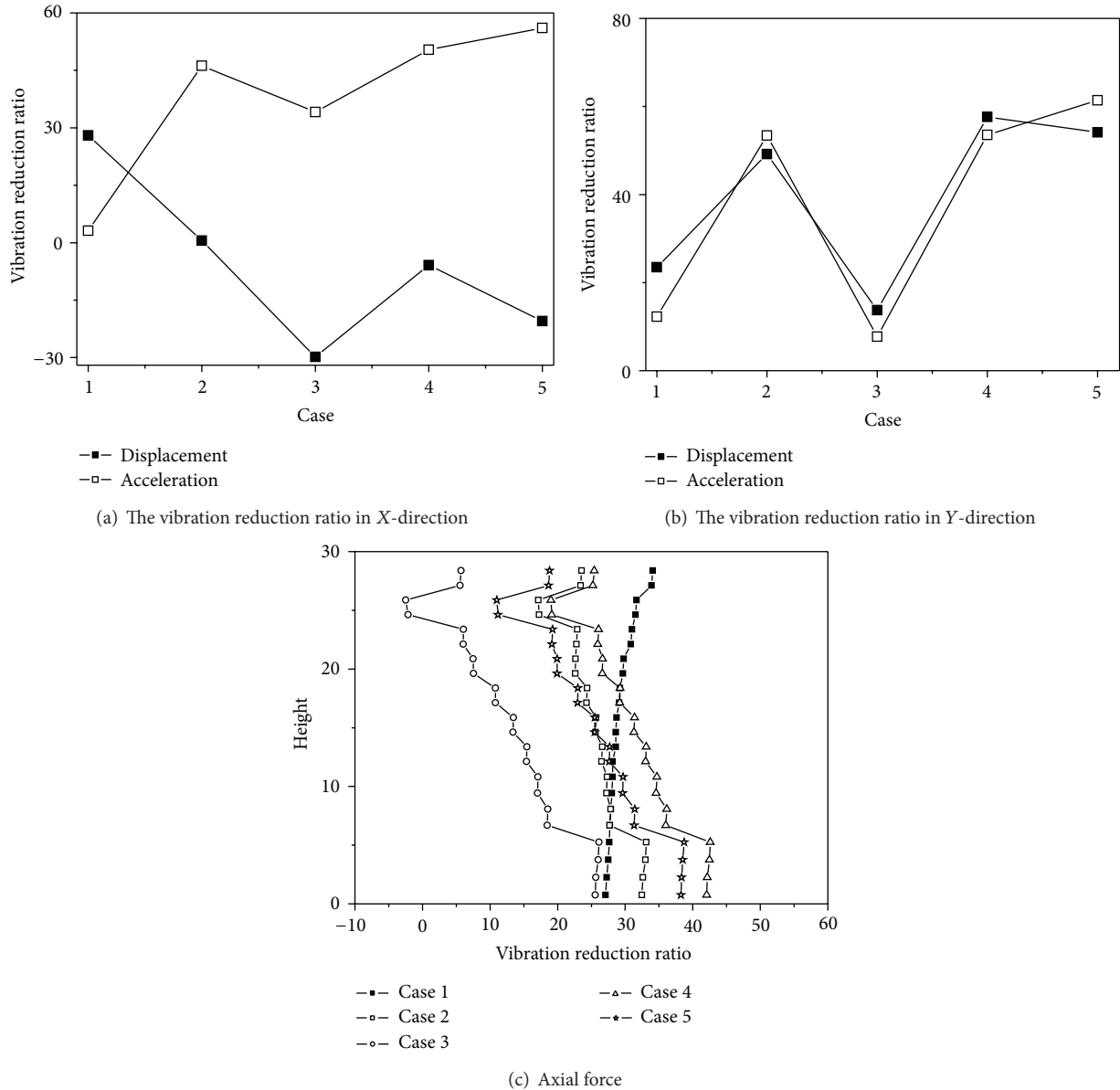


FIGURE 14: Vibration reduction ratios of 2[#] tower of system under different site conditions.

Acknowledgments

This work is supported by the National Natural Science Foundation of China under Grant no. 51208285, China Postdoctoral Science Foundation funded project under Grant no. 2012M521338, and Independent Innovation Foundation of Shandong University of China under Grant no. 2011GN051. The supports for this research are greatly appreciated.

References

[1] H. Li, W. Shi, G. Wang, and L. Jia, "Simplified models and experimental verification for coupled transmission tower-line system to seismic excitations," *Journal of Sound and Vibration*, vol. 286, no. 3, pp. 569–585, 2005.

[2] Q. Xie and J. Li, "Current situation of natural disaster in electric power system and countermeasures," *Journal of Natural Disasters*, vol. 15, no. 4, pp. 126–131, 2006 (Chinese).

[3] M. Shinozuka, "The Hanshin-Awaji earthquake of January 17, 1995 performance of life lines," Report NCEER-95-0015, NCEER, Alachua, Fla, USA, 1995.

[4] R. Yin, D. Li, G. Liu, and T. Zhai, "Seismic damage and analysis of power transmissions towers," *World Information on Earthquake Engineering*, vol. 21, no. 1, pp. 51–54, 2005 (Chinese).

[5] D. Zhang, W. Zhao, and M. Liu, "Analysis on seismic disaster damage cases and their causes of electric power equipment in 5. 12 Wenchuan earthquake," *Journal of Nanjing University of Technology*, vol. 31, no. 1, pp. 44–48, 2009 (Chinese).

[6] R. C. Battista, R. S. Rodrigues, and M. S. Pfeil, "Dynamic behavior and stability of transmission line towers under wind forces,"

- Journal of Wind Engineering and Industrial Aerodynamics*, vol. 91, no. 8, pp. 1051–1067, 2003.
- [7] B. Huang and J. Tang, “Wind-induced vibration control of long span transmission tower,” *Control of Noise and Vibration*, no. 5, pp. 2–5, 1997 (Chinese).
- [8] Y. Chen and G. Tang, “Vibration control on tower for long span transmission lines,” *Special Structure*, vol. 17, no. 3, pp. 43–46, 2000 (Chinese).
- [9] H. Deng, S. Zhu, Y. Chen, and Z. Wang, “Study on wind-induced vibration control of long span transmission line system,” *Journal of Building Structures*, vol. 18, no. 4, pp. 60–65, 2003 (Chinese).
- [10] G. Liu and H. Li, “Analysis and optimization control of wind-induced dynamic response for high-voltage transmission tower-line system,” *Proceedings of the Chinese Society of Electrical Engineering*, vol. 28, no. 19, pp. 131–137, 2008 (Chinese).
- [11] J. P. D. Hartog, *Mechanical Vibrations*, McGraw-Hill, New York, NY, USA, 1956.
- [12] R. Rana and T. T. Soong, “Parametric study and simplified design of tuned mass dampers,” *Engineering Structures*, vol. 20, no. 3, pp. 193–204, 1998.
- [13] S. Z. Shen, C. B. Xu, and C. Zhao, *Design of Suspension Structure*, China Architecture and Building Press, Beijing, China, 1997, (Chinese).
- [14] L. Tian, H. Li, and G. Liu, “Seismic response of power transmission tower-line system subjected to spatially varying ground motions,” *Mathematical Problems in Engineering*, vol. 2010, Article ID 587317, 20 pages, 2010.
- [15] R. W. Clough and J. Penzien, *Dynamics of Structures*, McGraw-Hill, New York, NY, USA, 1975.
- [16] H. Hao, C. S. Oliveira, and J. Penzien, “Multiple-station ground motion processing and simulation based on SMART-1 array data,” *Nuclear Engineering and Design*, vol. 111, no. 3, pp. 1325–1345, 1989.
- [17] K. Bi, H. Hao, and N. Chouw, “Required separation distance between decks and at abutments of a bridge crossing a canyon site to avoid seismic pounding,” *Earthquake Engineering and Structural Dynamics*, vol. 39, no. 3, pp. 303–323, 2009.
- [18] J. Penzien and M. Watabe, “Characteristics of 3-dimensional earthquake ground motions,” *Earthquake Engineering and Structural Dynamics*, vol. 4, pp. 365–373, 1975.

Research Article

Application of Fuzzy Control with Market-Based Control Strategy to Structures

Gang Li,¹ Hong-Nan Li,² and Qi-Feng Liu¹

¹ Faculty of Infrastructure Engineering, Dalian University of Technology, Institute of Earthquake Engineering, Dalian, Liaoning 116024, China

² Faculty of Infrastructure Engineering, Dalian University of Technology, Dalian, Liaoning 116024, China

Correspondence should be addressed to Gang Li; gli@dlut.edu.cn

Received 21 April 2013; Accepted 7 July 2013

Academic Editor: Gang-Bing Song

Copyright © 2013 Gang Li et al. This is an open access article distributed under the Creative Commons Attribution License, which permits unrestricted use, distribution, and reproduction in any medium, provided the original work is properly cited.

The market-based control as a control strategy is developed based on an analogy between the control force-energy source in the structural area and the supply demand in the free market. The optimal problem of control force from an actuator is transformed to that of the allocation resource in the market. Since the supply-demand relation model and iteration procedure for the optimal price solution are necessary and relatively hard to understand and perform for civil engineers, the fuzzy logical method is proposed in the framework of the market-based control to acquire an equivalent system corresponding to the market-based control method. An equivalent fuzzy logical rule is established through analyzing a single-degree-of-freedom system with the controller using the MBC strategy under earthquakes. The results show that the fuzzy logical method is able to also reduce the displacement and acceleration responses effectively similar to the MBC method, and the consumed computational time for the fuzzy logical method is obviously saved.

1. Introduction

At present, the structural control technique is verified as an effective way to reduce responses of structures under natural hazards such as earthquakes and strong winds. Over past few years, a number of structural control strategies have been developed and applied in practices, specifically in seismic regions. Structural control systems, in general, fall into four categories: passive, active, semiactive, and hybrid control based on whether the power source is necessary. For the active and semiactive control technique, the control force is often determined by control strategies. Conventional control strategies include the linear quadratic regulator (LQR), modal control, smart control, and H_2 and H_∞ [1–3]. The market-based control (MBC) as a multiobjective distributed control approach achieves the optimal allocation of the control energy and determines the controlling force by modeling seller and buyer behaviors in the free-market area. The optimal problem of control force from the actuator in the structural control area is then transformed to that of

allocation resources in the market. Since the MBC concept was proposed by Clearwater [4], it had been developed and applied in many fields, such as the telecommunication, mechanism, and mission plan [5–9]. Lynch and Law [10] firstly applied the MBC method in civil engineering and subsequently presented a market-based energy control method. Huo and Li [11] incorporated the MBC in the tuned liquid column damper for reducing structural responses. Li [12] developed supply-demand relations and further improved control effectiveness. In addition, Li et al. [13] presented a way to compress the computation time for the nonlinear analysis of the structure through combining the MBC and the force analogy method.

After stepping into the 21st century, more and more works were focused on the implementation of the artificial intelligent algorithm in the structural control. The fuzzy logical method (FLM), as an intelligent algorithm, was incorporated in the structural control and developed in few years ago. Advantages of the FLM are effective and easy in handling nonlinearities, uncertainties, and heuristic knowledge when

it was applied in the active and semiactive control. Aldawod et al. [14] designed a multiobjective optimal fuzzy logic controller for seismically excited building structures and verified its inherent robustness and ability to handle nonlinearities and uncertainties in the structural behavior and loading. Ahlawat and Ramaswamy [15] applied the FLM for the active vibration control of tall buildings. Schurter and Roschke [16] used a neurofuzzy technique to control a single-degree-of-freedom and four-degrees-of-freedom building models. Park et al. [17] presented an independent modal space fuzzy control technique for the vibration control of earthquake-excited structures. The technique adopts a two-step design procedure consisting of designing an optimal controller in the modal space and fuzzy tuning of predesigned modal control gains. Bhardwaj and Datta [18] presented a methodology for the semiactive control of building frames using multiple semiactive hydraulic dampers driven by fuzzy controllers. The results of study showed that an efficient semiactive control strategy was developed using a fuzzy rule base. Kim and Roschke [19] validate the advantage of fuzzy logic approach on handling the nonlinear behavior of the system. Guclu and Yazici [20] investigated the effectiveness of a supervisory fuzzy control technique for the reduction of seismic response of a smart base isolation system. Zahrai and Shafieezadeh [21] designed a fuzzy logic based controller and used it to reduce vibrations of a tall building under cross-wind excitations. The results verified the superior performance of the semiactive fuzzy controller over the passive controller in response to mitigation of the perturbed structure. Zhao and Li [22] carried out a shaking table test of seismic response reduction of semiactive fuzzy control system including a new type of piezoelectric variable-friction damper and fuzzy controller. Yeh [23] developed an adaptive fuzzy sliding model control based Lyapunov theory and got a satisfactory result in the application of structural control for buildings with sliding bearing isolators.

The MBC has a distinct advantage when it is applied in a large complex structure, because it as a large unity consists of many markets so that it is capable of performing a decentralized control through dividing the large complex structure into several substructures and establishing corresponding relations among the substructures. However, the controlling effect for all substructures is determined by the supply-demand relation of markets, and the equilibrium price of the commodity is formed depending on its own supply-demand relation and the price tendency. The presence of numerous supply-demand relation models and iteration procedures for the optimal price solution is necessary and relatively hard to understand and perform for civil engineers, so that it makes the application of the MBC in this kind of structures more sophisticated. The FLM is incorporated in the framework of the MBC to acquire an equivalent system corresponding to the market-based control method in this study. The objective of present study is to simplify the process of the MBC and improve its robustness and uncertainty through incorporating the FLM into the structural vibration control procedure. An equivalent fuzzy rule is established through analyzing a single-degree-of-freedom (SDOF) system with the controller using the MBC strategy under earthquakes.

The robustness and uncertainty of the FLM are validated by its application in a multidegrees-of-freedom structure under different earthquakes.

2. Fundamental Background

2.1. Framework of MBC. The governing equation of motion for an SDOF system with controller can be expressed as

$$m\ddot{x}(t) + c\dot{x}(t) + kx(t) = -F(t) + U(t), \quad (1)$$

where $x(t)$, $\dot{x}(t)$, and $\ddot{x}(t)$ represent the displacement, velocity, and acceleration of the SDOF system, respectively; m and k are the system mass and stiffness; c denotes the viscous damping coefficient; $U(t)$ is the controlling force from the actuator, and $F(t)$ is the environmental load.

The MBC as a control algorithm can realize the structural vibration control through the analogy between the free market and structural control system. In the free market, the demand function J_D is determined by its energy consumption Q_D , energy price p , and dynamical responses $Y(t)$; the sellers' supply function J_S is determined by its own original energy Q_S and energy price p . Buyers and sellers both pursue their maximum interests at any time. This process has to be restricted by commodity quantities Q_{\max} and virtual wealth W_{\max} . Thus, the relation among these parameters is satisfied by

$$\begin{aligned} \max J_S(Q_S, p) \quad Q_S \leq Q_{\max}, \\ \max J_D(Q_D, p, Y(t)) \quad p \cdot Q_D \leq W_{\max}. \end{aligned} \quad (2)$$

Actually, the supply-demand relation is a core of the overall MBC theory. In the prior research, classical mathematical models have been presented, such as the linear-supply and linear-demand model [12], linear-supply and power-demand model, advanced linear-supply and power-demand model, and linear-supply and exponential-demand model [10]. As a classic model, the linear-supply and linear-demand relation reflects changes of the supply and demand in free market. The price is not obviously linear with the demand in markets, so the advanced linear-supply and power-demand and exponential-demand models were established and validated to be more accurate models. The fundamental framework of the MBC in the structural control has been presented in detail by Lynch and Law [10], so only a short summary based on the linear-supply and power-demand model (ALPM) is provided here as background.

The supply function is written as

$$Q_S = \eta \cdot p(t). \quad (3)$$

And the demand function is chosen to depict the relation of the demand and price as

$$Q_D = \frac{W(t) |\alpha x(t) + \beta \dot{x}(t)|}{p(t)}, \quad (4)$$

where η is the parameter that reflects the energy supply, and α and β are the weighting coefficients.

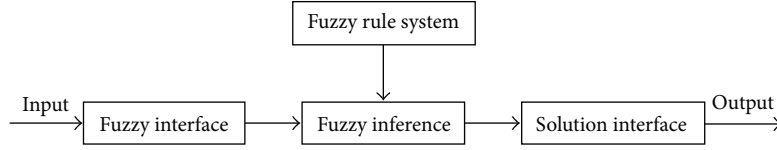


FIGURE 1: Fuzzy logical system.

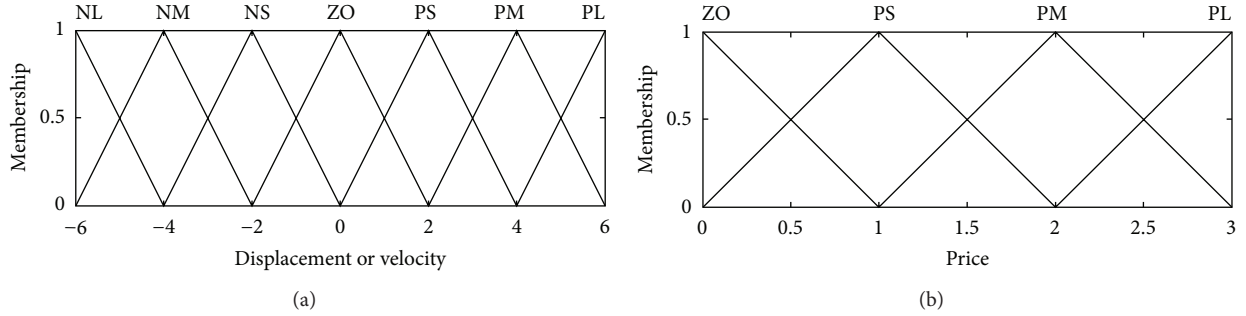


FIGURE 2: Relations of the membership and variables: (a) displacement or velocity; (b) price.

In the free market, there is a general equilibrium rule between the supply and demand. The rule can be expressed as

$$Q_S = Q_D. \quad (5)$$

Substituting (3) and (4) into (5), an equilibrium price is obtained through the resolution of (5) at any time step. The solution of (5) is called the Pareto optimal solution in economics [10]. Then, the control force is written as

$$U(t) = -K \cdot \frac{W(t) \cdot (\alpha x(t) + \beta \dot{x}(t))}{p(t)}, \quad (6)$$

where K is the gain coefficient related to the actuator. Substituting (6) into (1), the MBC in the structural control is implemented.

2.2. Fuzzy Logical Method. The FLM is capability to simplify the complex relation through mapping of only input-output information. The core of structural control is how to determine the controlling force through structural responses, such as displacement and velocity. This process is relatively complex and hard to solve. The controlling force in MBC is simulated to the price in market, so the structural displacement and velocity are selected as input variables to the fuzzy controller, and the output variable is defined as the price in the free market in this study, as shown in Figure 1. The whole price determination process is replaced by the fuzzy rule simplified through the FLC. The membership function for these three variables is selected as triangle with 50% overlap (Figure 2). The labels NL, NM, NS, ZO, PS, PM, and PL refer to the linguistic values: negative large, negative medium, negative small, zero, positive small, positive medium, and positive large, respectively.

Although the MBC mentioned in previous section is clear and simple, the presence of many supply-demand relations

leads to an expensive computation in time and makes the MBC strategy complex. In this study, an equivalent control system based on the FLM is developed to represent overall MBC solution process by using the unknown part of the system dynamics and the fuzzy learning model. The relation of the price, displacement x , and velocity \dot{x}_d can be written as

$$p(k) = R(x(k), \dot{x}(k)), \quad (7)$$

where k is the time at sampling; R represents the function of the fuzzy function.

3. Equivalent Fuzzy Price Rule

For illustration, a single-degree-of-freedom (SDOF) system, whose mass, stiffness, and damping ratios are 2.25×10^6 kg, 1.4×10^7 N/m, and 0.05, respectively, is excited by the El Centro north-south ground acceleration record from the 1940 Imperial Valley Earthquake. In order to obtain an equivalent fuzzy price rule to replace the MBC solution process, the dynamical response analysis of the SDOF structure with the controller based on the method presented in Section 2.2 was carried out. The three-dimensional relations of the price, displacement, and velocity are shown in Figure 3(a), and the fuzzy price rule is obtained and listed in Table 1. The rule surface that corresponds to the rule bases in Table 1 is generated as shown in Figure 3(b).

The whole process of the MBC in the structural control including the supply-demand relation and price solution is avoided, and much computational time is saved due to the establishment of price rule. It also can be found in Figure 4. In prior researches, the conclusion is that structural parameters and environmental loads have limited influence on the fuzzy rule. It also means that although the FLM is sourced from the SDOF under the given earthquake record, it is universal and will be verified in the next section.

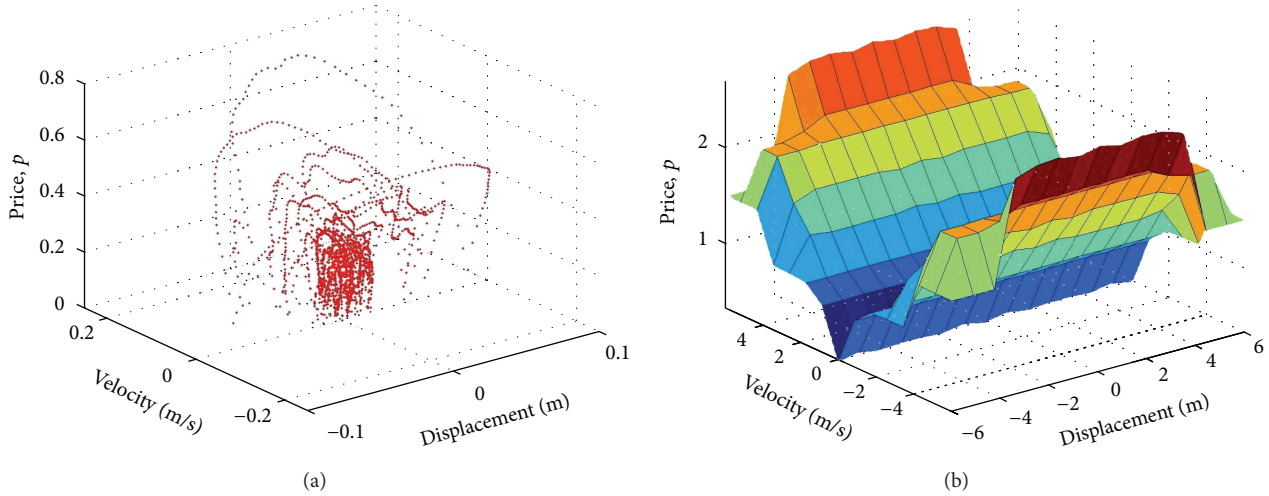


FIGURE 3: Three-dimensional graphic of the displacement, velocity, and price under El Centro earthquake: (a) the dotted graphic; (b) rule surface graphic.

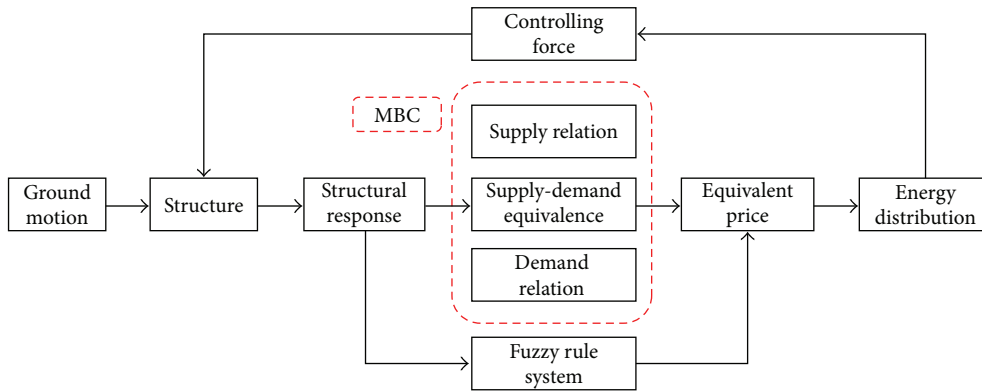


FIGURE 4: Procedure of the MBC and FLM.

TABLE 1: Fuzzy price rule.

Velocity	Displacement						
	NB	NM	NS	ZO	PS	PM	PB
NB	/	/	PB	PB	PB	/	/
NM	/	PM	PM	PM	PM	PM	/
NS	PS	PS	PS	PS	PS	PS	PS
ZO	ZO	ZO	ZO	ZO	ZO	ZO	ZO
PS	PS	PS	PS	PS	PS	PS	PS
PM	/	PM	PM	PM	PM	PM	/
PB	/	/	PB	PB	PB	/	/

Note: / means no rules in the case.

TABLE 2: Parameters of the ten-story structure.

Floor	1	2	3	4	5	6	7	8	9	10
Mass (10^3 kg)	980	980	980	980	980	980	980	980	980	980
Stiffness (10^6 N/m)	1819	1804	1774	1659	1559	1415	1728	1203	881.6	881.6

TABLE 3: Earthquake records.

Serial number	Station	Earthquake
1	El Centro	Imperial Valley (18/5/1940)
2	0453 Taft Lincoln School	Kern County (21/7/1952)
3	1028 Hollister City Hall	Hollister 1961/04/09

4. Application of the Fuzzy Control Method in the MDOF System

To validate the performance of the FLM established in the previous section, it is applied in a ten-story framed structure, whose parameters are shown in Table 2. In addition, three various earthquake records, which were scaled by various adjusted factors to 0.22g, are listed in Table 3 and selected

as inputting loads to verify the robustness of the FLM under different environmental loads. Three cases, which are the structure without control (FREE), with control based on the MBC, and with control based on the FLM, are conclude in this study to verify the effectiveness of the FLM.

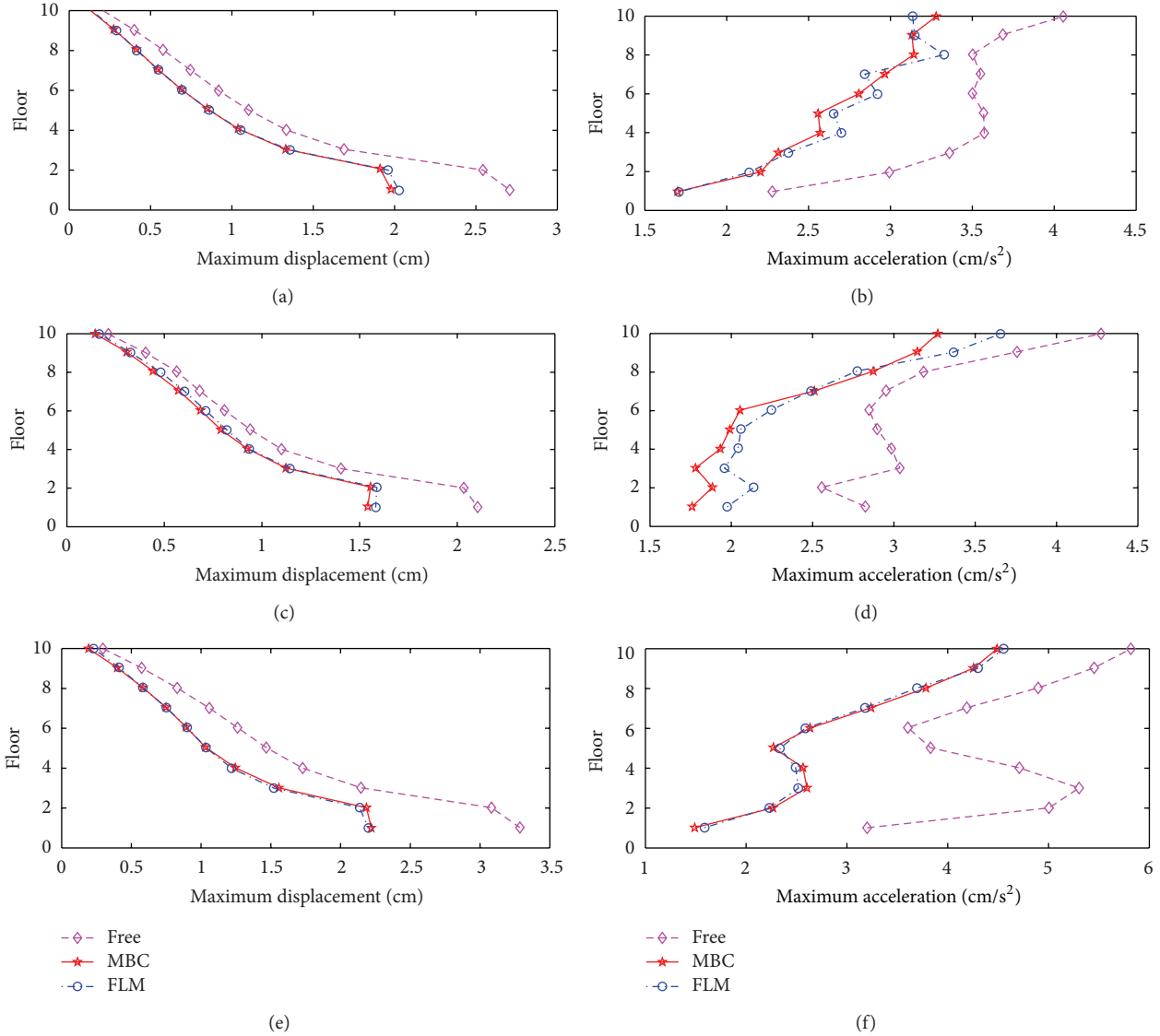


FIGURE 5: Maximum displacement and acceleration responses of each story under various earthquakes: (a), (c), and (e) maximum displacement under nos. 1, 2, and 3 earthquakes; (b), (d), and (f) maximum acceleration under nos. 1, 2, and 3 earthquakes.

TABLE 4: Comparison of computational time of the FLM and MBC algorithms (unit: second).

Methods	Serial number of earthquakes		
	1	2	3
FLM	6.8	7.0	6.7
MBC	12.8	12.4	12.8

The comparison of the time consumed on the completion of dynamic control analysis between using the MBC and FLM is shown in Table 4. It can be seen that the FLM compared to MBC can dramatically reduce the computational time.

The maximum displacement and acceleration of each floor for the three cases, FREE, MBC, and FLM, are shown

in Figure 5. It can be seen that the FLM has ability of reducing the displacement and acceleration responses effectively similar to the MBC through comparing responses of these three cases. Table 5 showed the maximum displacement and acceleration responses of the first, fifth, and tenth floor, and the maximum displacement and acceleration reduction ratio attaches to 33.12% and 50.42%. The controlling force in MBC is simulated to the price in market and also influenced by input earthquakes acceleration. Thus, both the price and input earthquake acceleration should have close changing trend. Figures 6, 7, and 8 illustrated that the price has the same changing trend as the theoretical control force of the first floor under the three earthquake records. The price and theoretical control force in the MBC agree well with that in the FLM. In addition, it was revealed that the FLM has excellent control effectiveness under the three earthquake records although it

TABLE 5: Peak response and control effect of the structure.

Earthquakes	Floor	Interstory displacement			Inter-story acceleration		
		Peak (cm)		Reduction ratio (%)	Peak (m/s ²)		Reduction ratio (%)
		FREE	FLM		FREE	FLM	
1	1	2.71	2.02	25.37	2.28	1.71	24.90
	5	1.10	0.86	22.03	3.58	2.66	25.46
	10	0.21	0.14	33.00	4.06	3.14	22.62
2	1	2.11	1.58	24.79	2.83	1.98	30.08
	5	0.94	0.82	12.82	2.90	2.06	29.01
	10	0.22	0.17	22.45	4.28	3.66	14.47
3	1	3.29	2.19	33.12	3.21	1.59	50.42
	5	1.47	1.03	29.64	3.83	2.33	39.10
	10	0.30	0.23	24.52	5.82	4.56	21.74

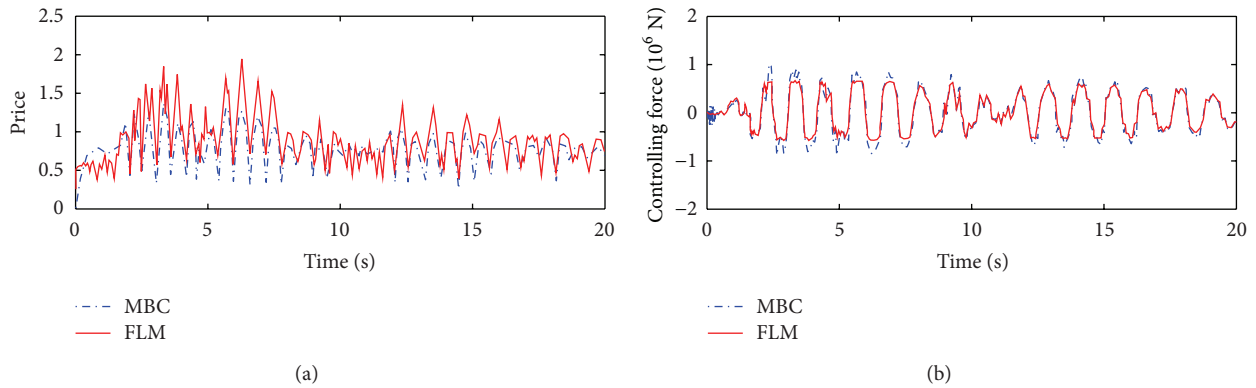


FIGURE 6: Responses of the structure under no. 1 earthquake record: (a) price time history; (b) control force time history.

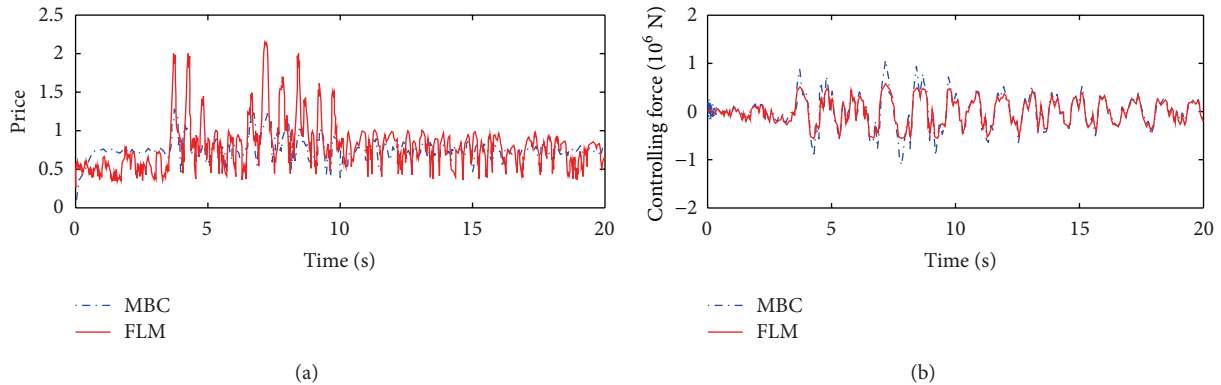


FIGURE 7: Responses of the structure under no. 2 earthquake record: (a) price time history; (b) control force time history.

was only sourced from the case under El Centro earthquake record.

5. Summary and Conclusions

Significant progress has gone towards developing a new control category, which has the highest performance on the robustness, uncertainty, and effectiveness in civil engineering. Although the MBC has capability of performing an effective control for structures, the complex solution of

equilibrium price and poor robustness of the MBC limits its application in complex structures. As the artificial intelligence theory matures, the fuzzy logical method is introduced or incorporated in the structural control technology in recent years. Many problems, which are relatively difficult to answer using the traditional control method, were solved with various degrees through the smart control algorithms and technology. In this paper, the fuzzy logical method is incorporated in the MBC to simplify the MBC procedure and improve its performance through establishing a fuzzy

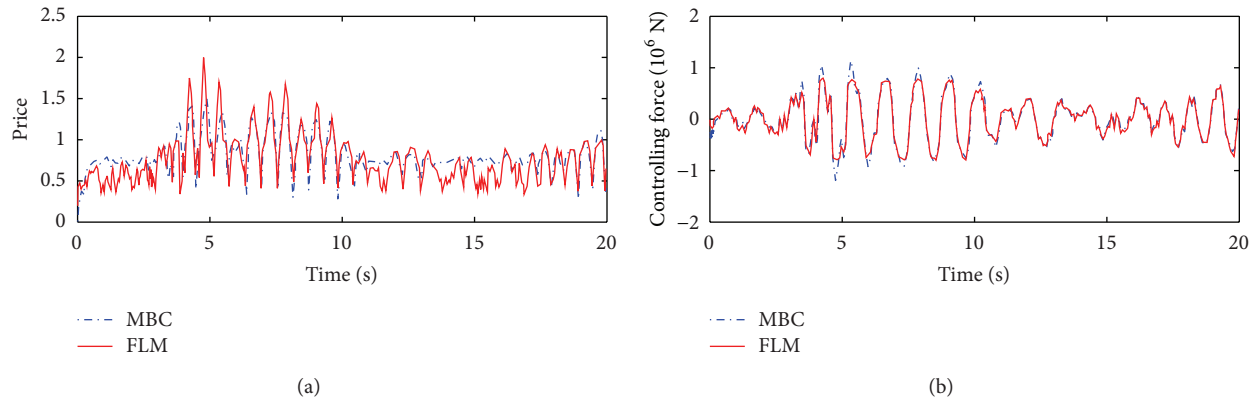


FIGURE 8: Responses of the structure under no. 3 earthquake record: (a) price time history; (b) control force time history.

rule based on a single-degree-of-freedom system under the earthquake. The results have shown that the fuzzy rule has ability of reducing the displacement and acceleration responses effectively similar to the MBC through comparing researches, and consuming computation time for the FLM is obviously saved. The present research implements a fuzzy theory model for use in the market-based control, which is a robust, efficient, and stable algorithm for conducting the structural vibration control.

Acknowledgments

Funding for authors was provided by the Science Fund for Creative Research Groups of the National Natural Science Foundation of China (Grant no. 51121005), the National Natural Science Foundation of China (Grant no. 51222806), and 973 Project (Grand no. 2011CB013605). The opinions, findings, and conclusions expressed in this paper are those of the authors and do not necessarily reflect the views of those acknowledged here.

References

- [1] T. T. Soong, *Active Structure Control Theory and Practice*, Longman Scientific & Technical, New York, NY, USA, 1990.
- [2] L. Huo, G. Song, H. N. Li, and K. Grigoriadis, "H ∞ robust control design of active structural vibration suppression using an active mass damper," *Smart Materials and Structures*, vol. 17, no. 1, pp. 15–21, 2008.
- [3] J. P. Ou, *Structural Vibration Control-Active, Semi-Active and Smart Control*, Science Press, Beijing, China, 2003.
- [4] S. Clearwater, *Market-Based Control: A Paradigm for Distributed Resource Allocation*, World Scientific, Singapore, 1996.
- [5] T. Alpcan, T. Başar, R. Srikant, and E. Altman, "CDMA uplink power control as a noncooperative game," in *Proceedings of the 40th IEEE Conference on Decision and Control (CDC '01)*, pp. 197–202, Orlando, Fla, USA, December 2001.
- [6] J. E. Hilland, R. R. Wessen, D. Porter, and R. S. Austin, "A market-based conflict resolution approach for satellite mission planning," *IEEE Transactions on Engineering Management*, vol. 48, no. 3, pp. 272–282, 2001.
- [7] M. B. Dias and A. Stents, "A comparative study between centralized, market-based, and behavioral multi-robot coordination," in *Proceedings of the IEEE/RSL International Conference on Intelligent Robots and Systems (IROS '03)*, pp. 2297–2303, Las Vegas, Nev, USA, October 2003.
- [8] W. B. Jackson, C. Mochon, K. Van Schuylenbergh et al., "Distributed allocation using analog market wire computation and communication," in *Proceedings of the 7th Mechatronics Forum International Conference*, Atlanta, Ga, USA, September 2000.
- [9] K. Prouskas, A. Patel, J. Pitt et al., "A multi-agent for intelligent network load control using a market-based approach," in *Proceedings of the 4th International Conference on Multi Agent Systems (ICMAS '00)*, pp. 231–238, IEEE Computer Society, Boston, Mass, USA, 2000.
- [10] J. P. Lynch and K. H. Law, "Market-based control of linear structural systems," *Earthquake Engineering and Structural Dynamics*, vol. 31, no. 10, pp. 1855–1877, 2002.
- [11] L. Huo and H. Li, "Control law for market-based semi-active timed liquid column dampers," *Chinese Journal of Applied Mechanics*, vol. 1, pp. 71–75, 2005.
- [12] Y. Li, *Structural vibration control using MBC strategy [Masteral dissertation]*, Dalian University of Technology, Dalian, China, 2007.
- [13] G. Li, Q. Liu, and H. N. Li, "Inelastic structural control based on MBC and FAM," *Mathematical Problems in Engineering*, vol. 2011, Article ID 460731, 18 pages, 2011.
- [14] M. Aldawod, B. Samali, F. Naghdy, and K. C. S. Kwok, "Active control of along wind response of tall building using a fuzzy controller," *Engineering Structures*, vol. 23, no. 11, pp. 1512–1522, 2001.
- [15] A. S. Ahlawat and A. Ramaswamy, "Multiobjective optimal structural vibration control using fuzzy logic control system," *Journal of Structural Engineering*, vol. 127, no. 11, pp. 1330–1337, 2001.
- [16] K. C. Schurter and P. N. Roschke, "Neuro-fuzzy control of structures using acceleration feedback," *Smart Materials and Structures*, vol. 10, no. 4, pp. 770–779, 2001.
- [17] K.-S. Park, H.-M. Koh, and C.-W. Seo, "Independent modal space fuzzy control of earthquake-excited structures," *Engineering Structures*, vol. 26, no. 2, pp. 279–289, 2004.
- [18] M. K. Bhardwaj and T. K. Datta, "Semiactive fuzzy control of the seismic response of building frames," *Journal of Structural Engineering*, vol. 132, no. 5, pp. 791–799, 2006.

- [19] H.-S. Kim and P. N. Roschke, "GA-fuzzy control of smart base isolated benchmark building using supervisory control technique," *Advances in Engineering Software*, vol. 38, no. 7, pp. 453–465, 2007.
- [20] R. Guclu and H. Yazici, "Fuzzy logic control of a non-linear structural system against earthquake induced vibration," *Journal of Vibration and Control*, vol. 13, no. 11, pp. 1535–1551, 2007.
- [21] S. M. Zahrai and A. Shafieezadeh, "Semi-active control of the wind-excited benchmark tall building using a fuzzy controller," *Iranian Journal of Science and Technology B*, vol. 33, no. 1, pp. 1–14, 2009.
- [22] D. Zhao and H. Li, "Shaking table tests and analyses of semi-active fuzzy control for structural seismic reduction with a piezoelectric variable-friction damper," *Smart Materials and Structures*, vol. 19, no. 10, pp. 1–9, 2010.
- [23] K. Yeh, "Seismic response control of sliding isolated buildings using adaptive fuzzy sliding mode control," *International Journal of Physical Sciences*, vol. 6, no. 20, pp. 4732–4738, 2011.

Research Article

Numerical Study on Nonlinear Semiactive Control of Steel-Concrete Hybrid Structures Using MR Dampers

Long-He Xu,¹ Zhong-Xian Li,² and Yang Lv²

¹ School of Civil Engineering, Beijing Jiaotong University, Beijing 100044, China

² School of Civil Engineering, Tianjin University, Tianjin 300072, China

Correspondence should be addressed to Long-He Xu; lhxu@bjtu.edu.cn

Received 28 May 2013; Accepted 19 June 2013

Academic Editor: Gang Li

Copyright © 2013 Long-He Xu et al. This is an open access article distributed under the Creative Commons Attribution License, which permits unrestricted use, distribution, and reproduction in any medium, provided the original work is properly cited.

Controlling the damage process, avoiding the global collapse, and increasing the seismic safety of the super high-rise building structures are of great significance to the casualties' reduction and seismic losses mitigation. In this paper, a semiactive control platform based on magnetorheological (MR) dampers comprising the Bouc-Wen model, the semi-active control law, and the shear wall damage criteria and steel damage material model is developed in LS-DYNA program, based on the data transferring between the main program and the control platform; it can realize the purpose of integrated modeling, analysis, and design of the nonlinear semi-active control system. The nonlinear seismic control effectiveness is verified by the numerical example of a 15-story steel-concrete hybrid structure; the results indicate that the control platform and the numerical method are stable and fast, the relative displacement, shear force, and damage of the steel-concrete structure are largely reduced using the optimal designed MR dampers, and the deformations and shear forces of the concrete tube and frame are better consorted by the control devices.

1. Introduction

Structural control has been proved to be an effective technique to improve the resistance performance of structures excited by both earthquakes and wind through energy dissipation by supplemental devices. In the last several decades, semiactive control methods, for the reliability, adaptability, low power input, controllability, and rapid response capability, have been widely studied, and many control algorithms using MR dampers [1] have been proposed for civil engineering applications and have built a self-contained theory system in the field of the linear system. To consider the nonlinear behaviors of the practical structures, the focus of study has been transferred to the robustness and feasibility of nonlinear control system, and the third generation benchmark model [2] considering the nonlinear property of material was proposed and had made some achievements [3–5]. Lee et al. [6] conducted a numerical study to evaluate the performance of an MR damper for a SDOF structure considering the soil-structure interaction effects, and Li and Wang [7] conducted an experimental investigation to demonstrate the feasibility

and capability of MR dampers for seismic control of nonlinear civil structure considering soil-structure interaction effects. Carrion et al. [8] presented an approach for real-time hybrid simulation in which compensation for actuator dynamics is implemented using a model-based feedback compensator. Christenson et al. [9] studied the real-time hybrid simulation experimental setup for multiple large-scale MR dampers and demonstrated the feasibility in a real-time hybrid test. Park et al. [10] presented a quantitative evaluation of the seismic performance of a building structure installed with an MR damper using real-time hybrid testing method. However, most of the studies focus on steel frame structures, and most control algorithms are suitable to the linear structural control under small or medium earthquake motions. In this paper, a semiactive control platform based on MR dampers is developed in LS-DYNA program, and it can realize the purpose of integrated modeling, analysis, and design of the nonlinear semiactive control system. The steel damage model, damage criteria for the concrete shear wall, and the optimal designed control force of MR dampers are also developed. A 15-story steel-concrete hybrid structure

is analyzed and compared to verify the nonlinear damage control performance on the control platform.

2. Nonlinear Semiactive Control Formulation

2.1. Semiactive Control Platform. The semiactive control system consists of the transducers, controller, and actuators. The transducers gather the structural responses and feedback to the controller, the feedbacks and states of MR dampers are analyzed and judged by the controller and command the power source to supply voltage to MR dampers, and control forces produced by MR dampers are applied to the structure to reduce its responses. With the development of the computing capacity of computers, the finite element method has become one of the most important research approaches in the engineering fields. To conduct a nonlinear seismic damage analysis of semiactive control system in general finite element software, the transducers, the semiactive controller, and the actuators should be developed into the subroutines, and unobstructed contact with the main program besides has the advantages of fast computation, numerical stable and high precise.

The frame of the developed semiactive control platform is shown in Figure 1. The finite element model of the structure is built through the preprocessor of the main program, in which the material models, element types, contact definition, boundary conditions, and load conditions are all reasonably defined. The subroutines are called step by step during the simulation, where the Bouc-Wen model [11] is used to portray the behavior of MR dampers. Both the main program and the subroutines of LS-DYNA software are based on explicit integration method in which the mass and stiffness matrices are uncoupled; therefore, the active control strategy based semiactive control method is unsuitable for this control platform. What is more, the practical structures experience degenerated performance during strong earthquakes, and the controller designed by the initial stiffness matrix may lead the control process to be unstable and divergent, so the simple bang-bang control law is employed in this platform as follows:

$$F(t) = \begin{cases} F_{I,\max} & x\dot{x} > 0 \\ F_{I,\min} & x\dot{x} \leq 0, \end{cases} \quad (1)$$

where $F(t)$ is the control force produced by MR damper at time t , $F_{I,\max}$ and $F_{I,\min}$ are the maximum and minimum control forces that MR dampers can produce at this moment.

2.2. Nonlinear Damage Criteria

2.2.1. Steel Damage Model. To accurately describe the accumulation and development of structural damage under strong earthquakes, a fiber beam element model approach based on a continuity damage mechanics material model proposed by Bonora [12] was developed in this paper. Each structural member is discretized into a number of sections, and each section is further divided into a number of fibers, as shown in Figure 2. The sections are located either at the center of the element or at its Gaussian integration points, so that the behavior of each fiber is tracked using a simple uniaxial

material model allowing an easy and efficient implementation of the inelastic performance, such as the strength and stiffness degradation behavior. In the continuity damage mechanics based steel material model, the plastic potential f_p is defined as follows:

$$f_p = \sigma_{\text{eq}} - k(\kappa) - \frac{3}{4\alpha_{\infty}} \alpha'_{ij} \alpha'_{ij} - \sigma_y, \quad (2)$$

where σ_y is the initial uniaxial yield stress, α_{∞} is kinematic hardening saturation value, and σ_{eq} is the equivalent stress and is given by

$$\sigma_{\text{eq}} = \left[\frac{3}{2} \left(\frac{s_{ij}}{1-d} - \alpha'_{ij} \right) \left(\frac{s_{ij}}{1-d} - \alpha'_{ij} \right) \right]^{1/2}, \quad (3)$$

where s_{ij} and α'_{ij} are the deviatoric parts of the stress and kinematic hardening tensor, respectively. k is the isotropic hardening stress and is defined through Osgood equation:

$$k(\kappa) = \frac{E_h}{\beta} [1 - \exp(-\beta\kappa)], \quad (4)$$

where E_h is the isotropic hardening modulus, β is isotropic hardening parameter, in which set $\beta = 0$ for linear isotropic hardening, and κ is the isotropic hardening coefficient and is defined as the equivalent accumulated plastic strain:

$$\kappa = \varepsilon_p = \int d\varepsilon_p. \quad (5)$$

The plastic strain components and the internal variables associated with k and α'_{ij} can be derived from f_p by the normality rule:

$$d\varepsilon_{ij}^p = d\lambda \frac{\partial f_p}{\partial \sigma_{ij}} = \frac{3}{2} \frac{d\lambda}{1-d} \frac{(s_{ij}/(1-d)) - \alpha'_{ij}}{\sigma_{\text{eq}}},$$

$$d\alpha'_{ij} = C(1-d)d\varepsilon_{ij}^p - \frac{3C}{2\alpha_{\infty}} \alpha'_{ij} d\lambda, \quad (6)$$

$$d\kappa = -d\lambda \frac{\partial f_p}{\partial k} = d\lambda = (1-d)d\varepsilon_p,$$

where C is the kinematic hardening modulus, λ is the plastic multiplier, and

$$d\varepsilon_p = \left(\frac{2}{3} d\varepsilon_{ij}^p d\varepsilon_{ij}^p \right)^{1/2}. \quad (7)$$

The damage dissipation potential is expressed as

$$f_d = \left[\frac{1}{2} \left(\frac{Y}{S_0} \right)^2 \frac{S_0}{1-d} \right] \frac{(d_{\text{cr}} - d)^{1-1/\nu}}{\kappa^{(2+n)/n}}. \quad (8)$$

The kinetic law of damage evolution is given by

$$\dot{d} = -d\lambda \frac{\partial f_d}{\partial Y} = \frac{(d_{\text{cr}} - d_0)^{1/\nu}}{\ln(\varepsilon_u - \varepsilon_{\text{th}})} f \left(\frac{\sigma_m}{\sigma_{\text{eq}}} \right) (d_{\text{cr}} - d)^{1-1/\nu} \frac{d\kappa}{\kappa}, \quad (9)$$

where Y is the variable associated with damage, ν and S_0 are the material parameters, ε_u and ε_{th} are the critical and threshold equivalent accumulated plastic strains, and d_{cr} and d_0 are critical and initial damages of the material corresponding to ε_u and ε_{th} , respectively.

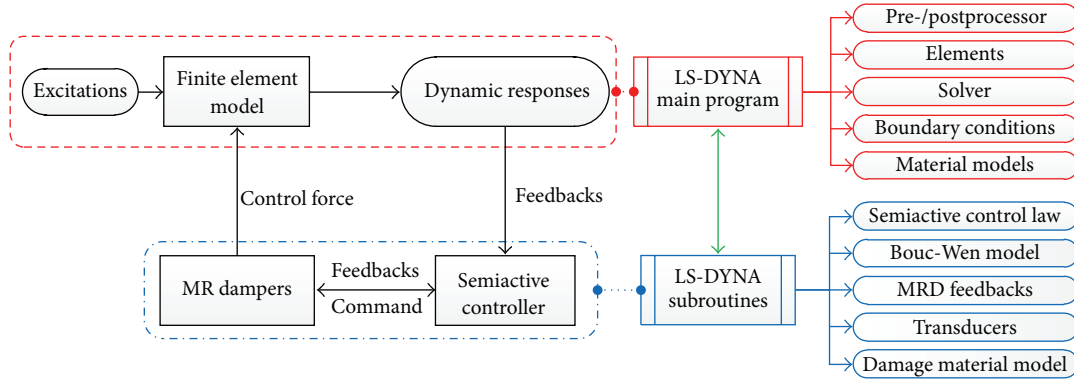


FIGURE 1: The frame of semiactive control platform in LS-DYNA program.

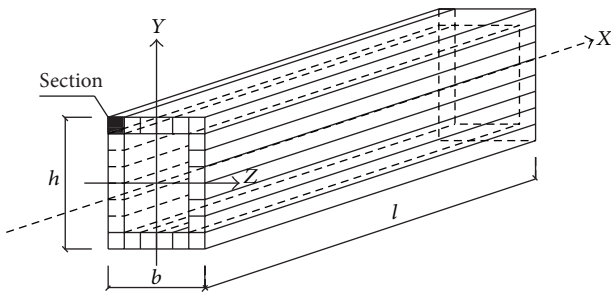


FIGURE 2: The discretization of structural members.

2.2.2. *Shear Wall Damage Criteria.* The pushover tests indicate that the well seismic designed shear wall will experience several stress states, that is, the elastic cracking of the concrete, yielding and reinforcing of the steel bars; the plastic flow of the steel bar, and crushing of concrete or rupture of the steel bars, the corresponding damage process of the shear wall can be divided into the elastic stage from the cracking of the concrete to the yielding of the steel bars, the stable stage, and the decrease stage. Here, the exponential and logarithmic composite function of Bonora model is used to simulate the damage process of the shear wall; the damage criteria is expressed as,

$$d_c = d_{c,0} + (d_{c,cr} - d_{c,0}) \left\{ 1 - \left[1 - \frac{\ln(\delta_m/\delta_{cra})}{\ln(\delta_u/\delta_{cra})} \right]^{\alpha_c} \right\}, \quad (10)$$

where the subscript c denotes the concrete structure. δ_m , δ_u , and δ_{cra} are the maximum, ultimate, and cracking deformation of the shear wall member, respectively, and the other parameters are the same as in the Bonora model. For different α_c value, the model can simulate three typical damage progresses, as shown in Figure 3. Type 1 can simulate the ductile components such as the steel plate shear wall, in which the strength has a little decrease after the yielding of the member; type 3 can simulate the brittle components, in which the concrete crushes or the steel bar ruptures before the yielding of the member; and type 2 is the combination of the former two types, which has an obvious yield platform and is suitable to simulate the normal reinforced concrete shear wall member.

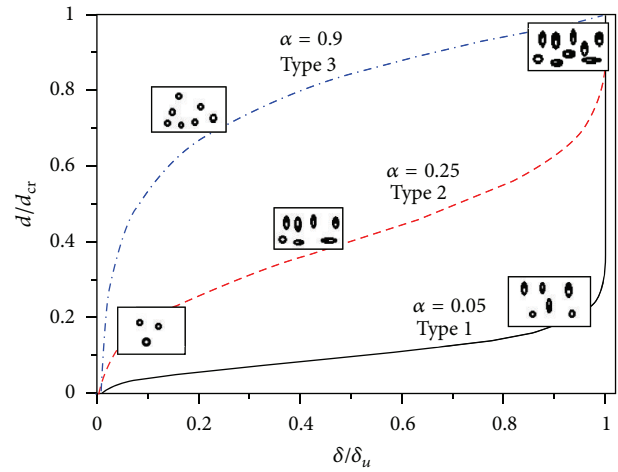


FIGURE 3: Three typical damage processes.

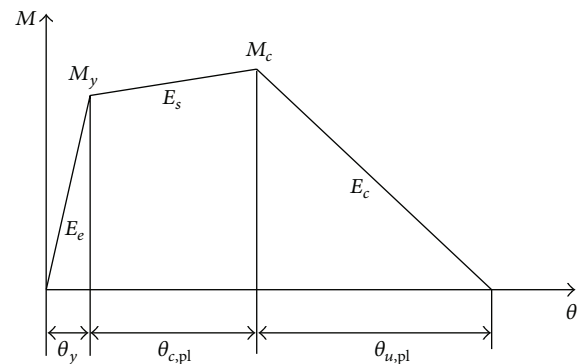


FIGURE 4: Lumped plastic hinge model.

Panagiotakos and Fardis [13] proposed a skeleton curve model of the reinforced concrete member by fitting a large number of tests data. As shown in Figure 4, the model uses 3 lines and 5 parameters, that is, θ_y , M_y , M_c , $\theta_{c,pl}$, and $\theta_{u,pl}$, to simulate the yielding, reinforcing, and strength degeneration of the member, and the model is also suitable for the

reinforced concrete shear wall members. The yield rotation and ultimate rotation are given by

$$\begin{aligned} \theta_y &= \phi_y \frac{L_s}{3} + 0.0025 + a_{sl} \frac{0.25\varepsilon_y d_b f_y}{(d-d') \sqrt{f'_c}} \\ \theta_u (\%) &= \alpha_{st} \alpha_{cyc} \left(1 + \frac{a_{sl}}{2.3}\right) \left(1 - \frac{a_{wall}}{3}\right) (0.2^\nu) \\ &\times \left[\frac{\max(0.01, \rho' f'_y / f'_c)}{\max(0.01, \rho f_y / f'_c)} f'_c \right]^{0.275} \\ &\times \left(\frac{L_s}{h} \right)^{0.45} 1.1^{(\alpha_{\rho_{xx}}(f_{yh} / f'_c))} (1.3^{\rho_d}), \end{aligned} \quad (11)$$

where the parameters are the same as in [13]. The cracking rotation of the model is given by

$$\theta_{cra} = \phi_{cra} \frac{L_s}{3} + 0.0025 + a_{sl} \frac{0.25\varepsilon_y d_b f_y}{(d-d') \sqrt{f'_c}}, \quad (12)$$

where ϕ_{cra} is the curvature corresponding to the cracking of the member and calculated by the cracking strain of concrete. After getting the values of cracking rotation, yielding rotation and ultimate rotation, and assuming that the damage is 0 when the concrete cracks and the damage is 0.2 corresponding to the yielding of the steel bar [14], parameter α_c can be calculated by inversion solving (10) as

$$\alpha_c = \log_{\zeta}^{0.8}, \quad (13)$$

where ζ is expressed as

$$\zeta = 1 - \frac{\ln(\delta_y / \delta_{cra})}{\ln(\delta_u / \delta_{cra})}. \quad (14)$$

3. Numerical Example

3.1. Simulation of Steel-Concrete Structure. The reinforced concrete tube, steel frame, slab, and connecting beam are the basic components of steel-concrete hybrid structure. In the finite element model, the steel frame is simulated by the fiber element model and the damage model developed in (9), the slab is simulated by the layered shell element model, the connecting beam is simulated by the lumped hinge plastic model [13], and the reinforced concrete tube is simulated by the layered shell element model and the damage model developed in (10). The concrete tube of the high-rise building structures usually experiences a global bending deformation due to earthquakes, which makes the upper stories of the concrete tube have a rigid body motion with the rotation of the lower stories, so the true relative deformation of the concrete tube should subtract the nonreal deformation. The relative displacement of the i th story is calculated as follows:

$$\Delta \delta_i = \Delta_i - \Delta_{i-1} - \theta H, \quad (15)$$

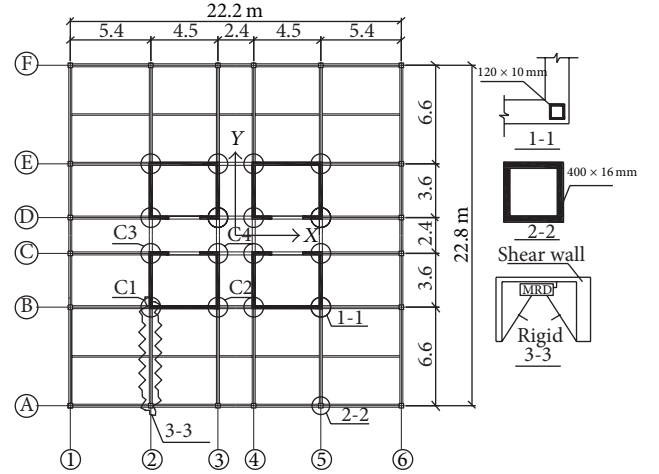


FIGURE 5: Plan view of the structure.

where Δ_{i-1} and Δ_i are the displacements of the i th and $(i-1)$ th story, respectively, θ is the rigid rotation of the $(i-1)$ th story, and H is the height of the i th story.

The numerical example is a 15-story steel-concrete structure [15], as shown in Figure 5, which is 22.2 m by 22.8 m in plan with five bays each in the N-S (X) and E-W (Y) directions. The height of the structure is 58.5 m in elevation with each story height being of 3.9 m. The shear wall depth of the 1st to 3rd story is 300 mm, the 4th to 6th is 250 mm, the 7th to 9th is 220 mm, and that of other stories is 200 mm. The sections of each type of structure members are the same, the columns are $\square 400 \times 400 \times 30$ hollow square steel tube, the beams are H400 \times 250 \times 10 \times 16 steel, the secondary beams are H350 \times 200 \times 10 \times 12 steel, and the connecting beams are 700 \times 250 concrete. To increase the deformation capacity of the concrete tube, a box steel column is embedded at the intersection of the shear walls, the materials of the structure are C40 concrete, HRB335 steel bars, and Q345 steel for the steel frame, and the reinforcement ratio of the shear wall is 0.02. Table 1 shows the parameters of the steel damage model.

MR dampers can significantly increase the energy dissipation capacity of the main structure and usually have little influence on the structural characters. For the determined structure, the internal energy dissipation capacity is controlled by the output force capacity of MR dampers, and the control force of MR damper at each story is optimized as follows:

$$F_j = \frac{\xi_j D_j E_j}{\xi_r D_r E_r} F_r, \quad (16)$$

where D_r , F_r , E_r , and ξ_r are the damage index, control force, dissipated energy, and normalized stiffness of the reference story, respectively. D_j , F_j , E_j , and ξ_j are the damage index, control force, dissipated energy, and normalized stiffness of the j th story, respectively. F_r is determined by the expected control effectiveness and the design standard of MR damper, ξ_j is the stiffness ratio of the j th story to the sum of all the stories, and the damage index D_j is the maximum damage value both in the X and Y direction of the concrete tube at the j th story.

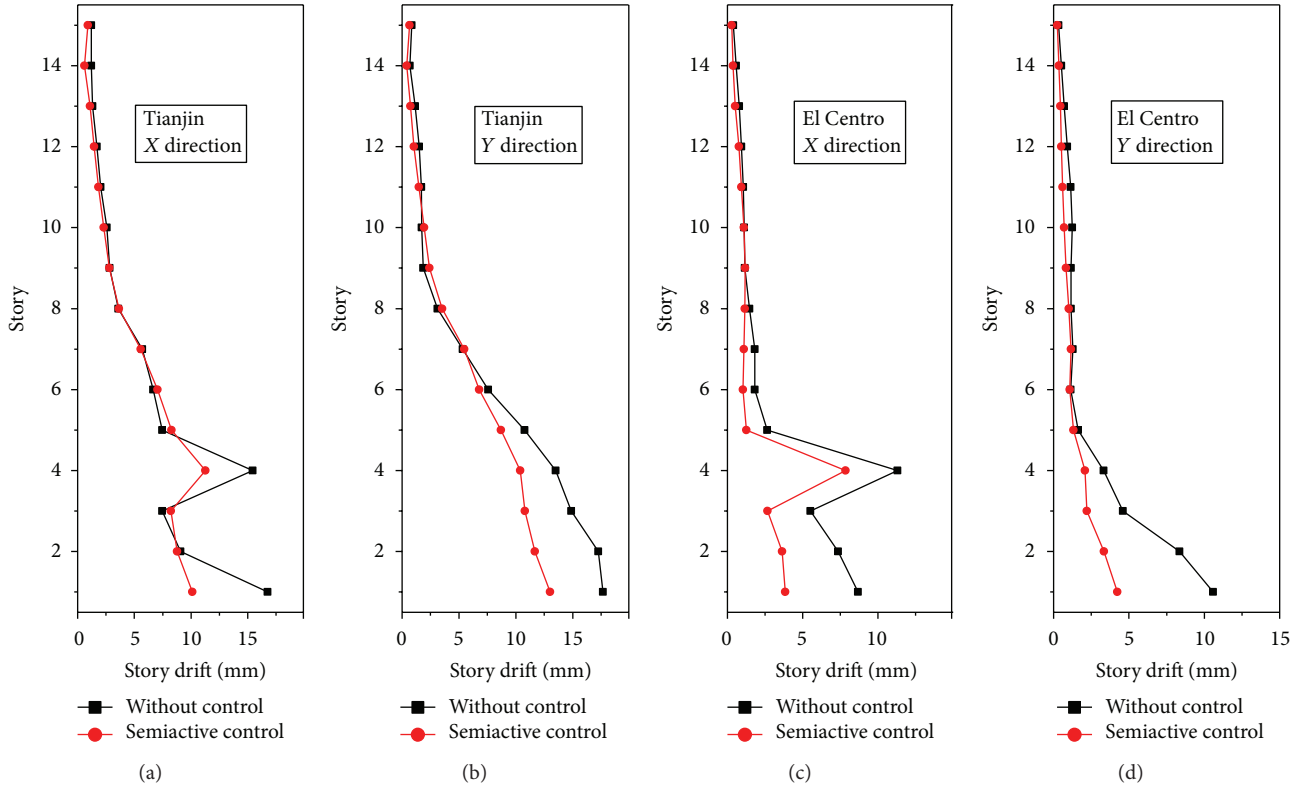


FIGURE 6: Envelope curve of story drift due to Tianjin and El Centro earthquakes in the X and Y directions.

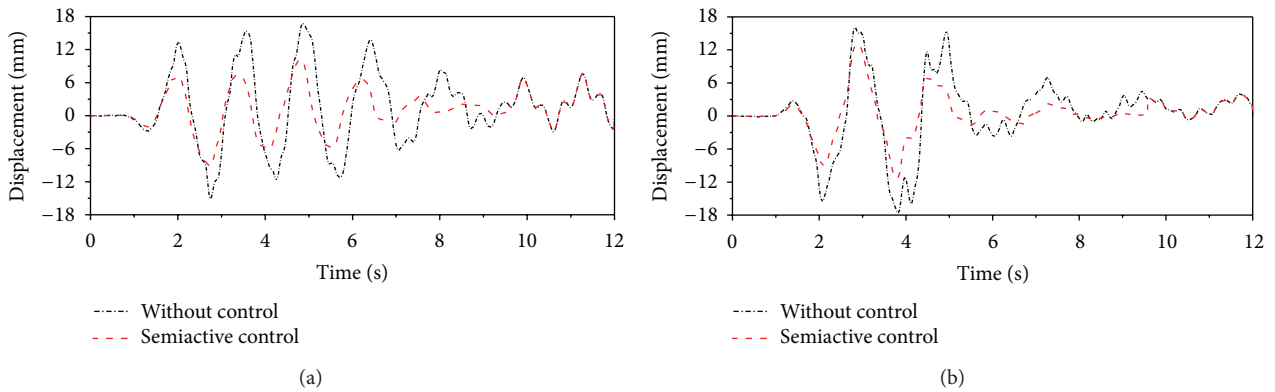


FIGURE 7: Displacement time history of the first floor due to Tianjin earthquake: (a) X direction, (b) Y direction.

TABLE 1: Material parameters.

Parameters	Damage parameters					Plastic parameters			
	ϵ_{th}	ϵ_{cr}	D_{cr}	D_0	α	E_h [MPa]	α_{∞} [MPa]	C [MPa]	β
Value	0.001	0.24	0.065	0	0.2173	200	300	800	0.5

TABLE 2: Control force of the MR dampers at each story.

Story	1	2	3	4	5	6	7	8	9–15
Damage	0.420	0.404	0.358	0.395	0.272	0.193	0.152	0.110	0.061
Energy/kJ	69814	56353	43668	37305	34976	32268	29271	26593	21296
Control force/kN	1000	793	545	430	332	217	129	49	0

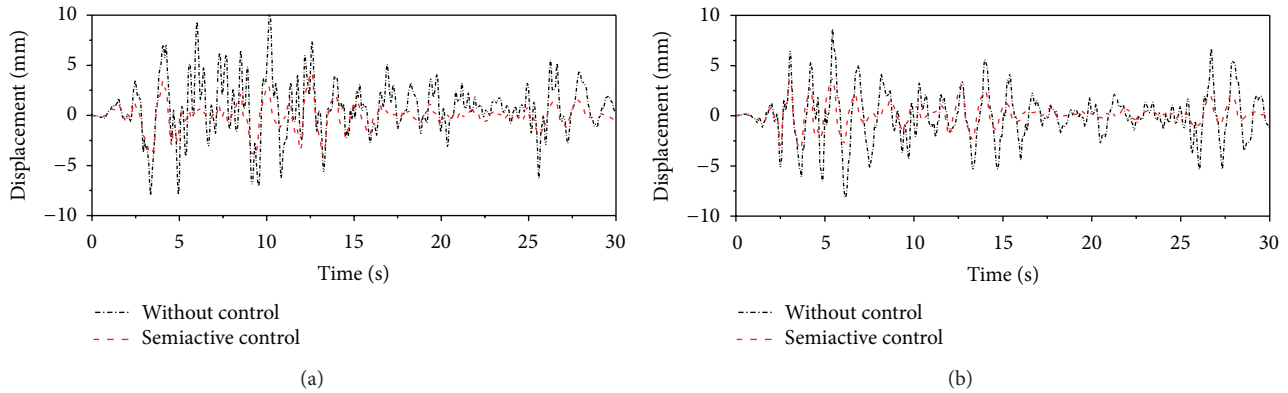


FIGURE 8: Displacement time history of the first floor due to El Centro earthquake: (a) X direction, (b) Y direction.

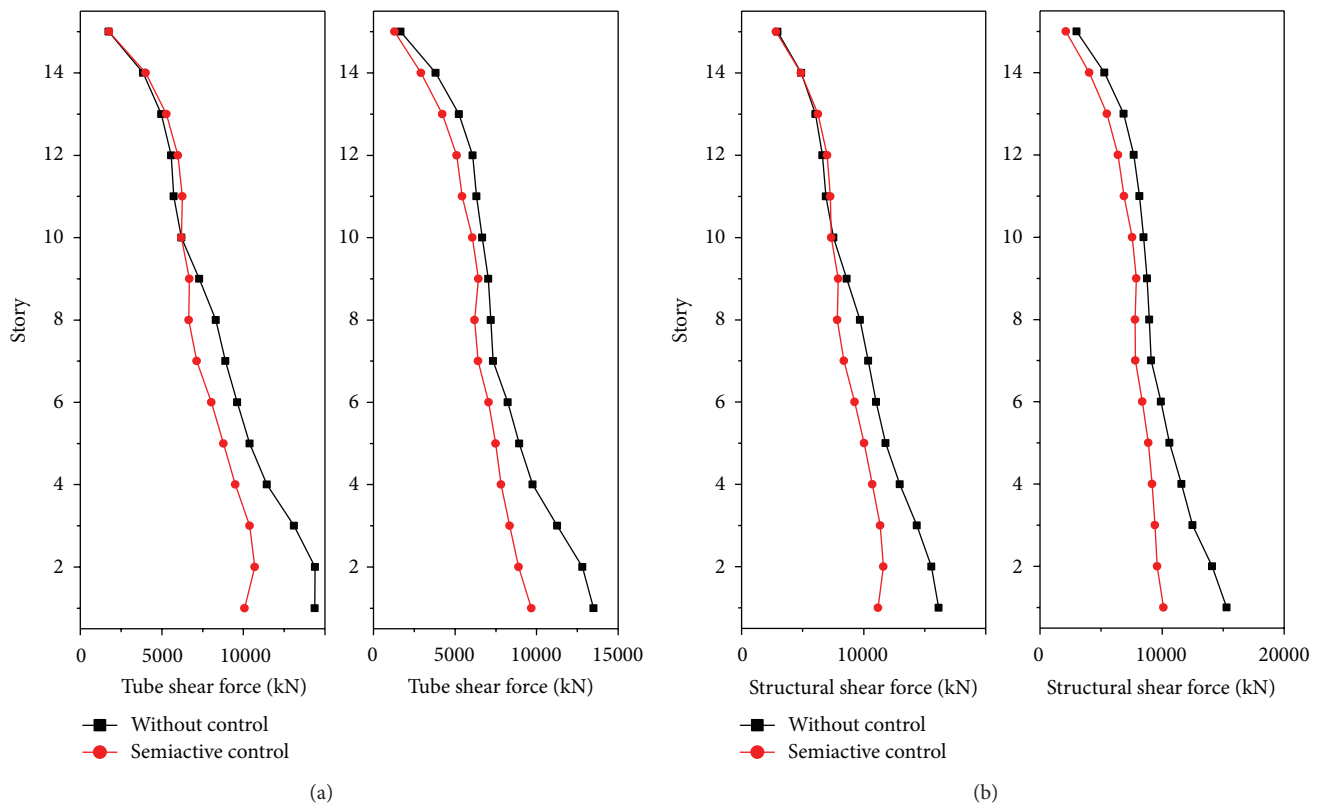


FIGURE 9: Shear force envelop curve of (a) concrete tube and (b) global structure in the X and Y directions.

Two directions of Tianjin, El Centro and Loma Prieta earthquake records with PGA of 0.3g are used as the excitations. 16 MR dampers are located between the steel frame and concrete tube from axis 2 to axis 5 and axis B to axis E at each story, and a total of 128 MR dampers are used from the 1st to 8th story, as shown in Figure 5. The damage process of the concrete tube, the internal energy of each story, and the optimized control force of MR dampers at each story is listed in Table 2.

3.2. Dynamic Responses Analysis. The dynamic responses of the steel-concrete structure with optimal designed force of MR dampers and without MR dampers are analyzed due

to the PGA of 0.3g Tianjin, El Centro and Loma Prieta earthquakes. The story drift envelop curve due to Tianjin and El Centro earthquakes is shown in Figure 6, and the relative displacement time histories of the first story are shown in Figures 7 and 8. It is indicated that the displacement of the controlled structure is smaller than that of the uncontrolled ones both in X and Y directions, the story drifts of the hybrid structure have been reduced by MR dampers and especially for the lower several stories because more powerful MR dampers are installed at the lower stories compared to the upper ones and the deformations are better controlled, while the members at upper several stories are still elastic and have very small deformation. From the envelop curves

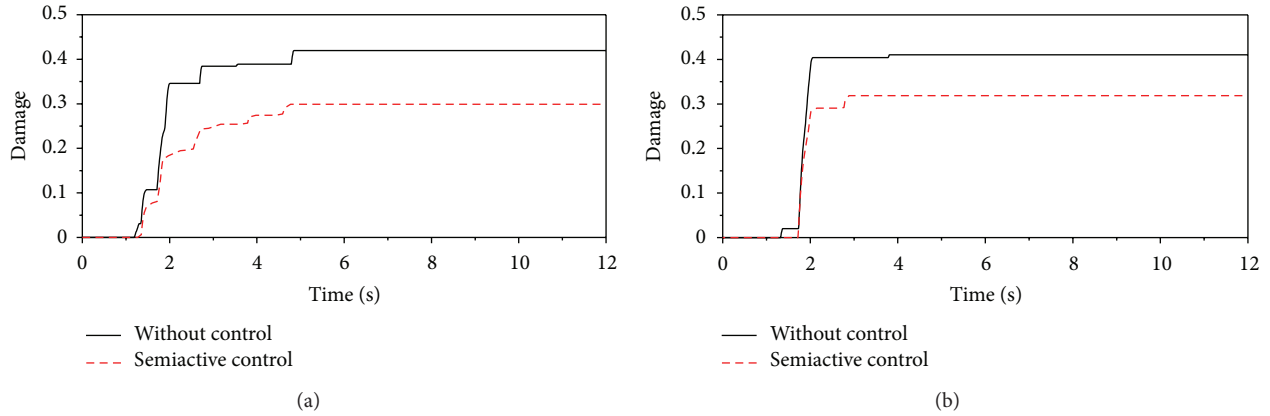


FIGURE 10: Damage process time history of the concrete core tube due to Tianjin earthquake: (a) X direction and (b) Y direction.

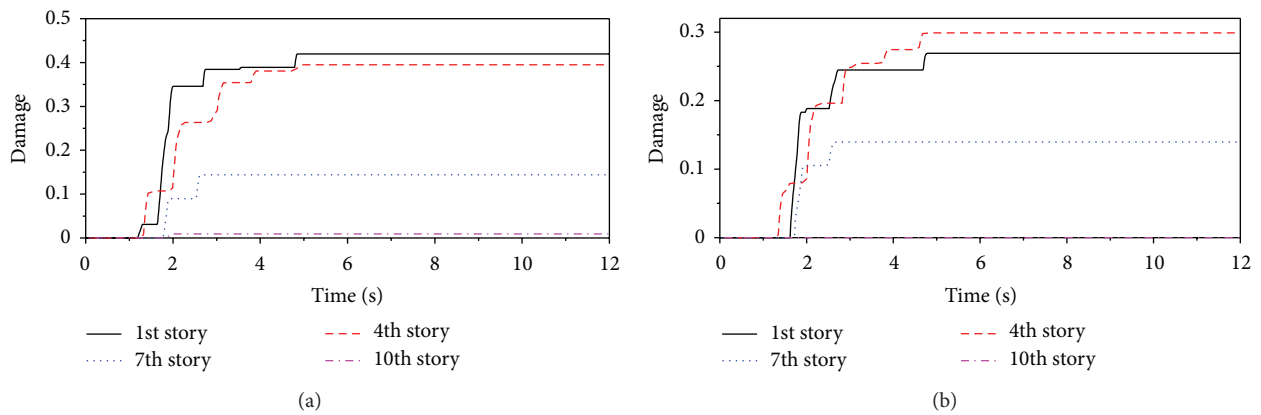


FIGURE 11: Damage process time history of the concrete core tube at some stories due to Tianjin earthquake: (a) without control and (b) semiactive control.

in the X direction shown in Figure 6, the deformation drifts at the 4th story because the depth of the shear wall changes here and the weak links occur. For the controlled structure, the deformation is smaller but also drifts at the 4th story, so the MR dampers can reduce the structural deformation but cannot eliminate the weak links completely.

The shear force envelop curve of the concrete tube and the global structure due to El Centro earthquake are shown in Figure 9. It is shown that the shear force of the controlled structures is smaller than that of the uncontrolled ones, although the MR dampers are located at some lower stories, and the shear force of the upper stories is also well controlled, which demonstrates the excellent control performance of MR dampers for using in steel-concrete structures.

3.3. Damage Analysis. The damage process of the concrete tube and the steel columns of the hybrid structure due to Tianjin earthquake is analyzed based on the damage criteria of shear wall and the steel damage material model because there is no damage in the steel frame, and the damage analysis of the steel frame is not involved. The damage process of the structure with and without MR dampers is shown in Figure 10; it is indicated that the damage of the concrete tube of MR dampers controlled structure is much smaller than that

of the uncontrolled ones because MR dampers are directly installed between the concrete tube and the steel frame; the deformations and shear forces of the tube and frame are better consorted by the control devices. Figure 10 also indicates that the damages of both the controlled and uncontrolled structures develop at the peak acceleration points and have the same process pattern; therefore, MR dampers can reduce the damage value but cannot eliminate the damage, which is consistent with the conclusions of the relative displacement, and it is also determined from the control mechanism of MR damper, that is, which can only apply the control force passively through the relative displacement of the story.

The damage process of the concrete tube at the stories where the shear wall depth changes, that is, the 1st, 4th, 7th, and 10th stories, is shown in Figure 11; it is indicated that the damage of the 10th story of MR dampers controlled structure is 0, and the damage values of the other stories are also reduced. The controlled and uncontrolled structures have a similar damage process pattern, and the damage mainly shifts at the peak acceleration points. In addition, the damage process of the 4th story is fast because of the weak links.

The damage process of the embedded steel columns at the intersection of the concrete tube is shown in Figure 12, and the serial number of the columns is shown in Figure 5. It is

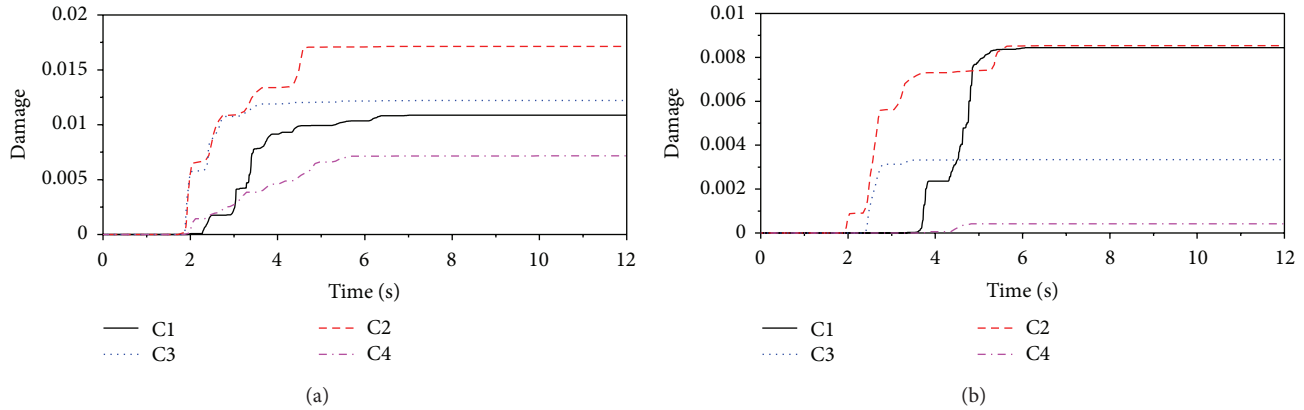


FIGURE 12: Damage process time history of each embedded steel column due to Tianjin earthquake: (a) without control and (b) semiactive control.

indicated that MR dampers can effectively reduce the damage intensity of the insert columns, and, comparing the damage processes of the concrete tube and the steel columns shows that the damage process of the steel columns lags behind the concrete tube and the steel columns also have obvious damage even after the peak acceleration points; the reason is that the concrete tube experiences serious damage at the peak acceleration points, and the degeneration of the concrete strength makes the steel columns sustain increasing shear force. And, for the lower several stories, the large bending moment causes the concrete tube to undertake large axial forces and crack under the tension forces, and then the axial forces are transferred to the steel columns; that is why the steel columns damage keeps increasing at the subsequent lower earthquakes. From the damage of different columns at the same story, it is indicated that the outside columns have larger damage than that of the inner columns, such as columns C1, C2, and C3 because the outside columns sustain bigger axial force to balance the bending moment of the structure. The damage process of structures with and without MR dampers is different; the reason is that the loading state of the embedded columns varies with the strength of the concrete tube, and the performance of the upper concrete tube and MR dampers will influence the loading state of the embedded columns and interfere with the damage process of the steel columns.

4. Conclusions

A semiactive control platform comprising the Bouc-Wen model of MR damper, the simple bang-bang semiactive control law, and the damage material model is developed in LS-DYNA program, based on the data transferring between the main program and the control platform; it can realize the purpose of integrated modeling, analysis, and design of the nonlinear semiactive control system. The steel damage model, damage criteria for the concrete shear wall, and the optimal designed control force of MR dampers are also developed. The nonlinear seismic control effectiveness is verified by the numerical example of a 15-story steel-concrete

hybrid structure; results indicate that the control platform and the numerical method are stable and fast; the relative displacement, shear force, and damage of the steel-concrete structure are largely reduced using optimal designed MR dampers, when MR dampers are directly installed between the concrete tube and the steel frame; the deformations and shear forces of the concrete tube and frame are better consorted by the control devices. MR dampers also can effectively reduce the damage intensity of the embedded steel columns at the intersection of the concrete tube.

Acknowledgments

The authors gratefully acknowledge the partial support of this research by the National Natural Science Foundation of China under Grant no. 51178034 and the 111 project under Grant no. B13002.

References

- [1] B. F. Spencer Jr. and S. Nagarajaiah, "State of the art of structural control," *Journal of Structural Engineering*, vol. 129, no. 7, pp. 845–856, 2003.
- [2] Y. Ohtori, R. Christenson, B. F. Spencer Jr., and S. J. Dyke, "Benchmark control problems for seismically excited nonlinear buildings," *Journal of Engineering Mechanics*, vol. 130, no. 4, pp. 366–385, 2004.
- [3] O. Yoshida and S. J. Dyke, "Seismic control of a nonlinear benchmark building using smart dampers," *Journal of Engineering Mechanics*, vol. 130, no. 4, pp. 386–392, 2004.
- [4] N. Wongprasert and M. D. Symans, "Application of a genetic algorithm for optimal damper distribution within the nonlinear seismic benchmark building," *Journal of Engineering Mechanics*, vol. 130, no. 4, pp. 401–406, 2004.
- [5] S. Sahasrabudhe and S. Nagarajaiah, "Experimental study of sliding base-isolated buildings with magnetorheological dampers in near-fault earthquakes," *Journal of Structural Engineering*, vol. 131, no. 7, pp. 1025–1034, 2005.
- [6] S.-K. Lee, S.-H. Lee, K.-W. Min, B.-W. Moon, K.-J. Youn, and J.-S. Hwang, "Performance evaluation of an MR damper in building structures considering Soil-structure interaction

- effects,” *Structural Design of Tall and Special Buildings*, vol. 18, no. 1, pp. 105–115, 2009.
- [7] H. Li and J. Wang, “Experimental investigation of the seismic control of a nonlinear soil-structure system using MR dampers,” *Smart Materials and Structures*, vol. 20, no. 8, Article ID 085026, 2011.
- [8] J. E. Carrion, B. F. Spencer Jr., and B. M. Phillips, “Real-time hybrid simulation for structural control performance assessment,” *Earthquake Engineering and Engineering Vibration*, vol. 8, no. 4, pp. 481–492, 2009.
- [9] R. Christenson, Y. Z. Lin, A. Emmons, and B. Bass, “Large-scale experimental verification of semiactive control through real-time hybrid simulation,” *Journal of Structural Engineering*, vol. 134, no. 4, pp. 522–534, 2008.
- [10] E. Park, K.-W. Min, S.-K. Lee et al., “Real-time hybrid test on a semi-actively controlled building structure equipped with full-scale MR dampers,” *Journal of Intelligent Material Systems and Structures*, vol. 21, no. 18, pp. 1831–1850, 2010.
- [11] L. M. Jansen and S. J. Dyke, “Semiactive control strategies for MR dampers: comparative study,” *Journal of Engineering Mechanics*, vol. 126, no. 8, pp. 795–803, 2000.
- [12] N. Bonora, “A nonlinear CDM model for ductile failure,” *Engineering Fracture Mechanics*, vol. 58, no. 1-2, pp. 11–28, 1997.
- [13] T. B. Panagiotakos and M. N. Fardis, “Deformations of reinforced concrete members at yielding and ultimate,” *ACI Structural Journal*, vol. 98, no. 2, pp. 135–148, 2001.
- [14] M. S. Williams and R. G. Sexsmith, “Seismic damage indices for concrete structures: a state-of-the-art review,” *Earthquake Spectra*, vol. 11, no. 2, pp. 319–349, 1995.
- [15] Y. Zhou, X. L. Lu, Z. H. Huang, and Y. Bo, “Seismic behavior of composite shear walls with multi-embedded steel sections. Part II: analysis,” *The Structural Design of Tall and Special Buildings*, vol. 19, no. 6, pp. 637–655, 2010.